**Title**
DYNAMICS OF THE REACTION OF THE N+ION WITH HYDROGEN ISOTOPES AND HELIUM



**Author**
Ruska, Walter Ernst William.

**Publication Date**
1976-06-01

LBL-5120

# DYNAMICS OF THE REACTION OF THE $N^+$ ION WITH HYDROGEN ISOTOPES AND HELIUM

Walter Ernst William Ruska
(Ph. D. thesis)



June 28, 1976

Prepared for the U. S. Energy Research and
Development Administration under Contract W-7405-ENG-48



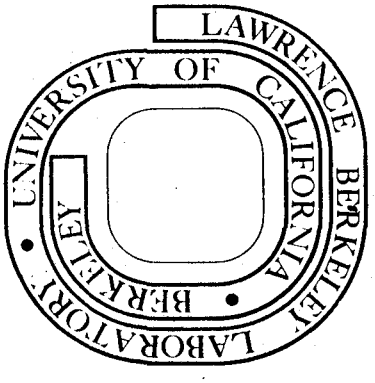


LBL-5120

## DISCLAIMER

# DYNAMICS OF THE REACTION OF THE $N^+$ ION WITH HYDROGEN ISOTOPES AND HELIUM

Walter Ernst William Ruska

## Abstract

Molecular beam techniques were used to study the reactive and non-reactive scattering of the nitrogen positive ion from hydrogen isotopes and helium, at energies above the stability limit for spectator stripping. Reactive scattering was observed from $H_2$ and HD targets. The intensity maxima for $NH^+$ product from both isotopes, above the stripping limit, were in the forward hemisphere at CM angles from 20° to 60°. The position of these maxima were dependent on the isotope used and relatively insensitive to collision energy. At the highest energies studied, a small product peak appeared on the centerline. This peak was correlated in intensity with the amount of excited $N^+(^1D)$ in the beam (<3% under normal conditions) and is attributed to the reaction of the excited ion. At energies slightly above the stripping limit, $ND^+$ product from HD target showed a similar distribution to that of the $NH^+$ product, except for an additional maximum at $\chi = 180°$. At higher energies only, the 180° peak was present. All reactive scattering was of low intensity.

Non-reactive scattering was observed from $H_2$ and $D_2$ targets, and from He at one energy. With both $H_2$ and $D_2$, the scattered intensity was low at all angles away from the beam direction. The product showed moderate endothermicity, and was centered about the system (ion-molecule) centroid instead of the impulsive (ion-atom) centroid at all energies. Scattering from He consisted of an elastic component and a component resulting from the electronic transition $N^+(^3P) \rightarrow N^+(^3D)$. The total cross-section for charge exchange at 70 eV was investigated and estimated as $\gtrsim 25$ $\mathring{A}^2$: charge exchange is therefore the dominant channel at higher energies.

A correlation diagram for the system is presented and compared with the available a priori calculations. Two surfaces are expected to lead to reaction. One is a $^3A_2$ - $^3\Pi$ surface, which is essentially flat and produces $NH^+(^2\Pi)$. An avoided crossing on this surface may lead to charge exchange involving collinear approaches and producing $N(^4S)$. The other surface, a $^3B_1$ - $^3\Sigma^-$ surface, has a 1 eV barrier to perpendicular approach and produces $NH^+(^4\Sigma^-)$. Charge exchange is likely for perpendicular approaches, yielding $N(^2D)$. As a result, collinear approaches are expected to be most reactive on the $^3B_1$ - $^2\Sigma^-$ surface; non-collinear, on the $^3A_1$ - $^3\Pi$ surface.

Theoretical models are presented in which an incident hard sphere A, representing the projectile ion, strikes one of a pair of hard spheres B-C representing the B hydrogen

molecule. After an impulsive A-B collision, an impulsive B-C collision may take place. The relative energy of A to B is then examined, and a reactive event is considered to have occurred if the energy is less than the dissociation energy for the A-B molecule. This model is treated both in the collinear case and in three dimensions. A graphical technique for the collinear case is summarized and applied to reaction on the $^3B_1$ - $^3\Sigma^-$ surface: it successfully predicts the observed scattering behind the center of mass. An integral equation for the three-dimensional case is developed. When applied to reaction on the $^3A_1$ - $^3\Pi$ surface, it accurately predicts the observed scattering forward of the center of mass. A synthesis of the two treatments, representing the behavior of the system on both reactive surfaces, and considering the charge-exchange channel, correctly predicts the observed product distribution. Predictions are also presented for the as yet unobserved case of reactive scattering from $D_2$ target.

# ACKNOWLEDGEMENTS

To Professor Bruce H. Mahan, my research director, an educator in the fullest sense of the word, for instruction and inspiration, by precept and example, in the craft and calling of science;

To my friends and my family, for their encouragement and understanding, without which this work would not exist;

To the faculty of the University of California at Berkeley and of Rice University, for fine undergraduate and graduate instruction, and particularly to Professor Joe L. Franklin of Rice, who introduced me to research;

To all of my fellow members in this research group, past and present, for guidance, cooperation, assistance, timely correction, and aid in moving heavy objects both physical and intellectual, and especially to Dr. John S. Winn, Mr. Ralph S. Terkowitz, and Dr. James Farrar;

To staff of the Lawrence Berkeley Laboratory and the University of California too numerous to mention, for the cheerful application of their exceptional expertise, but most of all to Mr. Howard Wood and Mr. Phil Eggers, patient guides through the mysteries of mechanical and electronic fabrication;

To Ms. Nancy Monroe, for the illustration of this dissertation, and to Ms. Cordelle Yoder, for the typing as well as her many other kindnesses;

And, to the Department of Chemistry, University of California; to the Standard Oil Company of California; and

to the Lawrence Berkeley Laboratory, Energy Research and Development Administration (under whose auspices this work was conducted), for financial support;

I gratefully acknowledge my debt.

# TABLE OF CONTENTS


| CHAPTER | | Page |
|---|---|---|
| I | BACKGROUND. . . . . | 1 |
| | A. Introductory Remarks. . . . . | 1 |
| | B. Reactions Kinematics. . . . . | 2 |
| | C. Reaction Models . . . . . | 9 |
| | References. . . . . | 16 |
| II | EXPERIMENTAL. . . . . | 17 |
| | A. Apparatus . . . . . | 17 |
| | B. Data Collection and Processing. . . . . | 25 |
| | C. Considerations of Resolution and Error. | 28 |
| | References. . . . . | 36 |
| III | FEATURES OF THE $(N+H_2)^+$ SYSTEM. . . . . | 37 |
| | A. Potential Surface . . . . . | 37 |
| | B. Relation to Previous Studies. . . . . | 45 |
| | References. . . . . | 52 |
| IV | RESULTS . . . . . | 54 |
| | A. Scope and Presentation. . . . . | 54 |
| | B. Reactive Scattering . . . . . | 56 |
| | C. Non-Reactive Scattering . . . . . | 76 |
| | References. . . . . | 87 |
| V | CONCLUSIONS . . . . . | 88 |
| | A. General Observations. . . . . | 88 |
| | B. Collinear Sequential Collisions . . . . | 93 |
| | C. Three-Dimensional Sequential Collisions | 101 |

TABLE OF CONTENTS (continued)


| CHAPTER | | Page |
|---|---|---|
| V | CONCLUSIONS (continued) | |
| | D. Preliminary Application to the Experimental System . . . . . | 117 |
| | E. Refinement of the Model . . . . . | 138 |
| | F. Summary of Conclusions. . . . . | 146 |
| | References. . . . . | 148 |
| APPENDIX | | |
| A | THE "WRONG-ATOM" SEQUENTIAL IMPULSE MODEL . . | 149 |
| B | LISTING OF PROGRAM SIMPLOT. . . . . | 155 |

# CHAPTER I

# BACKGROUND

## A. Introductory Remarks

Chemical reactions which occur in nature are remarkable for their complexity. The combustion of wood in air, for example, involves an almost innumerable array of chemical species, both as reactants and as products; each species in turn reacts under a wide variety of conditions and environments; and each of these cases involves a number of quantum states. The history of chemical kinetics, and even of chemistry itself, involves in large part the successive removal of these layers of complexity. The ultimate goal in this process is to observe the interaction of reactants of precisely determined relative energy and internal states, reacting to yield products of equally precise characterization, under completely defined conditions.

Molecular beam techniques have allowed a close approach to this goal. It is now common to study reactions in which the initial relative energy and quantum states of the reactants are quite accurately defined, and the energy and angular distributions of the reactants are observable; even further refinements have been achieved under certain circumstances. This work will apply these methods to the study of the $N^+(^3P)$ ion in collision with He, $H_2$, HD, and $D_2$ molecules in their room-temperature equilibrium state

populations. The distributions in energy and in angular deflection of the reactive and non-reactive ionic products will be measured, and the results applied to elucidate features of the potential surface for the reaction.

## B. Reaction Kinematics

Our goal in this work is to interpret distribution of products from a scattering event in terms of the detailed mechanism of the reaction under study. First, however, we must examine the fundamental constraints on the product distribution imposed by the requirements of momentum and energy conservation. In order to do so, let us consider an arbitrary scattering event:

$$a + b \rightarrow c + d \qquad (1)$$

in which reactants a and b collide to produce products c and d. To reproduce our experimental conditions, we will let b be at rest relative to the laboratory and give a an initial velocity $v_a$. After collision, the products c and d will have laboratory velocities $v_c'$ and $v_d'$ respectively. Throughout this work, primes will indicate post-collision quantities. Also, we will use the letter a to represent both the species and the mass of the species a, and similarly for b, c, and d. This results in a simplification of notation; the context will serve to make the particular usage clear. For example, the laboratory energy $E_a$ of species a prior to collision may be written as:

$$E_a = \frac{a}{2} v_a^2. \tag{2}$$

Let M represent the total mass of the system:

$$M = a + b = c + d. \tag{3}$$

In addition to the laboratory-fixed (LAB) frame, it is useful to refer to the center of mass (CM) frame of reference. This frame has its origin at the center of mass of the collision system and thus moves relative to the LAB frame with a velocity $\vec{v}_{cm}$. This velocity may be expressed in terms of $\vec{v}_a$ by recalling that the total momentum of a system of particles is equal to the system mass times $v_{cm}$.[1] Therefore:

$$M\vec{v}_{cm} = a\vec{v}_a \tag{4}$$

and,

$$\vec{v}_{cm} = \frac{a}{M} \vec{v}_a. \tag{5}$$

To distinguish velocities measured in the CM frame, we shall use the letter u with the appropriate subscript; e.g., $u_a$ and $u_c'$. Two other coordinates should also be defined: the LAB and CM scattering angles $\theta$ and $\chi$ respectively. The LAB scattering angle $\theta$ is the angle between the vector post-collision velocity $\vec{v}_c'$ and the initial velocity $\vec{v}_a'$; similarly, $\chi$ is the angle between $u_c'$ and $u_a$. We can express our initial conditions in terms of CM velocities by writing:

$$\vec{u}_a = \vec{v}_a - \vec{v}_{cm} = \frac{b}{M} \vec{v}_a \tag{6}$$

$$\vec{u}_b = -\vec{v}_{cm} = -\frac{a}{M} \vec{v}_a. \tag{7}$$

These relationships are illustrated graphically in Figure 1.

The CM frame is particularly convenient for expressing the conservation of momentum restrictions on $u'_c$ and $u'_d$. We note that the initial CM momenta sum vectorially to zero:

$$a\vec{u}_a + b\vec{u}_b = 0. \tag{8}$$

After collision, the same must be true; thus:

$$c\vec{u}'_c + d\vec{u}'_d = 0. \tag{9}$$

Therefore specification of either of $u'_c$ or $u'_d$ uniquely specifies the other.

Energy conservation considerations are most conveniently handled by separating the total LAB kinetic energy before collision into the energy of the center of mass and the energy $E_{rel}$ of the reactants relative to the center of mass:[1]

$$E_a = \frac{M}{2} \vec{v}^2_{cm} + E_{rel} \tag{10}$$

whence $E_{rel}$ is easily found to be:

$$E_{rel} = \frac{b}{M} E_a. \tag{11}$$

Since, in the absence of outside forces, the system mass and momentum are invariant, the first term on the right in equation (10) is fixed and only the relative energy is available to do work on the system. We may therefore restrict our attention henceforth to $E_{rel}$.

Energy conservation produces the following expression:

$$E_{rel} + U = E'_{rel} + U' + \Delta E^o_o \tag{12}$$

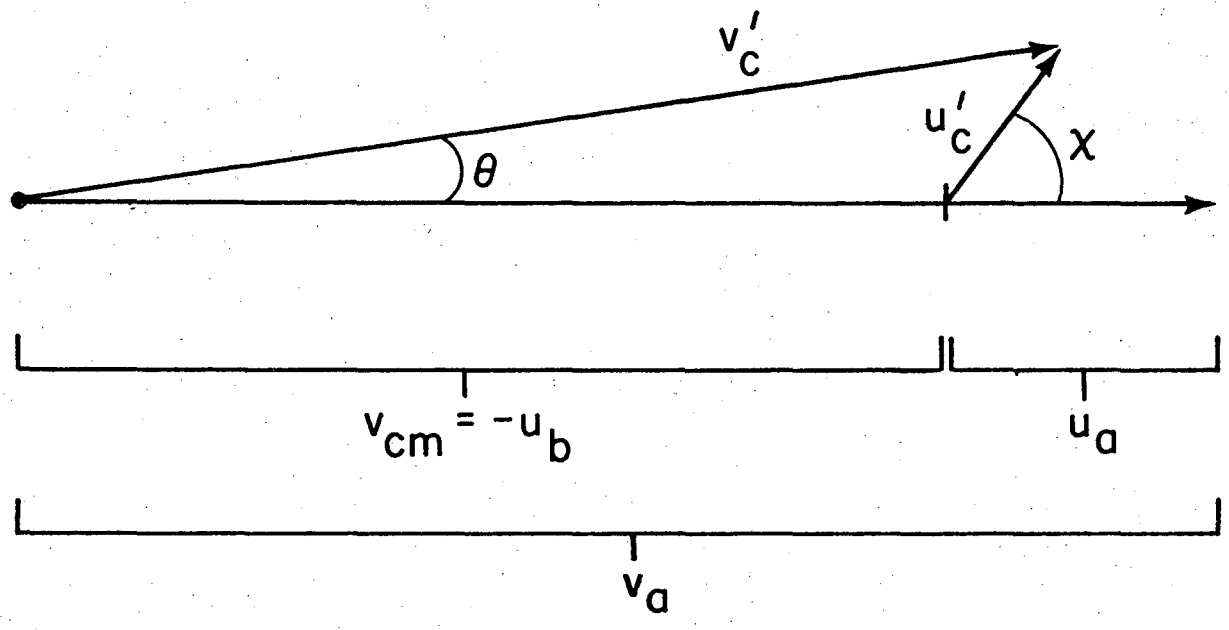


XBL 765-1773

Figure I-1. Velocity vector diagram for a + b → c + d.

where $E'_{rel}$ and $E'_{rel}$ are the CM kinetic energies before and after collision, U and U' are the internal energies of the reactants and products respectively, and $\Delta E^o_o$ the heat of the reaction under study. We can define the translational exoergicity, Q, by:

$$Q = E'_{rel} - E_{rel}. \tag{13}$$

Equation (12) then becomes:

$$Q = U - U' - \Delta E^o_o. \tag{14}$$

In addition, we may write Q as a function of the velocities $u_a$ and $u'_c$, using the definitions of kinetic energy in terms of velocity, and removing $u_b$ and $u'_d$ through the momentum conservation expressions (8) and (9). The result is:

$$Q = \frac{cM}{2d} u_c'^2 - \frac{aM}{2b} u_a^2. \tag{15}$$

This relation shows that, for a given initial velocity, $u'_c$ vectors of equal magnitude imply equal Q values. If the $u'_c$ values of products from a single experiment are plotted, then lines of constant Q will be represented by circles drawn about the CM origin.

By considering the restrictions on the quantities U and U' in equation (14), we may obtain upper and lower bounds for Q in any given reaction. We shall deal with reactants which are essentially in their ground vibrational and rotational states, so that U may be taken as zero, with the exception of a possible electronic term. By considering varying electronic states to represent different species, we

may absorb any electronic excitation into the heat of reaction, and set U equal to zero for our purposes. In addition, we shall deal with three-body events, so that either species c or d will be an atom, and have no internal energy. U' will then be limited to values between 0 and the dissociation energy of the diatomic species, $D_o^o$, if stable diatomic product is to exist. That is:

$$0 \leq U' \leq D_o^o \tag{16}$$

which implies that:

$$-\Delta E_o^o \geq Q \geq -D_o^o - \Delta E_o^o. \tag{17}$$

(Similar restrictions would exist, of course, without the simplifying assumptions of this paragraph, but more quantities would be required to express them.)

These limits are best illustrated using a velocity vector diagram known as a Newton diagram. An example of such a diagram has already been introduced as Figure 1. Figure 2 shows such a diagram for elastic, inelastic-nonreactive, and reactive events. In Figure 2a, an elastic event is illustrated: a = c, b = d, and Q = 0. Thus, by equation (15), $u_a$ and $u_c'$ are identical, and the scattered product may appear anywhere on a circle (the "elastic circle") drawn through the initial a velocity and about the center of mass. In Figure 2b, a non-reactive, inelastic event occurs: a and c are still identical, but Q is less than zero. The scattered product is thus found within the elastic circle. In

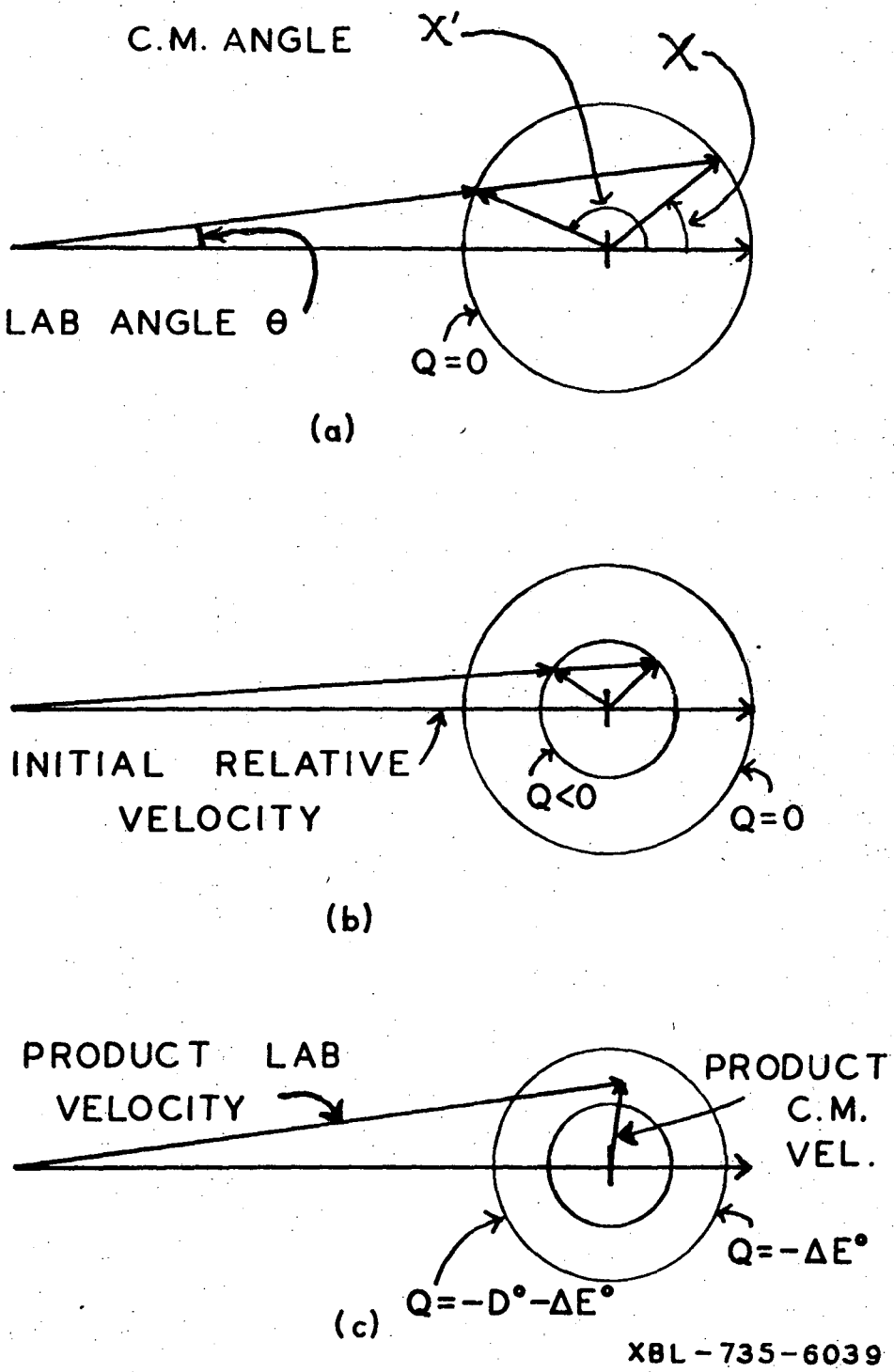


Figure I-2. Newton diagrams for three types of scattering: (a) non-reactive elastic; (b) non-reactive inelastic; (c) reactive.

Figure 2c, the reactive case is treated. The elastic circle of Q = 0 still exists, but its location is no longer obvious by inspection. Depending on the mass ratios in equation (15) and the heat of reaction, $u_c'$ may be greater than or less than $u_a$ for elasticity.

Figure 2 also shows the LAB velocity vectors $v_c'$ for the three types of events, together with the LAB and CM scattering angles $\theta$ and $\chi$. It is worth noting that in all cases, $v_c'$ is restricted to a relatively small area about $v_{cm}$. In the non-reactive case, for example, the elastic circle is an outer bound to the product, and $\theta$ is restricted to:

$$\theta \leq \sin^{-1} \frac{v_{cm}}{u_a} = \sin^{-1} .b/a. \qquad (18)$$

It is also clear from the figure that, in general, two values of $\theta$ may correspond to one value of $\chi$, although the associated $\vec{v}_c'$ vector will differ in magnitude.

## C. Reaction Models

The conservation laws ordain the broad outlines of the product distributions; the finer details are imposed by the mechanism of the reaction concerned. A number of simple models have been proposed to explain various observed product distributions. Several of these models may be classified as direct models, signifying that they assume that the interaction time between reactants is short in comparison to a rotational period. To describe these models we will consider

a more particular case of reaction (1), namely the generalized reactive triatomic collision:

$$A + BC \rightarrow AB + C \tag{19}$$

and use the conventions for mass and velocity developed in the previous section.

Of particular interest is the "spectator stripping" model.[2-5] In this model, the A atom is assumed to collide only with atom B, imparting no momentum to atom C. Atom C is thus a "spectator" of the collision, whence the name of the model. As a result, the AB product must be produced with the velocity of the A-B center of mass, so that:

$$(\vec{v}'_{AB})_{SS} = \frac{A}{A+B} \vec{v}_A. \tag{20}$$

The internal excitation must equal the energy of A relative to B, so:

$$Q_{SS} = - \frac{B}{A+B} E_A. \tag{21}$$

The product will thus be produced at an angle $\chi = 0°$ in the CM frame with a velocity:

$$(\vec{u}'_{AB})_{SS} = (v'_{AB})_{SS} - v_{cm} = \frac{AC}{(A+B)(B+C)} u_A. \tag{22}$$

In a related model, the "ideal rebound" model, the A atom is conceived of as reacting completely inelastically with the B atom, and then the AB product collides elastically with the C atom. As in the spectator stripping model, the internal excitation is the energy of A relative to B:

$$Q_{RB} = \frac{B}{A+B} E_A. \tag{23}$$

However, the product is formed with a velocity less than that of the center of mass:

$$(v'_{AB})_{RB} = \left(\frac{A+B-C}{A+B+C}\right)\left(\frac{A}{A+B}\right) v_A \tag{24}$$

and therefore at a CM angle of 180° and a CM velocity of:

$$(u'_{AB})_{RB} = \frac{AC}{(B+C)(A+B)} u_A. \tag{25}$$

This model may be generalized by allowing AB collisions with C leading to CM scattering angles other than 180°. The product may then appear at any angle on the Q circle given by equation (23). This generalization is the "elastic spectator" model.

A third impulsive model assumes that A first collides impulsively and elastically with atom C, ejecting the C atom and rebounding itself. It then reacts inelastically with the B atom to form the product. This is the "ideal knockout" model.[6-8] In the first step of the model, atom A with speed $v_A$ collides head-on with atom C with speed zero, so that the center of mass of the A-C pair moves with velocity $(A/(A+C))v_A$. The relative velocity of A relative to the A-C centroid is now $(C/(A+C))\ v_A$. After the collision, the A velocity relative to the A-C centroid is reversed, and the laboratory A velocity $v'_A$ is given by:

$$v'_A = \frac{Av_A}{A+C} - \frac{Cv_A}{A+C} = \frac{A-C}{A+C} v_A. \tag{26}$$

The A atom then combines with the B atom, which has remained at rest in the laboratory. Its laboratory momentum is zero, and the sum of the momenta of A and B represent the lab A-B momentum:

$$(A+B)\ v'_{AB} = A\left(\frac{A-C}{A+C}\right) v_A \tag{27}$$

so that the AB product appears at the lab velocity:

$$(v'_{AB})_{KO} = \left(\frac{A}{A+B}\right)\left(\frac{A-C}{A+C}\right) v_A. \tag{28}$$

This product will thus lie behind the center of mass of the system, with $\chi = 180°$; by subtracting $v'_{AB}$ above from the centroid velocity we can obtain an AB velocity in the CM frame of:

$$(U'_{AB})_{KO} = \frac{AC(A-2B+C)}{(A+C)(A+B)(B+C)} U_A. \tag{29}$$

The Q value predicted by this model is perhaps most easily obtained by accounting for the other energy terms. After the A-C collision, the total energy of the system is the sum of the A and C kinetic energies. After A and B combine, the total energy is the sum of the AB kinetic energy, the (unchanged) C kinetic energy, and the internal energy -Q. Thus:

$$\frac{C}{2} v'^2_C + \frac{A}{2} v'^2_A = \frac{C}{2} v'^2_C + \frac{A+B}{2} v'_{AB} - Q_{KO} \tag{30}$$

or:

$$Q_{KO} = \frac{A}{2} v'^2_A - \frac{A+B}{2} v'^2_{AB}. \tag{31}$$

Substituting from equations (26) and (28),

$$Q_{KO} = \frac{A}{2}\left(\frac{A-C}{A+C}\right)^2 v_A^2 - \frac{A+B}{2}\left(\frac{A}{A+B}\right)^2\left(\frac{A-C}{A+C}\right) v_A^2, \qquad (32)$$

or, factoring out the initial energy $E_A = \frac{1}{2} Av_A^2$:

$$Q_{KO} = \frac{B}{A+B}\left(\frac{A-C}{A+C}\right)^2 E_A. \qquad (33)$$

The predicted velocities and Q values for the models are collected in Table I-I.

We shall deal with the effectiveness of these models in explaining observed scattering in actual systems later in this thesis. At this point, however, it is interesting to note that the predicted Q value for each model becomes increasingly negative with increasing $E_A$. As a result, for each model there is a value of $E_A$ at which Q no longer falls within the limits of equation (17), and product is no longer stable to dissociation according to that model. Behavior at this point turns out to be of considerable interest in classifying ion-molecule reactions.

Each of the models so far examined has been characterized by a marked peaking of product either forward or backward of the center of mass. Markedly contrasting behavior is predicted by the collision complex model.[9-12] In this model, the colliding species remain in close contact for several rotational periods before dissociating in a statistical manner to products. (The word complex is used here to identify this close association, and implies no special

Table I-I

Kinematics of Several Impulsive Models

| Model | $\chi_{AB}$ | $v'_{AB}/v_A$ | $u'_{AB}/u_A$ | $-Q/E_A$ |
|---|---|---|---|---|
| Spectator Stripping | 0° | $\frac{A}{A+B}$ | $\frac{AC}{(A+B)(B+C)}$ | $\frac{B}{A+B}$ |
| Rebound | 180° | $\frac{A}{A+B}\left(\frac{A+B-C}{A+B+C}\right)$ | $\frac{AC}{(A+B)(B+C)}$ | $\frac{B}{A+B}$ |
| Knockout | 180° | $\frac{A}{A+B}\left(\frac{A-C}{A+C}\right)$ | $\frac{AC}{(A+B)(B+C)}\left(\frac{A+C-2B}{A+C}\right)$ | $\frac{B}{A+B}\left(\frac{A-C}{A+C}\right)^2$ |

assumptions regarding the configuration or future behavior of the atoms involved.) As a result, the uniqueness of the original direction of motion is lost, and product is equally likely to be ejected in either the forward or backward direction. Due to the possible coupling of momenta within the complex, it is not a necessary consequence that the product be isotropically distributed about the center of mass; it is, however, required that the product be symmetric about the $\chi = \pm 90°$ line. Rigorously, such a distribution is a necessary but not sufficient condition for the existence of a complex mechanism; practically, alternative explanations are sufficiently unlikely that forward-backward symmetry is usually accepted as conclusive evidence of complex formation.[13]

## References


1. Jerry B. Marion, Classical Dynamics of Particles and Systems, Academic Press, New York (1970), pp. 81-84.

2. A. Henglein, K. Lacman and B. Knoll, J. Chem. Phys. 43, 1048 (1965).

3. A. Henglein, Adv. Chem. Ser. 58, 63 (1966).

4. R. L. Champion, L. D. Doverspike, and T. L. Bailey, J. Chem. Phys. 45, 4377 (1966).

5. W. R. Gentry, E. A. Gislason, B. H. Mahan, and Chi-Wing Tsao, J. Chem. Phys. 49, 3058 (1968).

6. E. A. Gislason, Bruce H. Mahan, Chi-Wing Tsao and A. S. Werner, J. Chem. Phys. 50, 142 (1969).

7. R. J. Cross and R. Wolfgang, J. Chem. Phys. 35, 2002 (1961).

8. J. Light and J. Horrocks, Proc. Phys. Soc. (London) 84, 527 (1964).

9. E. A. Gislason, B. H. Mahan, C-W. Tsao and A. S. Werner, J. Chem. Phys. 50, 5418 (1969).

10. W. B. Miller, S. A. Safron and D. R. Herschbach, Disc. Faraday Soc. 44, 108 (1967).

11. I. Halpern and V. M. Strutinski, Paper P/1513, Proc. Intern. Conf. Peaceful Uses Atomic Energy, 2nd Conf. (Geneva, 1958).

12. S. Safron, N. Weinstein, D. Herschbach and J. Tully, Chem. Phys. Lett. 12, 564 (1972).

13. Zdenek Herman and Richard Wolfgang, in Ion-Molecule Reactions, J. L. Franklin, editor, Plenum Press, New York (1972), p. 572.

# CHAPTER II

# EXPERIMENTAL

## A. Apparatus

The apparatus used in this work has been previously described in detail.[1] Therefore, only a brief account will be undertaken here. A schematic diagram of the apparatus is given in Figure II-1. As can be seen, it consists of an ion source, an ion beam focusing section, a scattering region, a product analysis section, and a detector.

The experiments in this work were all performed with a microwave discharge ion source. In this source, a suitable gas flows through a quartz tube, which is surrounded by a Broida cavity of the type described by Fehsenfeld, et al.[2] Microwave power radiated by the cavity sustains a discharge in the gas, which is maintained at a pressure on the order of 10-100 microns. Microwave power is supplied to the cavity by a 3 GHz commercial diathermy power source. Two electrodes serve to contain the discharge and establish the potential of the plasma. One electrode is mounted directly on the inlet flange of the apparatus, and has a 2 mm hole to allow gas flow and ion extraction. The other is suspended in the tube, and is perforated to allow for gas flow.

A minor modification was made to the source to allow the easy removal and replacement of the rear discharge electrode. Previously, the electrode was made of platinum

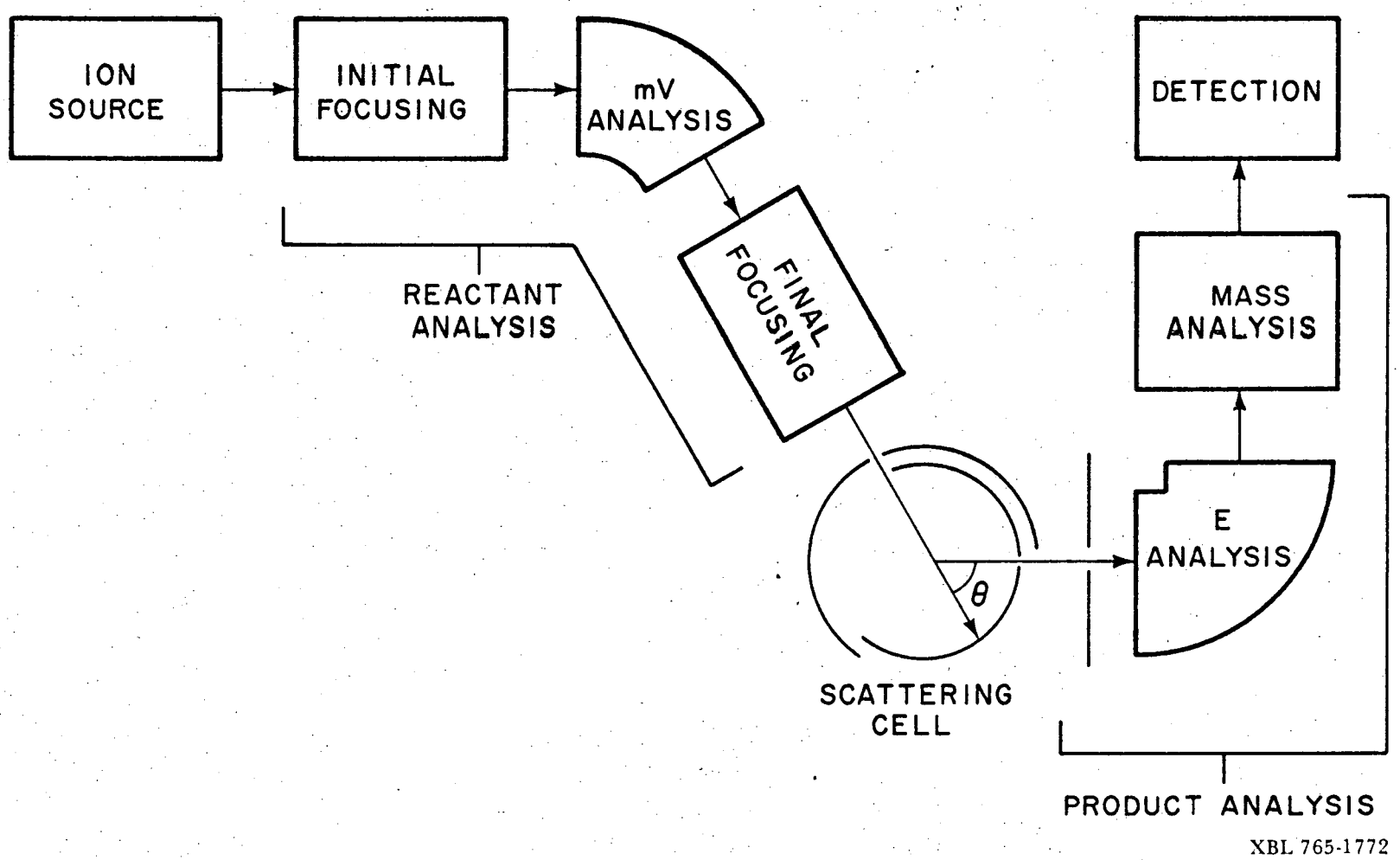


Figure II-1. Schematic diagram of the experimental apparatus.

and sealed permanently into the quartz tube. The modified configuration uses an o-ring seal to connect the rear of the tube to a small chamber containing the gas inlet and a device for suspending the electrode. This allows easy replacement of electrodes, and facilitates experimentation with various electrode materials. While of limited importance in studying the nitrogen system, this capability has proven valuable in exploratory studies of halogen ions.

For the routine production of nitrogen ions, we used a mixture of nitrogen and helium in about 9:1 proportion as measured by an ionization gage. The electrodes were made of stainless steel. The best available ion currents proved to be about 0.1 to 0.03 times the $O^+$ currents available with the source, with a concomitant reduction in the apparatus resolution. Winn[3] has speculated that production of the monatomic oxygen ion proceeds by a two-step process involving dissociation of the $O_2$ molecule (minimum energy 5.1 eV) followed by ionization (minimum energy 13.6 eV). If so, the higher dissociation energy of $N_2$ (~9.8 eV) would explain the reduced amount of $N^+$ ion produced.

The advantage of this type of source over the more traditional electron impact method lies in the relative mildness of the ionization environment. While electron impact ionization usually required electron energies on the order of 100 volts, the electron temperature in our source is about five volts.[3] As a result, few if any of the ions produced should be in an excited electronic state. This

conclusion is supported by two previous studies with this source involving $O_2^+$ and $O^+$. For $O_2^+$, the first ionization potential is 12.2 eV and the excitation energy of the first excited state is 3.8 eV. Chiang et al.[4] found only 3% excited $O_2^+$ in this case. For $O^+$, the equivalent energies are 13.6 eV and 3.3 eV. Winn concluded that the resulting $O^+$ beam was "nearly pure" ground state ion.[3] We therefore expect the $N^+$ ion beam used in this study to be predominantly in the ground state.

The question of excited states was dealt with more directly in this work by the use of alternate gas combinations as $N^+$ sources. Based on appearance potentials compiled by Franklin et al., the gases $NH_3$ and $N_2O$ might be expected to produce at least some ion in the excited $^1D$ state.[5] These gases were diluted in a large amount of argon (about 20:1 proportion as measured by an ionization gage), and the resulting mixture used to support a microwave discharge. In both cases, a $N^+$ beam of comparable intensity and stability to that obtained from the microwave discharge of $N_2$ was observed. The results of this substitution will be presented in Section C of this chapter.

Ions are extracted from the source region and formed into a collimated, monoenergetic beam by the focusing section, which is illustrated in Figure II-2. The energy of the ion beam is determined by the voltage applied to the ion source electrodes and by the discharge plasma potential. Other focusing voltages are referenced to the ion energy voltage

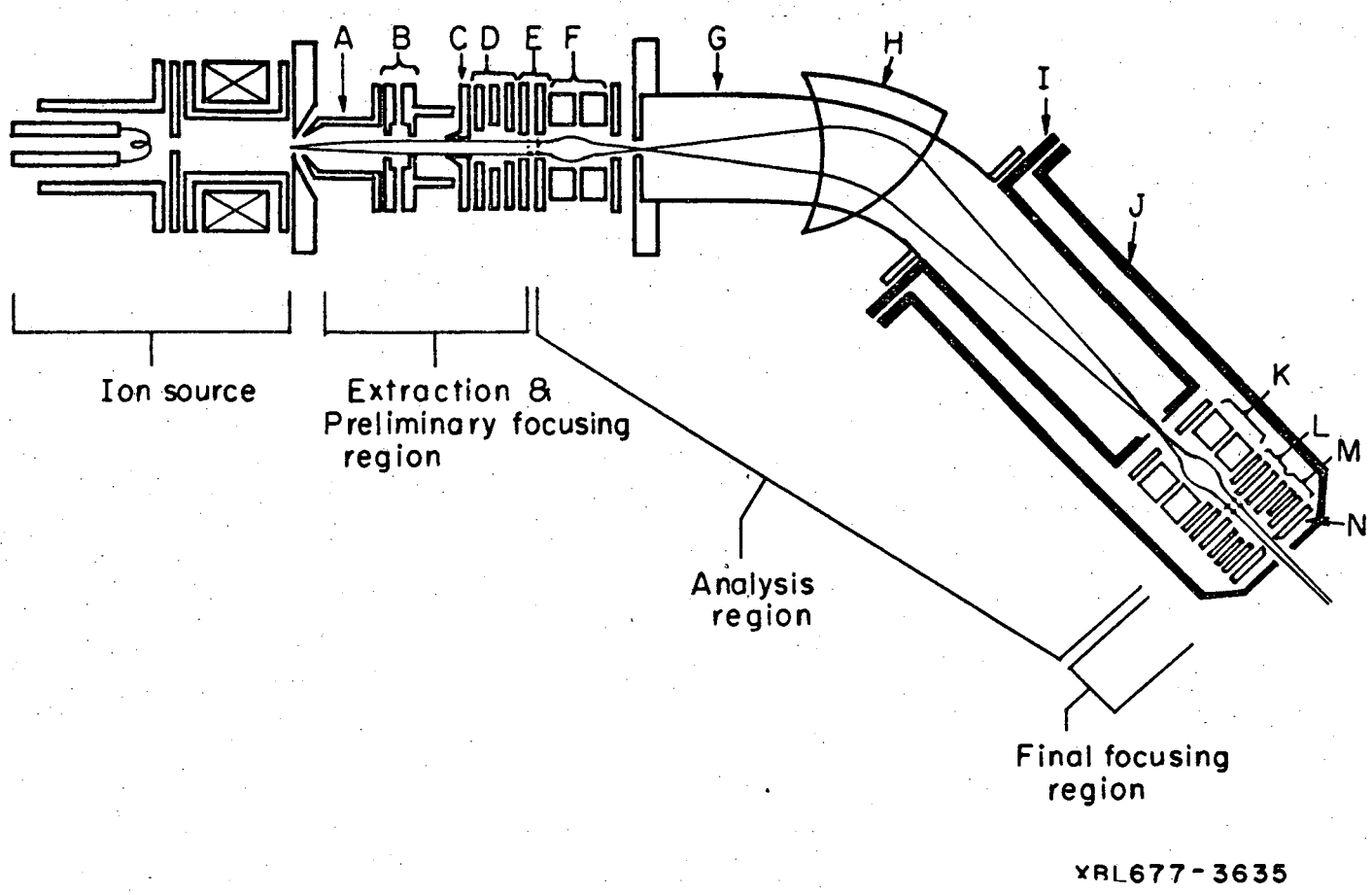


Figure II-2. Details of the reactant focusing region. A microwave discharge source is substituted for the electron impact source shown.

so that focusing conditions are relatively insensitive to the energy setting. An initial focusing stage extracts the ions and focuses them onto the entry slit of a 66° magnetic mass spectrometer, which serves as a momentum analyzer. A pair of quadrupole lenses in the initial focusing stage transforms the beam from a cylindrical to a ribbon-like configuration for maximum transmission through the analyzer. The geometry of the analyzer produces a momentum resolution of 2% FWHM. The analysis voltage may be varied independently of the ion energy for maximum efficiency of analysis. Following analysis, the beam is reconverted to a roughly circular cross-section and focused on the scattering region by the final focusing stage.

Provided that the mass of the extracted ions is fixed, the momentum analyzer serves to produce a monoenergetic beam. On the other hand, if the discharge region is monoenergetic, the analyzer serves as a mass selector. In practice, the beam is essentially fixed both in mass and energy, since the discharge region is equipotential to good accuracy. However, some mass impurities may be passed by the filter: the effect of these minor contaminants are discussed in Section C of this chapter.

Reaction with the neutral gas takes place in the scattering region within the main vacuum chamber of the apparatus. All of our experiments were carried out using a scattering cell to contain the reactant gas. The "front" aperture, a 2 x 2 mm square, is fixed in line with the exit

point of the focusing section, and receives the incident beam. The rear aperture is a 2 mm diameter circle which may be rotated. It is positioned in line with the detector aperture, so that the two rotate together to scan the angular distribution of products. The apertures are conical to reduce streaming of the scattering gas into the path of the beam,[6] and allow cell pressures to exceed the vacuum chamber background pressure by a factor of about 1,000.

Gas enters the cell through an entry pipe from the lid of the apparatus. The pressure is regulated using a Granville-Phillips variable leak, and is monitored with a MKS Baratron capacitance manometer. The manometer reading represents the pressure at the top of the entry pipe, and must be corrected to obtain the absolute pressure in the cell itself. Since only relative pressures are usually of interest in this work, the correction is omitted unless otherwise stated. It is worth noting that the manometer reads true (mechanical) pressure and is thus unaffected by the nature of the gas measured.

The product analysis section provides angular, energy, and mass characterization of the scattered products. Angular resolution is obtained by rotating the detector in alignment with the exit aperture of the scattering cell: the cell and detector aperture dimensions determine a 2.5° resolution at full width. A 90° spherical sector electrostatic energy analyzer then selects ions of a desired energy with a resolution of 3% FWHM. Ions leaving the energy analyzer are

focused by a set of lenses into a quadrupole mass spectrometer (QPMS) which rejects all ions not of a preset charge-to-mass ratio. The resolution of the QPMS is adjustable, and is set for a FWHM of about 1/2 mass unit for this work. A second set of lenses then focuses the mass-analyzed ions into the detector. The detector counts individual ion impacts.

The detector is of the scintillation type, and represents a modification of the apparatus from previous reports. The basic design and operation of scintillation detectors is well documented.[7,8] This particular detector was designed by Dr. James A. Farrar of this lab and will be described by him in a forthcoming report.[9] In this detector, the incoming ions are first attracted to a metal plate held at a voltage of -25 kV, causing the ejection of secondary electrons. The plate voltage then accelerates the electrons towards a sheet of scintillating material, which emits a burst of photons. A phototube then responds to the photon burst by producing a pulse which is recorded by counting equipment. The counting equipment is that previously employed with the solid-state detector.

The principal advantage of the scintillator over the solid-state detector is operational simplicity. The scintillator operates at room temperature with no warmup time, while the solid-state detector requires cooling to liquid nitrogen temperature. Also, the scintillator does not involve the replacement of sensitive and expensive

semiconductor wafers. In addition, the scintillator is capable of a slightly higher counting rate. In exchange, the new detector has a slightly higher noise level. However, the variation in the number of background counts between successive thirty-second collection periods is still no greater than one count per second.

## B. Data Collection and Processing

To conduct an experiment, it is first necessary to obtain a stable and intense beam of the required mass and energy. This is done by adjusting the potentials on the various ion lenses and electrodes until the desired result is obtained. The beam intensity may be monitored by connecting the ion lenses following the energy analyzer in the product analysis train to an electrometer. The electrometer current thus represents an angular- and energy-analyzed measure of the beam intensity.

When a stable beam is obtained, scattering gas is admitted to the scattering cell and the analysis and detection equipment energized. The scattering gas pressure is adjusted to provide about 15% attenuation of the incident beam: multiple scattering events are therefore negligible.

A single data point is obtained by setting the analysis energy, angle, and mass to the desired values and counting the ions impacting on the detector during a known time. A sequence of such observations thus provides a set of numbers representing scattered ion intensities as a function of beam

energy; product mass, angle and energy; counting time and scattering gas pressure. The last two of these quantities, along with the number of counts observed, are automatically recorded on a teletypewriter; the other variables are entered by hand. A typical scattering map contains several hundred such observations.

In addition to product scattered from within the scattering cell, some ions will reach the detector following collisions between the beam and the background gas in the vacuum chamber. To account for these spurious incidents, background observations are conducted. These involve repeating a series of observations with the scattering cell emptied. Scattering gas is leaked into the chamber until the chamber pressure, as measured with an ionization gage, is equal to the chamber pressure observed with the scattering cell filled. The background intensities observed are subtracted from the equivalent signal intensities during data analysis.

While in principle observations can be made in any order, it is most efficient to minimize the number of settings which must be changed between each point. When a complete scattering map is to be made, this is best accomplished by fixing the product energy while varying the angle over the range to be observed. This procedure is referred to as a "cut," and most of the data to be presented here is made up of cuts. To avoid systematic errors, an effort is made to make cuts in both directions (ascending and descending angle)

and in a random order of energies. Nevertheless, in examining the data, it is well to realize that points of constant laboratory energy are more likely to be subject to a constant systematic error than points of equal laboratory angle. Background observations are usually made in a second cut immediately following the relevant signal cut.

It is not possible to monitor the incident beam intensity during the collection of data, since any such measurement would absorb or deflect the beam. Therefore the collection of data is interrupted periodically (about every 30-45 minutes) and the beam intensity observed. These measurements serve to normalize the data.

Data is processed using a FORTRAN program written for the Lawrence Berkeley Laboratory's CDC 7600 electronic computer. The program input includes all of the observed quantities listed in the preceding paragraphs. The program then produces, for each data point, an intensity $\bar{I}$ given by:

$$\bar{I} = 10^7 \frac{(S-B)f(\theta)}{Ti_o PE^{3/2}} \qquad (1)$$

where:

$S$ = number of signal counts

$B$ = number of background counts

$T$ = counting time, in seconds

$i_o$ = incident beam intensity, in picoamps

$P$ = scattering gas pressure, in units of $6 \cdot 10^{-6}$ torr[10]

$E$ = energy setting of the energy analyzer, in volts

$f(\theta)$ = detector angular viewing factor.

The background level B is set by the program to a nominal value in the absence of a higher observed reading; the nominal value is a program input, determined as described in Section C of this Chapter. When successive observations of $i_o$ differ, the program assumes the change between observations to have been linear and calibrates $\bar{I}$ accordingly. Due to the geometry of the energy analyzer, E is related to the LAB energy of the transmitted ions by:

$$E = 0.44\ E'_{AB}. \qquad (2)$$

The quantity $\bar{I}$ has been shown to be invariant to the CM to LAB coordinate conversion.[11]

The program then produces table of $\bar{I}$ together with the input quantities and useful derived quantities both in the LAB and CM frames. These tables are also copied to an IBM Datacell in the LBL Computer Center, where they are accessible to other programs for further analysis. Finally, the program plots values of $\bar{I}$ in CM polar coordinates. A second plot symmetrizes the first about the beam centerline to remove the effects of minor apparatus asymmetries. From the plots, one can draw contour maps of $\bar{I}$, which represent the primary results presented in this work.

## C. Considerations of Resolution and Error

The basic data of this work are contour maps of the quantity $\bar{I}$ (X, u'). It is therefore appropriate to address the resolution of the apparatus with respect to each of the

quantities $\bar{I}$, $\chi$, and u' separately. The last two of these are in turn determined by the laboratory quantities $\theta$ and $E'_{AB}$.

Resolution in laboratory angle $\theta$ is fundamentally limited to the $\pm 1.25°$ limit determined by the cell and detector apertures. In addition, it may be further restricted by the uncertainty in the angular location of the primary beam, and by the symmetrizing process in the production of the map plots.

The width of the beam is usually less than 2° FWHM, or comparable to the detector resolution. Small variations in the beam angle have been observed in the course of an experiment: they do not exceed a few tenths of a degree. In the process of building the symmetrized plot, the computer program interpolates between the angles of observed points which are not precisely symmetric about the centerline. This process may diminish resolution somewhat, but hardly by more than half the distance between points. This distance is one degree in all instances where angular resolution is an important concern. Our angular resolution is thus near the apparatus limit of 1.25°.

Energy resolution is subject to similar considerations. The instrument resolution is about ±1.5% of the LAB energy being observed. Beam widths are usually a fairly constant 1-2 volts HWHM, and variations of several tenths of a volt have been observed between cuts. The computer program performs no operations affecting energy resolution. The energy resolution is thus apparatus-limited at high energies (say $\geq$70 eV) to ±1.5% and becomes limited by beam width to about 1-2 eV at lower energies.

As Figure I-1 indicates, the effect on $\chi$ and u' of uncertainties in $\theta$ and E depends in an involved way on the actual coordinates involved. It is clear, however, that a fairly small range of coordinates in the LAB frame spans the entire allowed CM area. The actual expressions relating changes in ($\theta$, E) to those in ($\chi$, u) can be found to be:

$$du'/dE = \frac{1}{c} \frac{v'-v_{cm}\cos\theta}{v'\cdot y} \tag{3}$$

$$du'/d\theta = \frac{v'\cdot v_{cm}\sin\theta}{y} \tag{4}$$

$$d\chi/dE = \frac{1}{c} \frac{v_{cm}\sin\theta}{v'y^2} \tag{5}$$

$$d\chi/d\theta = \frac{v'}{v'\cos\theta - v_{cm}} \left(\cos\theta - \frac{\sin^2\theta v' v_{cm}}{y^2}\right) \tag{6}$$

where y is an expression defined by:

$$y^2 = v'^2 - 2v'v_{cm}\cos\theta + v_{cm}^2 \tag{7}$$

and the mass convention is identical to that of Chapter I, Section A. The quantity Q is frequently of more interest than u'; the equivalent expressions for Q are:

$$dQ/dE = -\frac{M}{d} \frac{v'-v_{cm}\cos\theta}{v'} \tag{8}$$

$$dQ/d\theta = -\frac{Mc}{d} (v'v_{cm}\sin\theta). \tag{9}$$

A better intuitive conception of the magnitudes involved can be obtained by concentrating on the area around the primary beam velocity, where $v' = v_a$ and $\theta = 0$. There the derivatives (4), (5), and (9) are zero, and expressions (3), (6), and (8) reduce to:

$$du'/dE = \frac{1}{cv'} \tag{10}$$

$$dX/d\theta = M/b \tag{11}$$

$$dQ/dE = b/d. \tag{12}$$

Thus dQ/dE ranges from 1 for non-reactive scattering to 3 for ND product from HD, and $dX/d\theta$ is 8 for a $H_2$ target and 4.5 for a $D_2$ target. The effect on CM resolution of the LAB resolution limits is increased accordingly.

The resolution of the instrument relative to $\bar{I}$ is more complicated, since it involves all of the quantities in equation (1). Most of these variables, however, are quite accurately known. Counting time is determined by the electronics of the counting equipment and is essentially exact. Gas pressure is read by the BARATRON to about one part in 300. The accuracy of the energy determination was previously discussed. The viewing factor is obtained graphically from the cell and detector dimensions and is in principle exact if the angle is known: the uncertainty in angle is discussed above and is of no significant effect.

Resolution in $\bar{I}$, in the sense of minimum detectable signal, is determined by the difference between signal and

background counts observed at the point (the quantity S-B in equation (1)). The background signal varies randomly due to noise and external radiation, and the size of this variation sets a minimum to the observable signal. Since the detector in use is new, we have carefully monitored the background under a variety of conditions. Variations are of course decreased by longer counting times: most of our observations involved times of 30 seconds, and the following figures pertain to that case. An essentially constant 1 cps is contributed by the detector with the electron emission cathode at ground potential. Field emission from the cathode contributes another five or so cps. The distribution of observations about this central value is approximately Gaussian with a half-width of 0.6-1.0 cps. The point in this distribution below which 80% of the observations lie has been taken as the nominal background value in this work; it is separately determined for each experiment. Thus the possibility of several higher-than-average backgrounds being mistaken for a significant feature is reduced. The minimum significant signal is therefore about 1-2 cps. The cross-section represented by this counting rate is of course a function of beam intensity and scattering gas pressure.

At signal levels significantly above noise, however, the reproducibility of $\bar{I}$ values is essentially determined by variations in the incident beam intensity $i_o$. The stability of the beam varies with the system under study and is usually improved with increased beam intensity. Experience with the

$N^+$ system (including the periodic intensity calibrations during experiments and continuous observation of beam stability when experiments are not in progress) indicates that during a cut beam stability is usually constant within 10%, but may occasionally vary as much as 30%. Thus, 30% is an upper found to the uncertainty of $\bar{I}$ at a single point.

The interpretation of a scattering map is not, however, dependent solely on the value of $\bar{I}$ at any one point. On the contrary, trends involving several points are always required to reach a conclusion. Without entering into a complicated analysis, it seems reasonable to assert that the perceived behavior of $\bar{I}$ at a map point is based on at least four independent measurements: the point as measured; the symmetric point (as $\theta \rightarrow -\theta$); the adjacent points on a line of constant lab energy, and the adjacent points of constant lab angle. It also seems reasonable to estimate the effect of additional determinations of a value by the relation valid for normal distributions: i.e., that uncertainty is inversely proportional to the square root of the number of observations. The uncertainty of a feature on a map can then be estimated as no greater than:

$$15\% = \frac{30\%}{\sqrt{4}} \qquad (13)$$

No important conclusion in this work is based on differences of less than a factor of 10 in $\bar{I}$.

At this point a possible systematic error should be considered. Our results are obviously quite sensitive to the

chemical and quantum purity of the primary beam. The quantum state of the reactant is not selected at any point in the reactant analysis, and is therefore dependent on the output of the source. We have described above evidence based on previous studies using this source for concluding that the reactant ion is predominantly in its ground state. In addition, in studies of the non-reactive scattering of $N^+$ off He, we observed no transitions except those involving the electronic ground state. By contrast, when Tsao conducted similar observations using an electron impact source with this instrument, transitions involving the excited ($^1D$) state of $N^+$ were observed.[12]

The $N^+$ beam composition has been more directly investigated using the attenuation method of Turner et al.[13] As applied on our apparatus, the method appears capable of resolving excited state concentrations with an accuracy of about 3% of the total beam intensity. Ion beams from electron impact were found to be about 15% excited. By contrast, the $N_2$ microwave discharge produced no detectable excited ion (<3%). Discharge of $NH_3$ in argon showed indications of an excited state concentration at the threshold of detectability (~3%), while the nitrous oxide-argon discharge produced about 6% excited ions.

In addition, the beam may be contaminated by several possible ions of similar masses. Since the source region is not ideally equipotential, small amounts of ions of neighboring masses may pass through the analysis magnet. Likely

candidates are the nitrogen isotopes $^{15}N$ (natural abundance 0.37%), and $^{16}O$, which may be present in the discharge region as an impurity from the atmosphere. These ions can be distinguished from product ions by two principal features. First, while product ion intensity decreases with decreasing scattering gas pressure, primary ion intensity increases. Secondly, these ions, having the same momentum but greater mass than the desired reactant, will be found at a lab energy given by the expression:

$$E_x = \frac{m_A}{m_x} E_A \qquad (14)$$

where $m_x$ and $E_x$ are the impurity mass and energy, and $m_A$ and $E_A$ the similar quantities for the primary ion.

Impurity ions have been observed at masses 15 and 16 in the course of this work. In each case they represented a maximum of a few tens of counts per second, in comparison with primary beams of at least $10^6$ ions per second. In these concentrations, the magnitude of scattering of the impurities is entirely negligible and background measurements serve to remove the spurious counts entirely.

## References


1. W. R. Gentry, University of California Lawrence Radiation Laboratory Report UCRL-17691 (1967).

2. F. C. Fehsenfeld, K. M. Evenson, and H. P. Broida, Rev. Sci. Instrum. 36, 294 (1965). Our cavity is similar to their cavity 5.

3. John S. Winn, Ph.D. Thesis, University of California LBL Report LBL-1820 (1973), p. 14.

4. M. H. Chiang, E. A. Gislason, B. H. Mahan, C. W. Tsao, and A. S. Werner, J. Phys. Chem. 75, 1426 (1971).

5. J. L. Franklin, et al., National Standard Reference Data Series, Vol. 26 National Bureau of Standards (U.S.), (1969).

6. I. Amdur and J. Jordan, in Molecular Beams, J. Ross, editor, Volume X of Advances in Chemical Physics, J. Wiley Interscience (1966), p. 51.

7. H. M. Gibbs and E. D. Cummins, Rev. Sci. Instrum. 37, 1385 (1966).

8. N. R. Daly, Rev. Sci. Instrum. 31, 264 (1960).

9. James M. Farrar, Lawrence Radiation Laboratory Report, to be published.

10. The unusual units of P result from the properties of the BARATRON digital readout. The scanner uses units of $10^{-2}$ volt; the BARATRON output is 5 volts full scale with a full scale reading of $3 \cdot 10^{-3}$ torr.

11. M. Chiang, E. A. Gislason, B. H. Mahan, C. W. Tsao, and A. S. Werner, J. Chem. Phys. 52, 2698 (1970).

12. Chi-Wing Tsao, Ph.D. Thesis, University of California LBL Report UCRL-19140 (1970), p. 47.

13. B. R. Turner, J. A. Rutherford, and D. M. J. Compton, J. Chem. Phys. 48, 1602 (1968).

# CHAPTER III

## FEATURES OF THE $(N+H_2)^+$ SYSTEM

### A. Potential Surface

The energetics of a chemical reaction are usually described in terms of its potential surface. In general, a system of $n$ particles requires $3n$ coordinates to specify its condition. When the absolute position of the system is not of importance, as is true in gas-phase kinetics, the three coordinates specifying the position of the system center of mass may be neglected. The energy of the system may be considered as a function of the remaining $3n-3$ coordinates. The resulting function constitutes a hypersurface in $(3n-2)$-space, referred to as the potential surface. The projections of this surface into two or three dimensions can be plotted graphically, and usually give considerable intuitive insight into the characteristics of the reaction.

In principle, the potential surface may always be obtained by solving the Schroedinger equation for the system. In practice, reliable approximations to the surface are extremely hard to obtain, even for the comparatively simple $A + H_2$ systems. In the case of ion-molecule reactions, the situation is further complicated by the existence of multiple low-lying electronic states, each giving rise to a separate potential surface which may interact with the others. It is

most useful, then, to have a method of predicting the main features of the reaction surface from basic principles.

An effective means of doing just that involves correlation diagrams. Proposed in a seminal paper by Mahan,[1] the technique has been applied with success to several experimental systems.[2-5] The only data required are the states of the products, reactants, and significant intermediate configurations, together with an ordering of them in terms of energy. Thermodynamic information about the actual relative energies of the states improves the precision of the results but is not essential. The method may be applied either to molecular states or orbitals, but experience has shown the state version to be more reliable.[3] We will therefore deal exclusively with state correlations in this work.

The first step is to assume a plausible geometry for the collision.[6] This geometry will then have certain symmetry elements, which can be used to identify it with one of the symmetry point groups of group theory. Group theory states, quite generally, that any entity with a symmetry corresponding to a point group can be expressed as a linear combination of the irreducible representations of that group. For instance, a molecular orbital may be expressible as the sum of several irreducible representations, each representing a separate potential surface. The representations are denoted by the familiar Toennies symbols (e.g., $^2\Pi_g$). To avoid a catastrophic descent into jargon, we shall refer to that component of a molecular state represented by the irreducible

representation $^2\Pi_g$, for example, as the $^2\Pi_g$ surface, or as having the symmetry $^2\Pi_g$.

Two general principles are now applied. The first is that the symmetry of the states is conserved throughout the collision. The other is that surfaces of the same symmetry do not cross.[7] As a result, the product and reactant states can be linked uniquely by a small number of lines, each representing a cut through a potential surface. These lines can be modified by plausible assumptions (either from chemical intuition or orbital correlations) about the behavior of the surfaces near the stable configurations. The result is a quite useful approximation to significant portions of the potential surface.

This somewhat abtruse discussion becomes more meaningful with the consideration of a concrete example. Figure III-1 displays the molecular state correlation diagram for the $NH_2^+$ system obtained by Mahan and Fair.[5] On both the extreme left- and right-hand sides are shown the energy levels for the low-lying states of $(N+H_2)^+$. On the left-hand side, it is assumed that the N atom approaches the $H_2$ molecule along the perpendicular bisector of the molecule. This geometry has the symmetry of the $C_{2v}$ point group, and the resolution of the states into the irreducible representations of that group is shown at the left of the diagram. The next column from the left shows the states of the bent intermediate $HNH^+$, and next to it are the linear $HNH^+$ states. The linear states are of $C_{\infty v}$ geometry, and are also special cases of $C_{2v}$

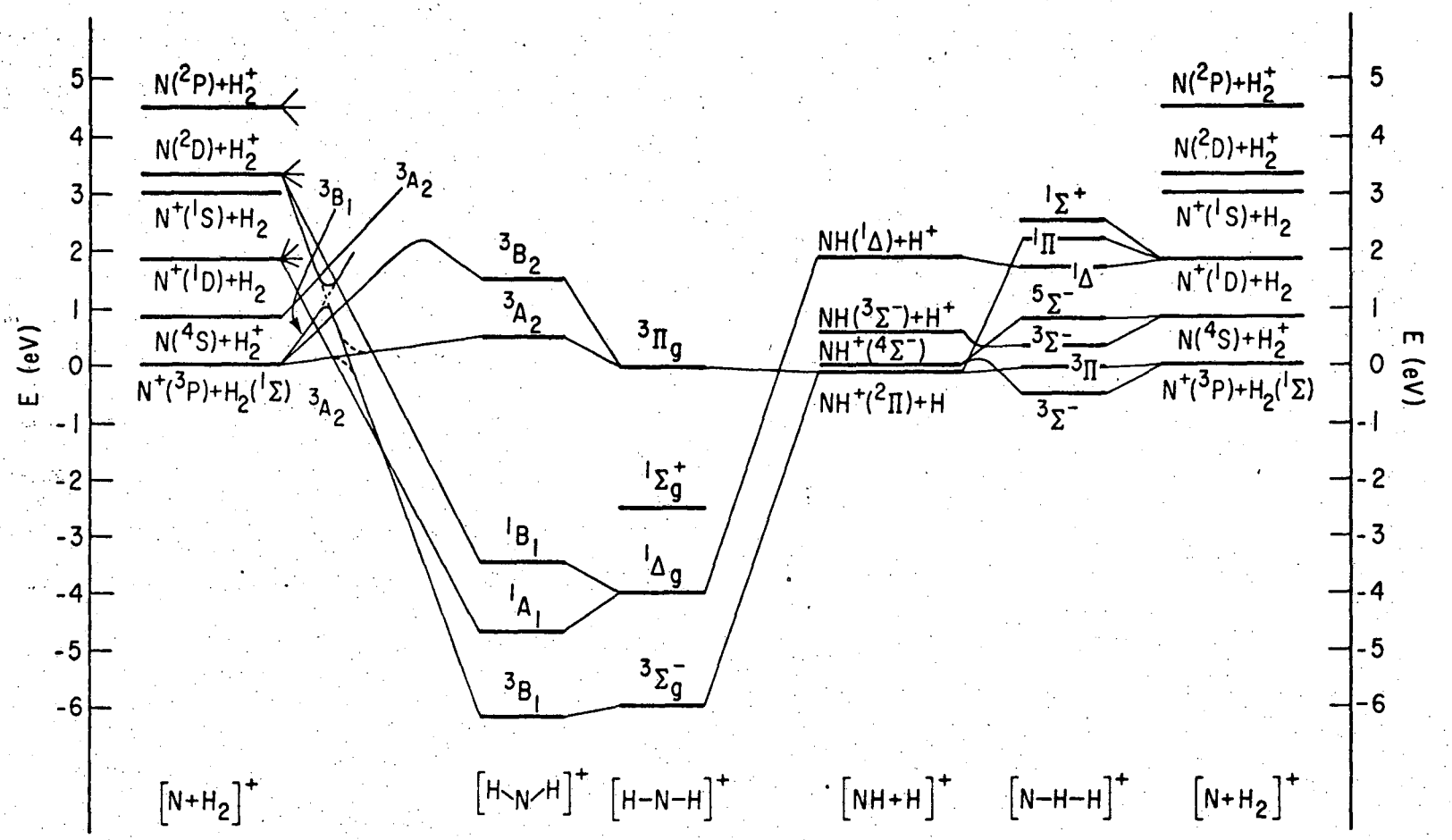


XBL 764-1593

Figure III-1. Correlation diagram for $(NH_2)^+$.

geometry. Immediately to the right of them are shown the $(HN+H)^+$ states, representing the products in $C_{\infty v}$ geometry. The correlations drawn between the columns represent slices through the potential surface parallel to one coordinate, the others being held constant. Moving from the left, the pertinent coordinates are: (1) The distance from the N atom to the $H_2$ bond midpoint; (2) The HNH bond angle; and (3) one of the NH bonds, the other remaining fixed.

On the right-hand side of the diagram, the assumed collision geometry requires the N atom to approach along the $H_2$ internuclear axis. The point group of this symmetry is $C_{\infty v}$, and the reactant states are resolved into the irreproducible representations of that group. The correlation proceeds through the $NHH^+$ intermediates to the $(NH+H)^+$ products.

More probable than either the exactly perpendicular or the exactly collinear approaches, of course, is the intermediate case. In this instance, the only symmetry element is the plane defined by the three atoms, and the point group is $C_s$. The reduced number of symmetry elements causes surfaces, previously of different symmetries, to become of the same symmetry. As a result, some crossings become avoided. The most important of these is the crossing between the $^3A_2$ and $^3B_1$ surfaces, shown as avoided in the dotted lines in the figure.

The energy levels of $H^+$, $N^+$ and $H_2^+$, and of the ground states of $NH^+$ and $NH_2^+$ shown in the figure are based on

spectroscopic determinations as tabulated by Moore.[8] The relative positions of the excited states of $NH^+$ are the results of ab initio calculations by Liu and Verhagen.[9] The excited states of $NH_2^+$, in the bent and linear configurations, were determined using theoretical calculations by Chu, Sui, and Hayes,[10] by Walsh,[11] and by Gimarc.[12] The resulting diagram should thus have quantitative as well as qualitative significance.

Examination of the diagram shows two principal paths from reactants to products. One is an essentially flat surface connecting ground state reactants, the $^3A_2$ and $^3\Pi_g$ states of $NH_2^+$, and the $^2\Pi$ state of the product $NH^+$. It is accessible from both the collinear and perpendicular approaches, as well as in the intermediate $C_s$ geometry. The other surface connects ground state reactants to the $^4\Sigma^-$ state of the products, and to the deep well occupied by the $^3B_1$ ground state of $NH_2^+$. This surface is freely accessible by collinear approach, but there is a significant barrier to perpendicular approach. In the $C_s$ geometry, the avoided surface crossing allows access to the well.

Avoided crossings are particularly interesting features because of the phenomenon of surface-hopping. The reaction is rigorously restricted to a single surface only when the motion of the atoms is infinitely slow. Otherwise, there is a finite probability of the reaction crossing from one surface to another, particularly when they are close together. The Landau-Zener expression has been used to estimate this

probability, and is given by:[13-15]

$$P = \exp(-\omega)$$

$$\omega = \frac{2\Pi}{h\underline{v}} \frac{H_{12}^2}{|H_{11}-H_{22}|} \qquad (1)$$

Here P is the probability of surface-hopping, $\underline{v}$ is the radial velocity at the crossing point, and the $H_{ij}$ are elements of the perturbation Hamiltonian. $H_{12}$ is the coupling between surfaces, and is hence one-half of the separation between them at their closest point; $H_{11} - H_{22}$ may be shown to be the difference in slopes between the two surfaces near the crossing. Equation 1 is rarely applied quantitatively to ion-molecule reactions, chiefly because of the difficulty in ascertaining the radial velocity $\underline{v}$. However, qualitatively it alerts us to the possibility of velocity-dependent surface-hopping behavior when surfaces approach closely, and describes the characteristics of the surfaces favorable to such behavior. In addition to the crossing mentioned in the previous paragraph, there is another close approach in the area between the NH--H and NHH configurations, where two $^3\Sigma^-$ surfaces converge.

Recent theoretical calculations have confirmed significant features of Figure III-1. Gittins and Hirst used unrestricted Hartree-Fock calculations to examine the $^3B_2$, $^3B_1$ and $^3A_2$ states of bent HNH and the $^3\Sigma^-$ state of linear NHH.[16] In the HNH case, they investigated the energy as a function of the bond angle and of the distance from the $N^+$

ion to the $H_2$ bond midpoint (N-$H_2$ distance). These are the portions of the surfaces represented by the second and first correlations from the left, respectively, in Figure III-1. The results were essentially as predicted. The dependence on bond angle of the $^3A_2$ and $^3B_1$ surfaces, small in any case, may be of the opposite sign. There may also be a slight well in the $^3A_2$ surface between reactants and bent HNH. In the linear case, the $^3\Sigma^-$ state energy was examined as the N-H and H-H distances were varied: these are the rightmost two correlations of Figure III-1. The results here were exactly as predicted, with a well-depth of about 1.07 eV between reactants and products.

Schaefer and co-workers have applied configuration-interaction calculations to a full two-dimensional study of the $^3A_2$ and $^3B_1$ states of $HNH^+$.[17] The N-$H_2$ distance varied from 1.25 to 3.00 bohr, and the $H_2$ internuclear distance (H-H distance) ranged from 1.2 to 2.6 bohr. Their results, like those of Gittins and Hirst, show a shallow depression in the $^3A_2$ surface, with a minimum of some 2 eV at H-H = 1.8 bohr, N-$H_2$ = 2.1 bohr. The $^3B_1$ surface is essentially identical to that of Figure III-1 when examined at the equilibrium H-H distance. However, the energy of this surface is significantly lower at greater H-H separations, approaching -4 eV (relative to reactants) when H-H = 2.6 bohr, N-$H_2$ = 1.25 bohr. Perhaps the most interesting question about these two surfaces is the shape of the avoided crossing which develops in $C_s$ symmetry. This problem, which

requires three dimensions for its description, was not addressed by Schaefer et al.

## B. Relation to Previous Studies

So far we have dealt with specifics: facts and concepts required to present the experimental results and conclusions. At this point, we shall become more general, and seek to place our work in context as part of a continuing research effort. The ion-molecule reactions:

$$A^+ + H_2 \rightarrow AH^+ + H \qquad (2)$$

where A represents a second- or third-row atom and $H_2$ includes the isotopic variants HD and $D_2$, are a fruitful domain for a brief survey. These reactions are complex enough to show chemically interesting behavior, yet sufficiently simple not to baffle our intuition. They are also near the limit of complexity which can be dealt with a priori by theoreticians with any reliability. For this reason, they have excited appreciable experimental interest. We shall restrict ourselves to a review of those works which, like the present one, produce angular and energy distributions of the reaction products.

Workers in this laboratory have investigated reaction (2) with A representing C, O, Ne, Ar, and N.[2-5, 18-20] In addition, Koski and co-workers have studied the C and F systems;[21,22] Doverspike et al. have examined the C and Ar reactions;[23,24] Wolfgang and co-workers have investigated

the Ar example;[25,26] and Henglein and associates have looked at some aspects of the N case.[27] These efforts have led to some tentative classifications of the resulting scattering distributions. We shall refer to three general types of behavior, each representative of a different energy range, which we shall call complex, stripping, and trans-stripping behavior.

At the outset, we should stress the oversimplifications inherent in such a classification. The most prominent qualitative characteristics of the scattering are abstracted, at the price of ignoring finer structure which may be both marked and significant. Nevertheless, understanding begins with classification, and the scheme is useful and informative if applied with caution. We shall endeavor to point out the limitations relevant to each category as we examine them in turn.

Complex behavior is represented by scattering distributions which have the forward-backward symmetry of the complex model discussed in Chapter I. This behavior implies a complex with the characteristic lifetime $\tau_c$ long with respect to a rotational period $\tau_r$. This in turn requires a well in the potential surface of depth -V which is large with respect to the energy $E_{rel}$ of the collision. Obviously this condition will fail at some point as $E_{rel}$ increases; complex behavior, if observed, is thus restricted to the lowest energy regime. In practice, there is usually a smooth progression from nearly complete symmetry at low energies to the strongly

asymmetric distributions characteristic of impulsive models, and we shall thus generalize the term complex behavior to describe distributions with "substantial" forward-backward symmetry. This is equivalent to restating the lifetime and energy conditions so that $\tau_c \gtrsim \tau_r$; $-V \gtrsim E_{rel}$.

Complex behavior has been reported for the C and F cases of reaction (2).[4,22] In neither case is the symmetry complete at the lowest energy studied. In the $C^+$ system only a slight asymmetry is seen at a collision energy of 2.86 eV; a well-depth of 4.3 eV is expected on the basis of correlation arguments. It is interesting, however, the Doverspike et al. have extended the energy range studied down to 0.64 eV and noted no further increase in symmetry.[23] In the $F^+$ system, almost complete symmetry is reported at 0.21 eV. Correlation diagrams indicate a $FH_2^+$ state with an energy of -9 eV relative to reactants, but suggest that this state is not accessible to the reactants.[22] Further study appears warranted on this problem.

At intermediate energies, all scattering distributions observed so far resemble the predictions of the spectator stripping model to a considerable extent. It seems reasonable to characterize such patterns as stripping behavior. This designation in particular must be applied with caution. Kuntz, Mok, and Polanyi defined stripping as a process producing predominantly forward scattered products;[29] we concur with Winn that this definition is overbroad to the point of being uninformative.[28] We shall apply the term to direct or

short-lived (relative to $\tau_r$) interactions in which there is little transfer of momentum to one of the reactant atoms in a substantial fraction of cases. In scattering distributions, this corresponds to the existence of a substantial peak at the location predicted by the spectator stripping model.

Mahan has emphasized the oversimplification inherent in the spectator stripping model, observing: "Without question, the idea that atom B can be transferred to A with no force being exerted on C is quite remarkable."[30] We should certainly not allow the fascination of our classification scheme to beguile us into neglecting scattering away from the stripping peak, which is frequently substantial. We should also remember that the prominence of the stripping peak is to some extent an artifact, based on the collection of product only in the detector plane. This weights the observed distribution by a factor of $(\sin\theta)^{-1}$, giving exceptional prominence to small angle scattering. Despite all these caveats, however, stripping behavior remains the predominant feature of scattering distributions at intermediate energies.

The two systems displaying low-energy complex behavior exhibit a gradual shifting of the peak intensity towards higher velocities as energy increases. In the $F^+$ system, the peak has moved close to the stripping position at 0.39 eV. Increasing energy improves the approximation, until the coincidence is essentially complete at the dissociation limit for stripping product, 0.81 eV.[22] In the $C^+$ system, the

transition is slower and never complete: at the dissociation limit the peak still lies at a slightly lower velocity than predicted by the spectator stripping model.[4]

In the $Ar^+$ and $O^+$ systems, which do not display complex behavior, the stripping model is a very good approximation at all energies studied up to the dissociation limit.[3,19] In the Ar case, there is also a marked peak behind the center of mass, emphasizing the limits of the stripping model.

Behavior at energies above the stability limit for spectator stripping will be classified as trans-stripping behavior. It was originally expected that, at this point, the forward intensity peak would disappear.[31] In the $Ar^+$ system, however, an intense peak remains at $\chi = 0°$ and near the dissociation limit in energy, even though the stripping prediction lies in the unstable zone.[19] Angular distributions for the $F^+$ system were not reported in this zone, but the energy of the forward peak shows similar behavior.[22] In the $C^+$ system, the peak continues to coincide with the stripping prediction, indicating the formation of excited electronic states.[4]

Dramatically different behavior was observed in the $O^+$ system.[18] Above the instability limit, the peak intensity moves off the centerline to larger CM angles, remaining near the instability limit in energy. The position of these maxima is isotope-dependent and nearly independent of energy within the trans-stripping regime. This difference has been attributed to the fact that the $Ar^+$ and $F^+$ reactions are

considerably exothermic, while the $O^+$ system is essentially thermoneutral. The exothermicity of the former reactions may be expended as repulsion between the products, thus stabilizing the impulsive stripping mechanism. In the $O^+$ system, this method is not available, and alternate mechanisms must come into play. For this reason, the behavior of the nearly thermoneutral $N^+$ reaction in the trans-stripping regime was of particular interest to us.

The scattering of nitrogen ion from $H_2$ was among the first systems studied with our apparatus. The energies investigated ranged from 2.5 to 8.1 eV, and spanned the stripping region. The intensity observed was concentrated in a forward peak at the spectator stripping location and a smaller, backward, peak near the ideal knockout velocity.[20] Subsequently, Fair and Mahan reacted $N^+$ with $H_2$, $D_2$, and HD at lower energies and in a different apparatus. In this lowest energy regime, complex behavior was observed, with symmetry nearly complete at 0.79 eV. The transition to the stripping regime is complete above about 2.79 eV. They explained this behavior as due to the avoided crossing between the $^3A_2$ and $^3B_1$ surfaces, discussed in the first section of this chapter. At low relative energies, reaction occurs adiabatically on the lower surface and is dominated by the deep $NH_2^+$ well; at higher energies, transition to the upper surface at the crossing becomes predominant, essentially closing off the well and producing $NH_2^+(^3A_2)$.

Other studies of the $N^+ + H_2$ reaction have concentrated mainly on total cross-sections. Fehsenfeld et al. measured

a thermal cross-section of $5.6 \times 10^{-10}$ $cm^3$ $sec^{-1}$ in 1967.[32] Recently, Henglein and co-workers studied the energy distribution of $NH^+$ and $ND^+$ from HD target over the stripping range. Their results were essentially those of Tsao, Mahan, et al.[26] They also observed the total cross-section as a function of energy in the range from 1-5 eV. The current study extends our knowledge of the system into the transstripping regime, and serves to test the tentative generalizations summarized in this section.

## References


1. B. H. Mahan, J. Chem. Phys. 55, 1436 (1971).

2. B. H. Mahan and J. S. Winn, J. Chem. Phys. 57, 4321 (1972).

3. Keith T. Gillen, Bruce H. Mahan and John S. Winn, J. Chem. Phys. 58, 5373 (1973).

4. Bruce H. Mahan and Thompsom M. Sloane, J. Chem. Phys. 59, 5661 (1973).

5. James A. Fair and Bruce H. Mahan, J. Chem. Phys. 62(6), 515 (1975).

6. For an extensive discussion of the method, see Gerhard Herzberg, Molecular Spectra and Molecular Structure, Vol. III, Van Nostrand Reinhold Co., New York (1966), p. 312 ff.

7. Gerhard Herzberg, op. cit., p. 442 ff.

8. Charlotte Moore, Atomic Energy Levels, Nat. Bur. Stds. (U.S.) Circular 467 (1948).

9. H. P. D. Liu and G. Verhaegen, J. Chem. Phys. 53, 735 (1970).

10. S. Y. Chu, A. K. Q. Siu, and E. F. Hayes, J. Am. Chem. Soc. 94, 2969 (1972).

11. A. Walsh, J. Chem. Soc. 2260 (1953).

12. B. Gimarc, J. Am. Chem. Soc. 93, 593 (1971).

13. C. Zener, Proc. Royal Soc. (London) A137, 696 (1932).

14. L. Landau, Z. Phyz. Sowjet, 2, 46 (1932).

15. E. C. G. Stueckelberg, Helv. Phys. Acta, 5, 369 (1932).

16. Martin A. Gittens and David M. Hirst, Chem. Phys. Lett. 35, 534 (1975).

17. Henry F. Schaefer, et al., to be published.

18. Keith T. Gillen, Bruce H. Mahan and John S. Winn, J. Chem. Phys. 59, 6380 (1973).

19. M. Chiang, E. A. Gislason, B. H. Mahan, C. W. Tsao and A. S. Werner, J. Chem. Phys. 52, 2698 (1970).

20. Eric A. Gislason, Bruce H. Mahan, Chi-Wing Tsao and Arthur S. Werner, J. Chem. Phys. 54, 3897 (1971).

21. C. R. Iden, R. Liardon and W. S. Koski, J. Chem. Phys. 56, 851 (1972) and J. Chem. Phys. 54, 2757 (1971).

22. F. K. Wendell, C. A. Jones, Joyce J. Kaufman, and W. S. Koski, J. Chem. Phys. 63(2), 750 (1975).

23. E. C. Herbst, R. L. Champion and L. D. Doverspike, J. Chem. Phys. 63, 3677 (1975).

24. L. D. Doverspike, R. L. Champion, and T. L. Bailey, J. Chem. Phys. 45, 4385 (1966).

25. P. M. Hurl, Z. Herman and R. Wolfgang, J. Chem. Phys. 53, 660 (1970).

26. Z. Herman, J. Kerstetter, T. L. Rose, and R. Wolfgang, Disc. Faraday Soc. 44, 123 (1967).

27. G. Eisele, A. Henglein, P. Botschwina, and W. Meyer, Birichte der Bunsen-Gesellschaft, 78, 1090 (1974).

28. John S. Winn, Ph.D. Thesis, University of California LBL Report 1820 (1973), p. 176.

29. P. J. Kuntz, M. H. Mok and J. C. Polanyi, J. Chem. Phys. 50, 4623 (1969).

30. Bruce H. Mahan, in Interactions Between Ions and Molecules, P. Ausloos, editor, Plenum, New York (1975).

31. Bruce H. Mahan, in International Review of Science II, Vol. 9, Butterworth's (1976).

32. F. C. Fehsenfeld, A. L. Schmeltekopf, and E. E. Ferguson, J. Chem. Phys. 46, 2802 (1967).

# CHAPTER IV

# RESULTS

## A. Scope and Presentation

The principal experimental results to be presented in this work are a series of fifteen experiments, each comprising a determination of the product intensity from a given reaction at a given beam energy. These experiments each include an examination of the entire accessible range of product energy and scattering angle. Using these determinations as a guide, an additional thirty-one experiments were performed covering a more restricted portion of the theoretically available product range.

The order in which these results will be presented follows almost irresistibly from the characteristics of the experiments themselves. A fundamental separation is into reactive and non-reactive processes. Within the reactive category, the results are further subdivided according to the reactions studied. They are:

$$N^+ + H_2 \rightarrow NH^+ + H \qquad (1)$$

$$N^+ + HD \rightarrow NH^+ + D \qquad (2)$$

$$N^+ + HD \rightarrow ND^+ + H. \qquad (3)$$

The logical fourth member of this sequence is the reaction:

$$N^+ + D_2 \rightarrow ND^+ + D. \qquad (4)$$

An effort was made to study this reaction, but observable product intensities were not found. This was hardly surprising, since the signal from reaction (4) may cover a laboratory velocity space about eight times the volume of reaction (1) and since the product intensities from the first three reactions were near the resolution limit of the apparatus.

In the category of non-reactive experiments, we dealt principally with the two processes:

$$N^+ + H_2 \rightarrow N^+ + H_2 \qquad (5)$$

and

$$N^+ + D_2 \rightarrow N^+ + D_2. \qquad (6)$$

For kinematic reasons, experiments at lower relative energies were performed with $H_2$ target, while those at higher energies used $D_2$ as the scattering gas. Despite some overlap, the pair of reactions basically comprise a single study, and will be presented together. Experiments involving the process:

$$N^+ + He \rightarrow N^+ + He \qquad (7)$$

were performed chiefly for comparison with the results of reaction (6), and will be presented in that context. As a final contribution to the non-reactive section, we will present observations bearing on the charge exchange reaction:

$$N^+ + H_2 \rightarrow N + H_2^+ \qquad (8)$$

## B. Reactive Scattering

Our examination of reaction (1) commences with Figure IV-1, which represents the intensity of $NH^+$ product at an initial relative velocity of 6.87 eV. The figure is a plot of product intensity contours in CM polar coordinates, which we shall refer to as a map. The large cross at the center of the map marks the location in velocity space of the center of mass. The small dot near the right-hand edge marks the CM velocity of the incident beam and is surrounded by a dotted line marking the beam spread. The product intensity contours are shown in terms of the quantity $\bar{I}$ of equation (II-1). Also shown are two circles, corresponding to lines of constant translational exoergicity ("Q-values"). They mark the loci of Q = 0.6 and Q = -4.6, the limits of product stability implied by equation (I-17).

As mentioned in Chapter II, our data processing program yields both symmetrized and unsymmetrized map plots. The maps presented here represent the symmetrized output. However, it is frequently also of interest to know the location of the maxima obtained on each cut. These maxima are marked by the small circles in the figures, and are based on the unsymmetrized values of the results.

The relative energy of Figure IV-1, 6.87 eV, lies in the range previously examined by Tsao et al.: this experiment thus serves as our point of departure from known to unknown territory. The predominant feature of the map is the

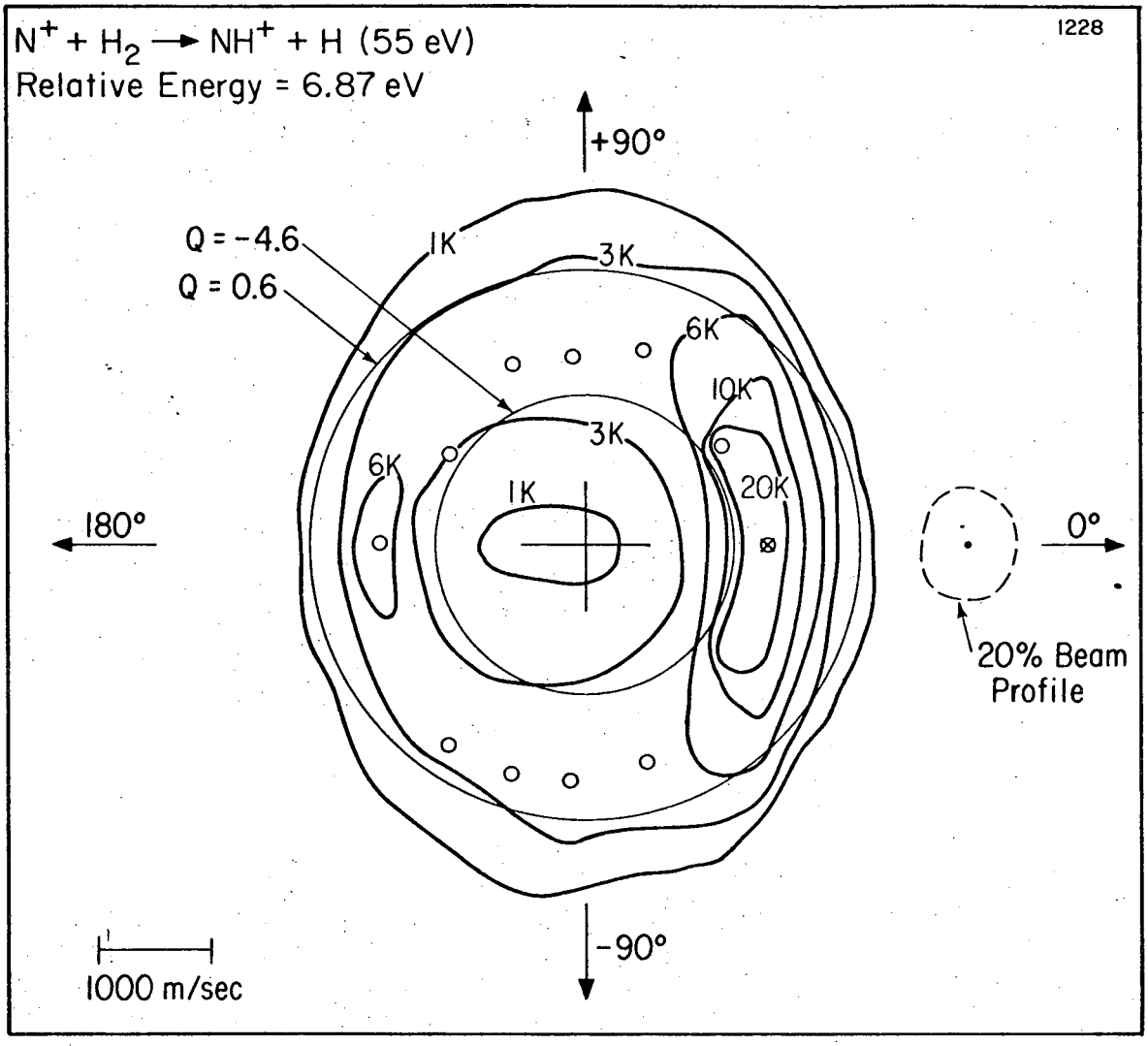


Figure IV-1

large peak forward of the center of mass, on the centerline, and at about the velocity predicted by the spectator stripping model. This predicted velocity is marked with a small "x". There is also a smaller peak behind the center of mass. These features characterized the entire stripping range in earlier work.[1]

Figure IV-2 shows the same reaction at an energy of 8.75 eV. The stripping peak is still evident, and a ridge of intensity still appears behind the centroid. The stripping peak has now moved to the inner edge of the stability limit, and the observed intensity has diminished considerably.

In Figure IV-3, the energy has been increased to 12.5 eV. Spectator stripping does not produce a stable product at this energy, and we observe that the peak at 0° is no longer in evidence. Instead, the maximum intensity appears in two symmetrical lobes at a CM angle of about 60°. The maxima of the cuts, marked by the small circles, fall near the inner limit of the stability zone.

Figure IV-4, taken at 15.6 eV, reveals an interesting development. The two lobes at about $\chi = \pm 60°$ are still in evidence, albeit weaker. However, there is also evidence of product again appearing on the centerline. All of the product intensities are extremely low, and lie at the very limit of the apparatus resolution. The rather unexpected central peak in Figure IV-1 motivated us to examine the identical reaction and energy using beams from alternate source gases. The results, using ammonia and nitrous oxide

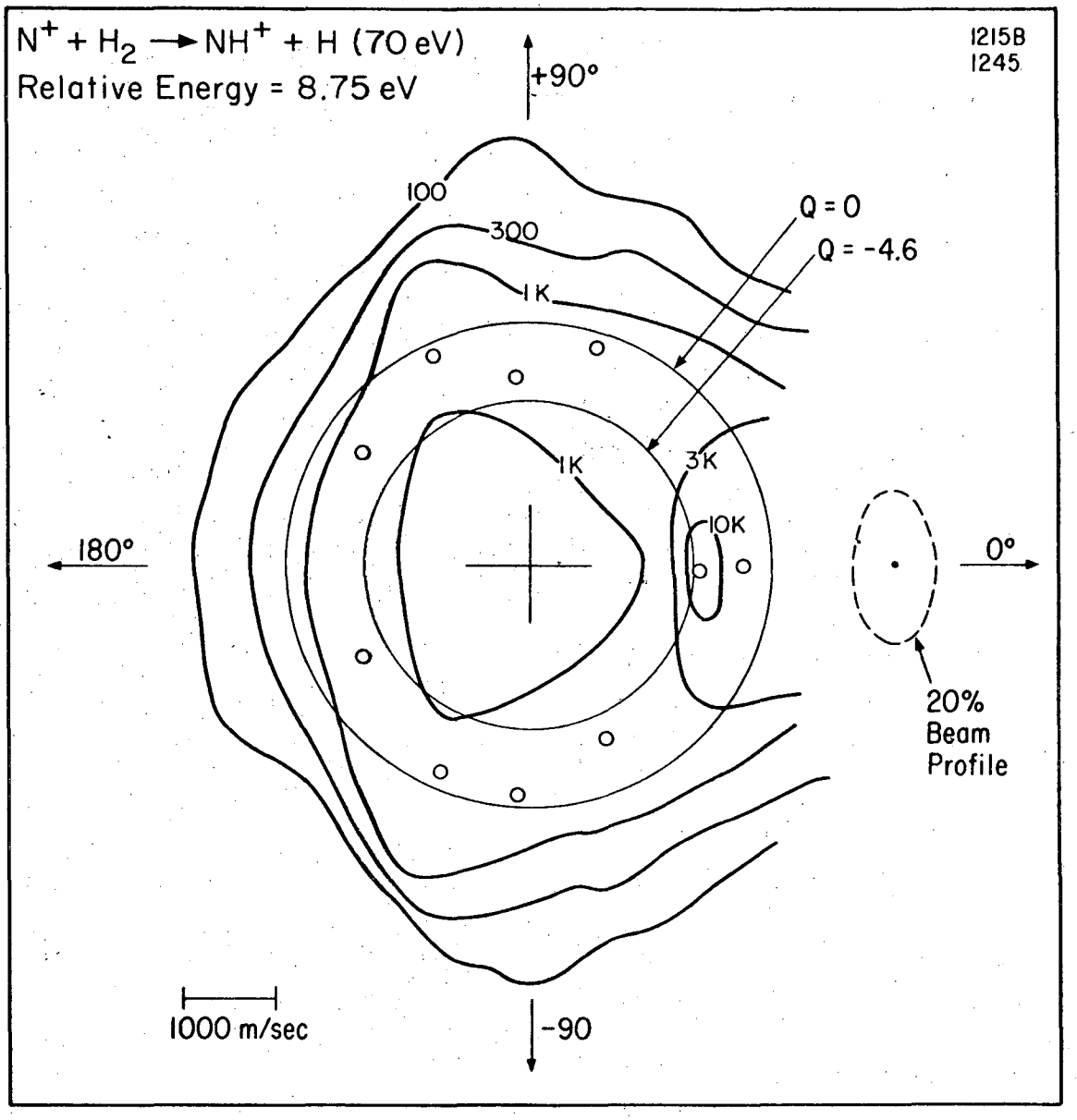


Figure IV-2

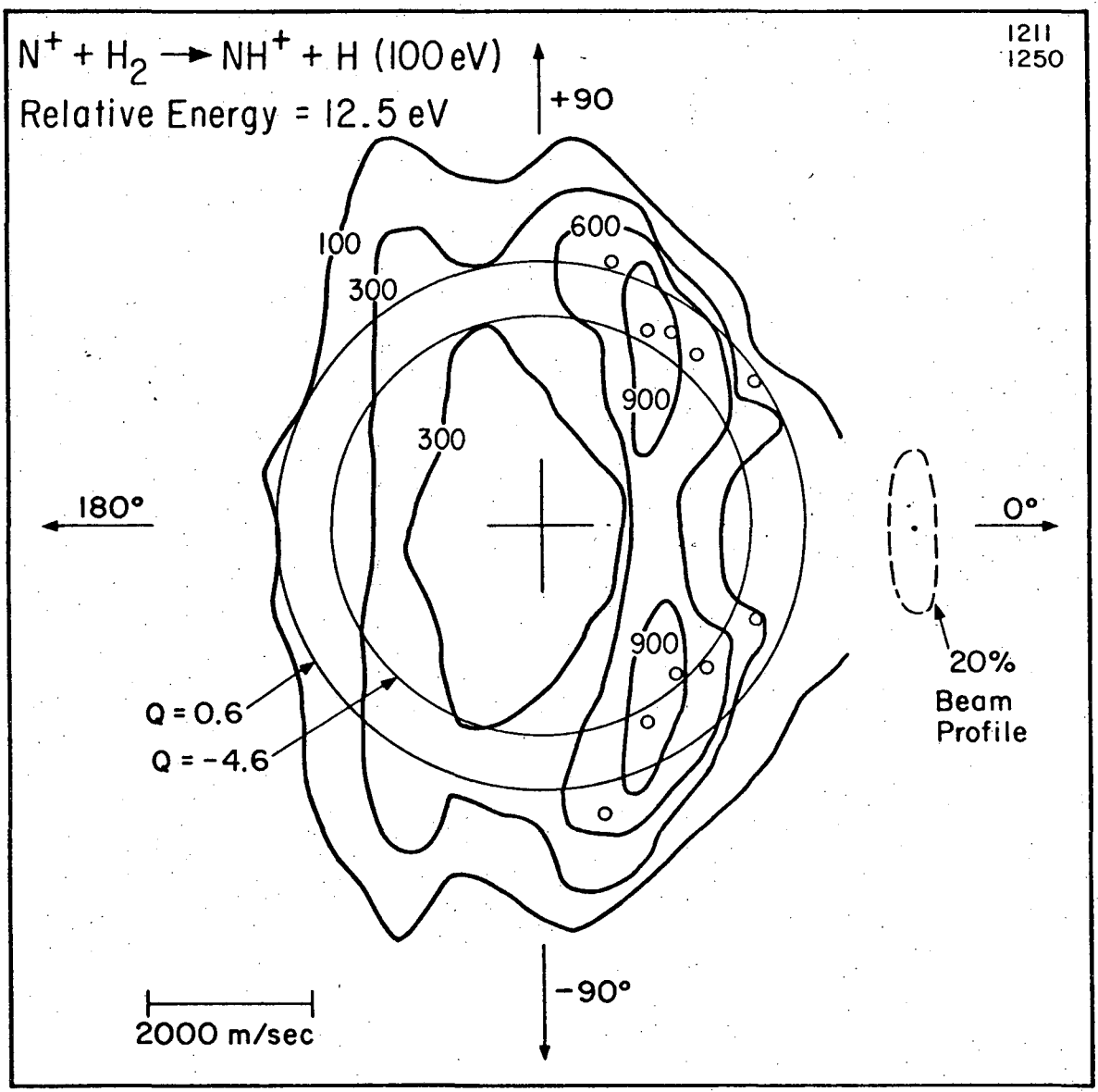


XBL 764-1588

Figure IV-3

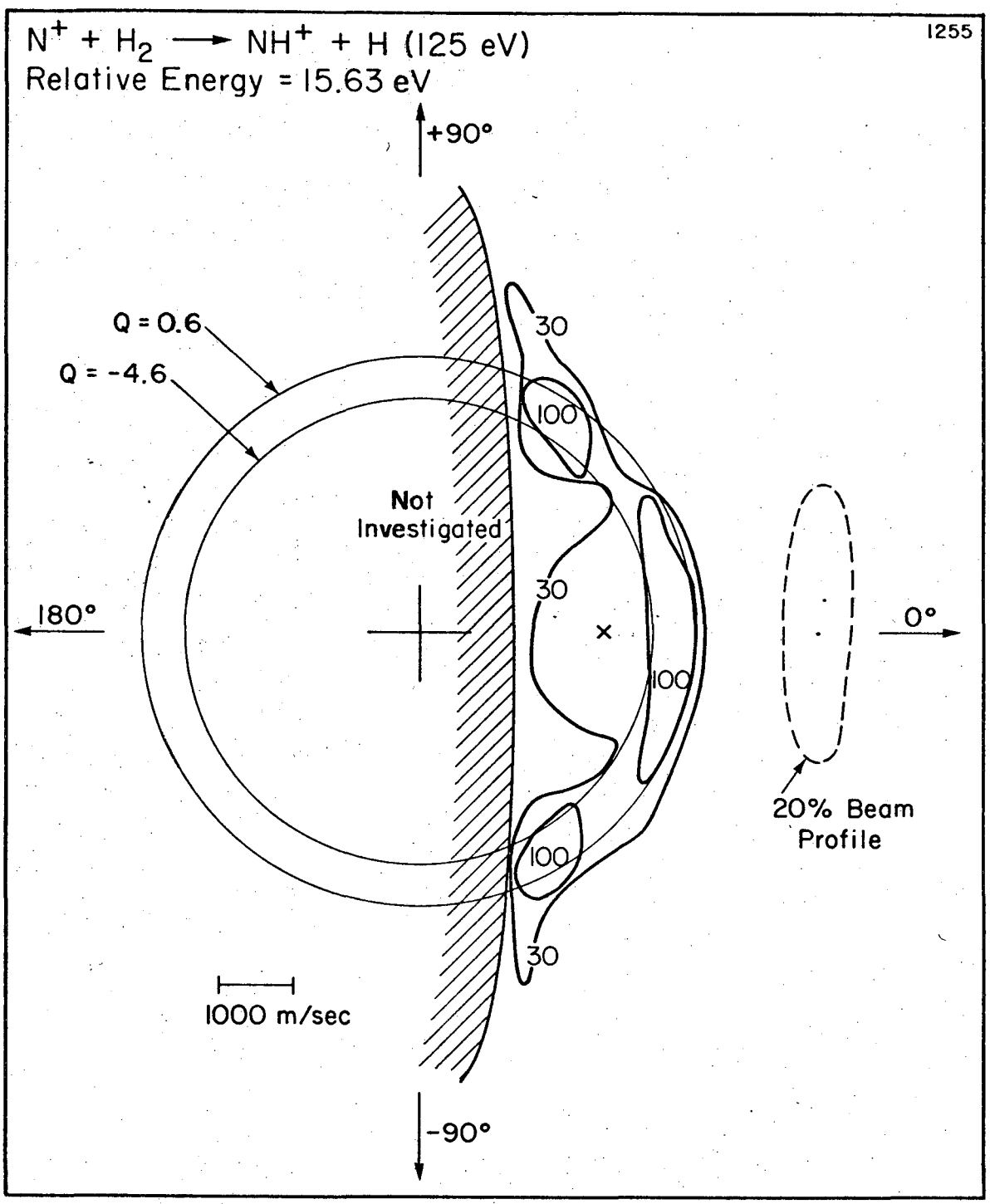


XBL 765-1769

Figure IV-4. $N^+$ from $N_2$/He discharge, as usual: <3% excited state concentration.

respectively as $N^+$ sources, are given as Figures IV-5 and IV-6. We notice an increased intensity of the central peak, relative to the side peaks, with the $NH_3$ source and an even greater increase when $N_2O$ is used.

With Figure IV-7, we commence our study of reaction (2). Shown are the reaction products from collision at a relative energy of 9.71 eV, approximately the same as that of Figure IV-2. The two figures resemble each other closely, Figure IV-8 shows the same reaction at 12.35 eV, a similar energy to that of Figure IV-3. Again, the two distributions are quite similar, with the emergence of two symmetric lobes. In this case, the CM angles of the lobes are near 30°. In Figure IV-9, the energy has been increased to 17.65 eV. The side lobes have completely disappeared, and a small residual peak on the centerline has appeared analogous to that seen in Figure IV-4 to IV-6. At 22.1 eV, in Figure IV-10, the same pattern appears with exceedingly low intensity.

Our lowest-energy examination of reaction (3) is depicted in Figure IV-11. At an energy of 6.54 eV, the spectator stripping velocity rests just on the edge of inner stability circle, and is marked by a small cross. We observed the presence of lobes in the forward hemisphere and a ridge about the centerline in the back scattered region. This map bears a qualitative resemblance to those previously presented for reactions (1) and (2).

At higher energies, however, this comforting similarity disappears. In Figure IV-12, at a relative energy of 9.71 eV,

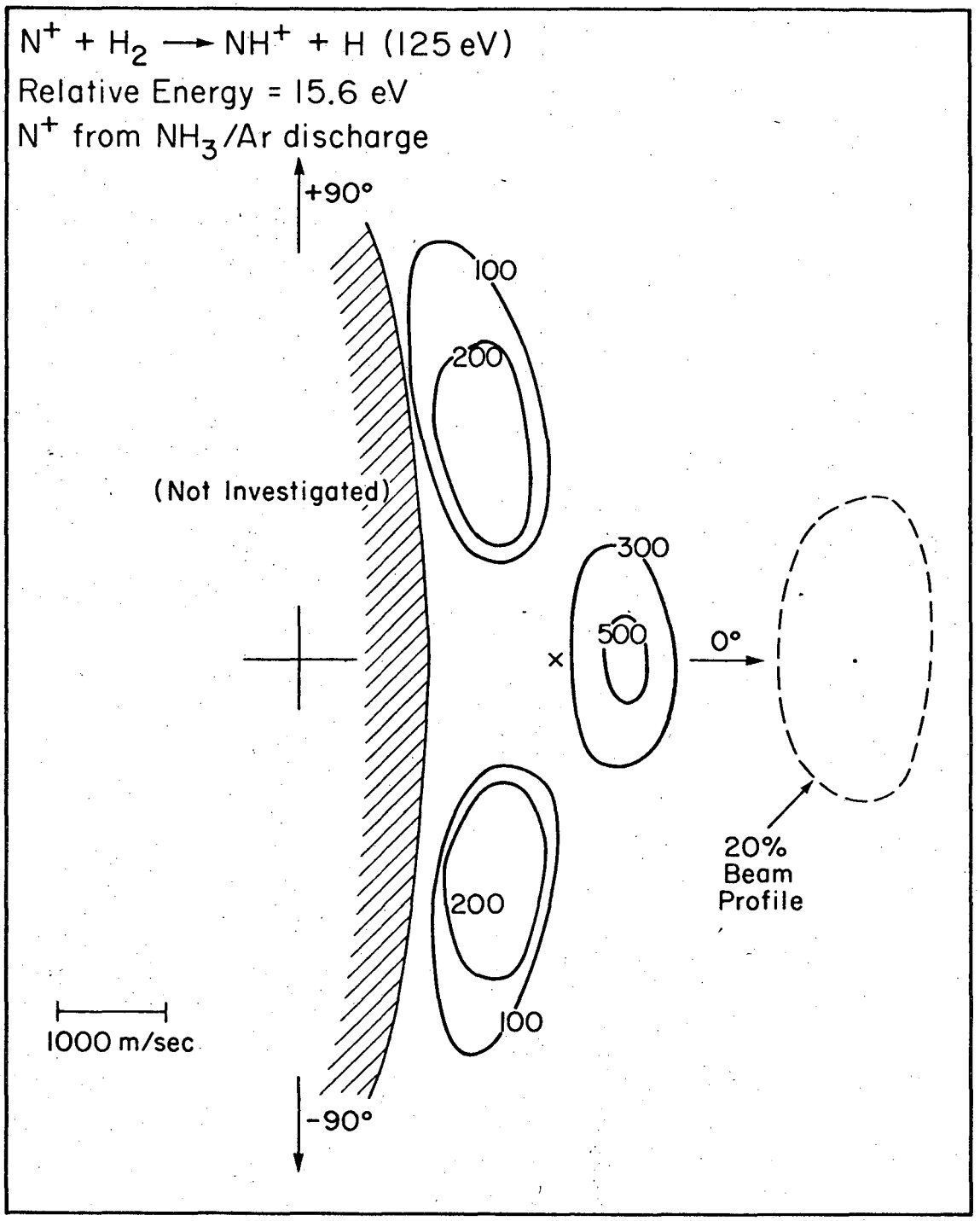


XBL 765-1770

Figure IV-5. $N^+$ from $NH_3$/Ar discharge: about 3% excited.

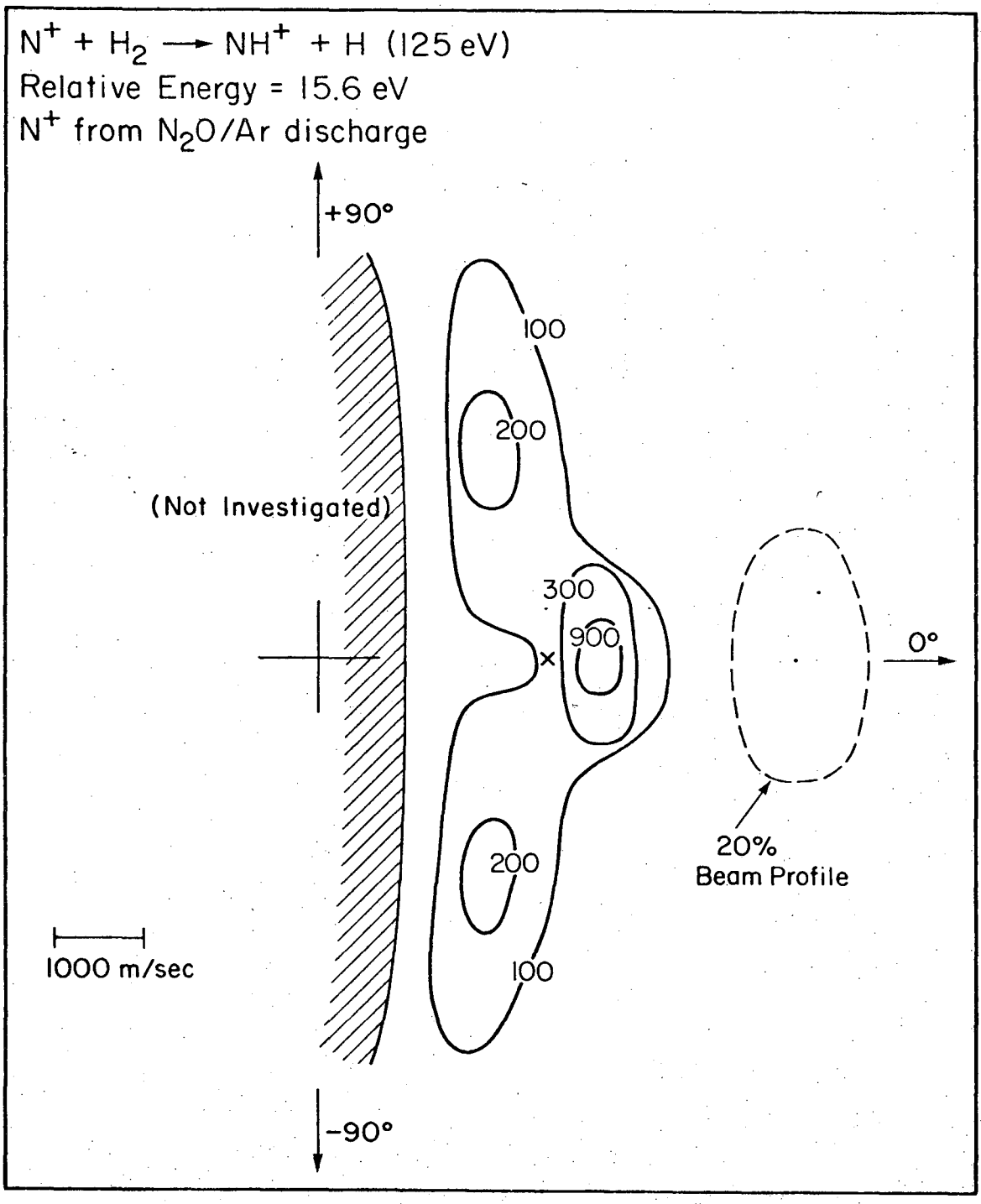


Figure IV-6. $N^+$ from $N_2O$/Ar discharge: about 6% excited.

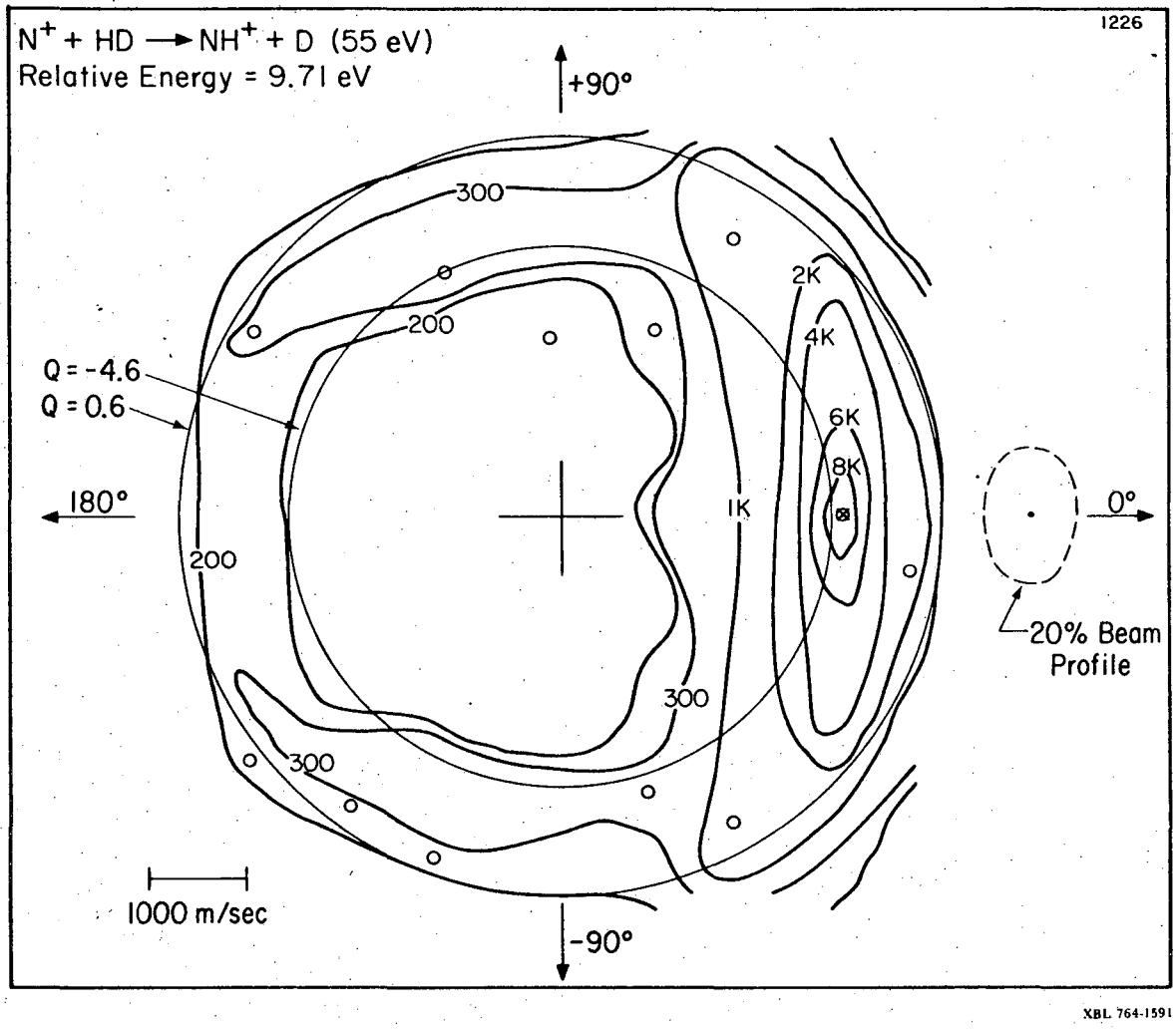


Figure IV-7

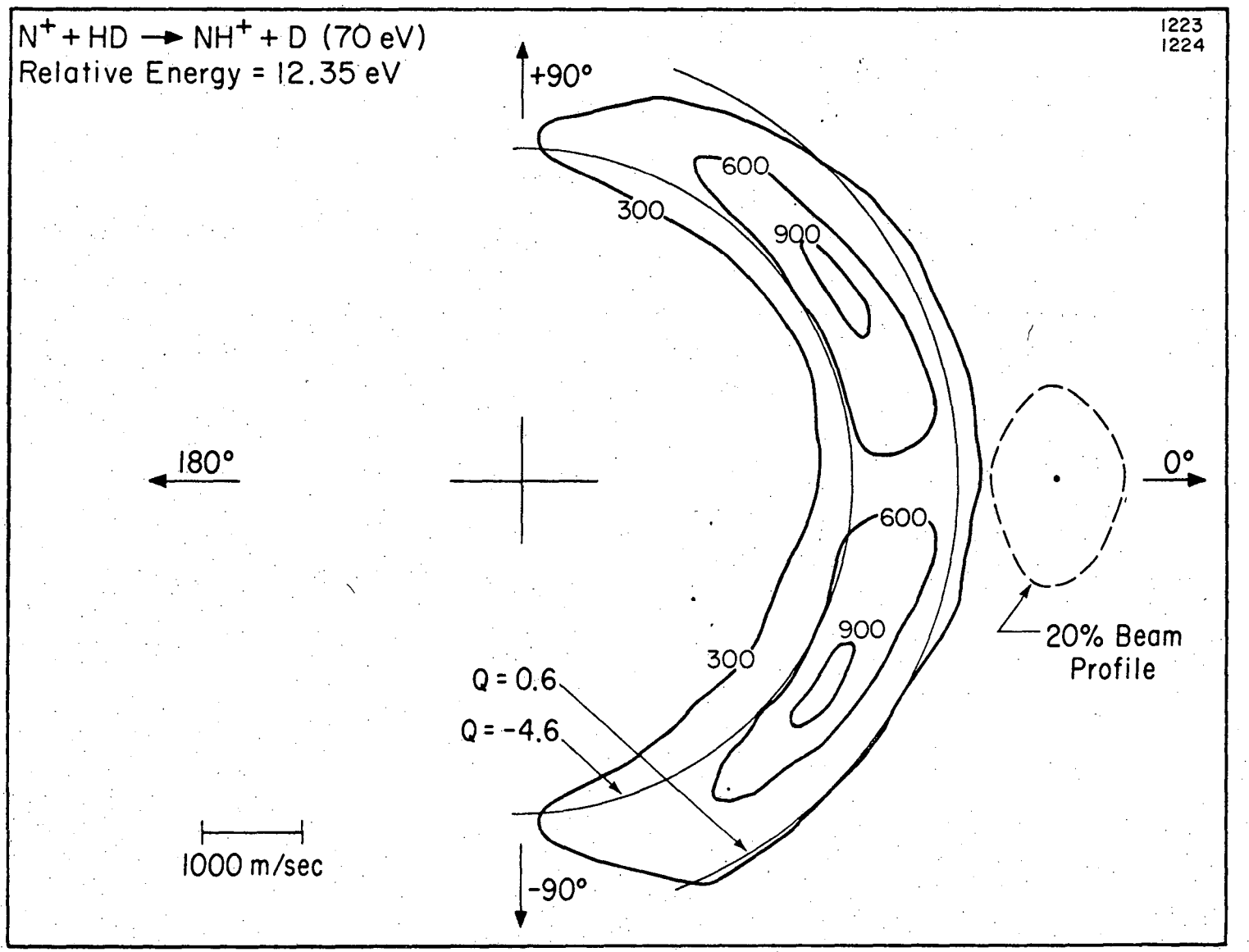


XBL 764-1592

Figure IV-8

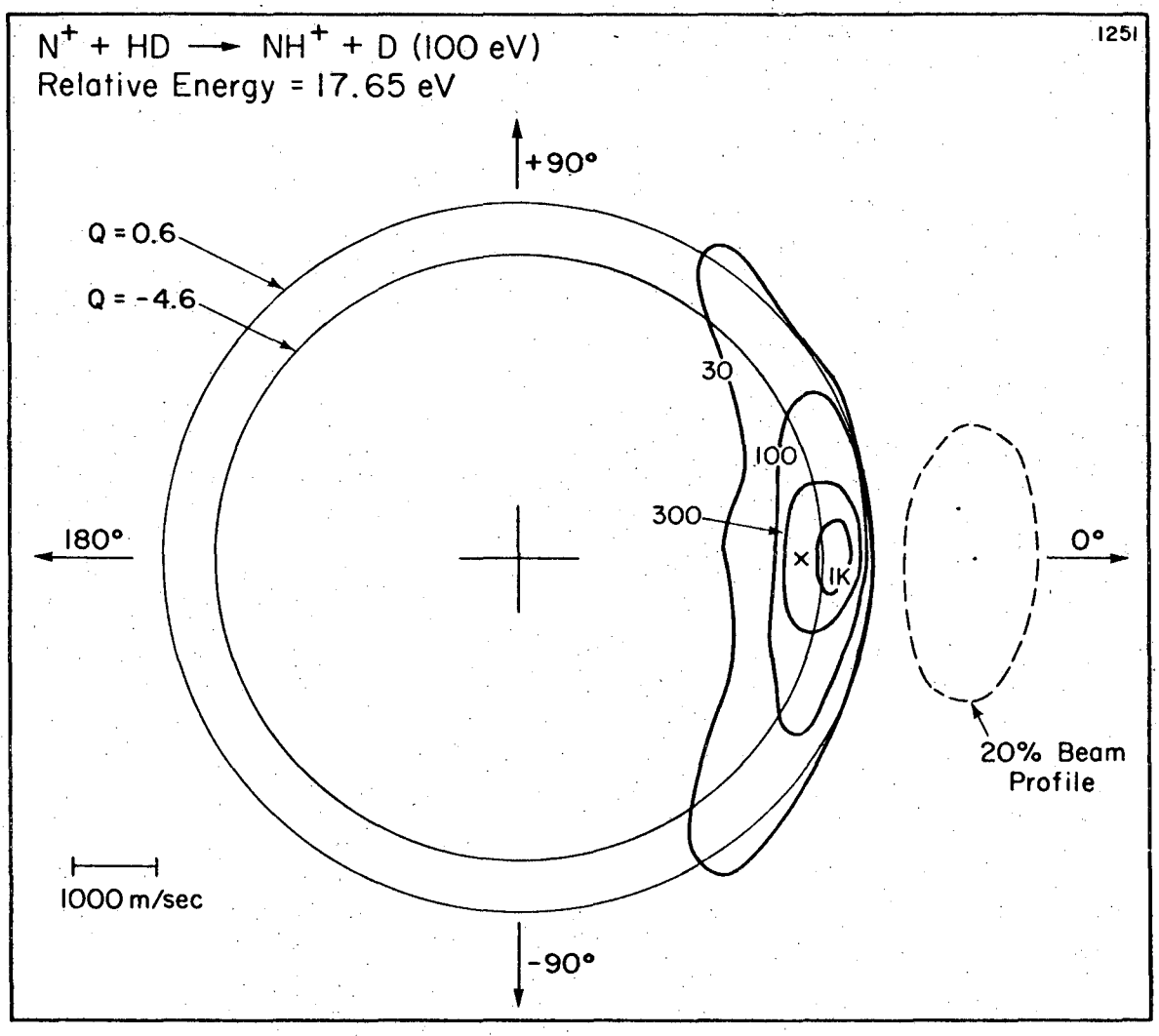


XBL 765-1764

Figure IV-9

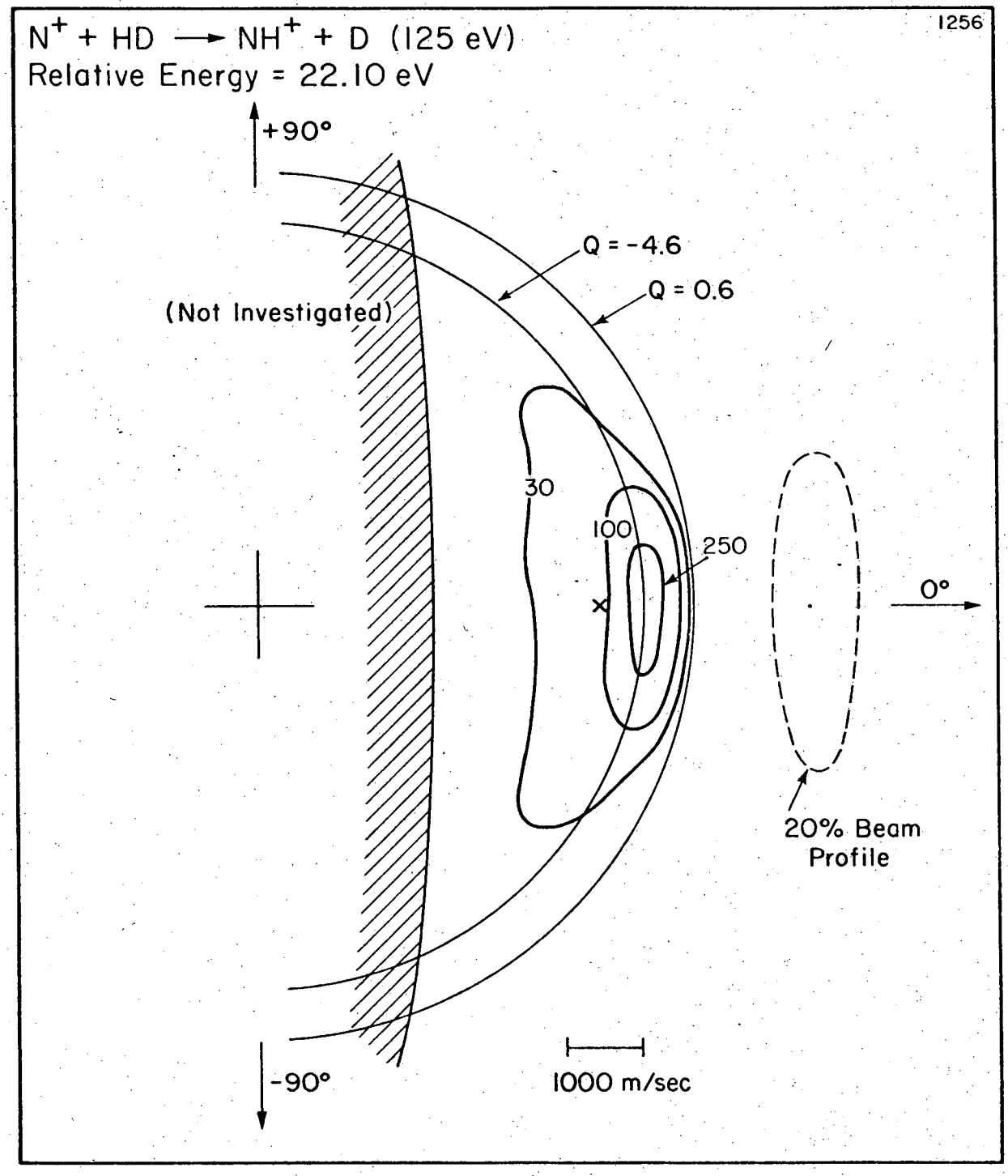


XBL 765-1768

Figure IV-10

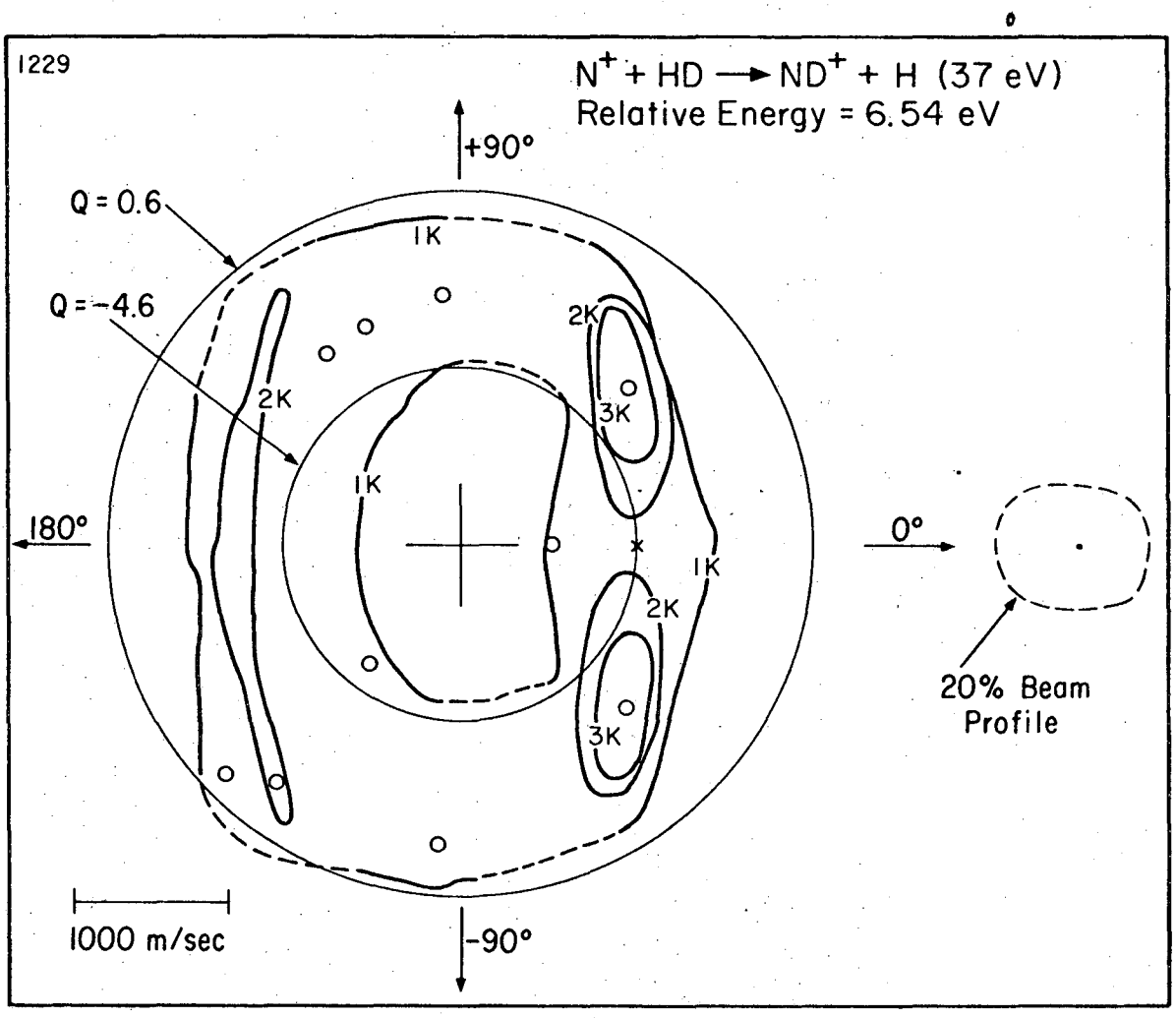
1229
$N^+ + HD \rightarrow ND^+ + H$ (37 eV)
Relative Energy = 6.54 eV
+90°
Q = 0.6
Q = −4.6
1K
2K
2K
3K
1K
180°
0°
1K
2K
3K
20% Beam Profile
1000 m/sec
-90°
XBL 764-1589

Figure IV-11

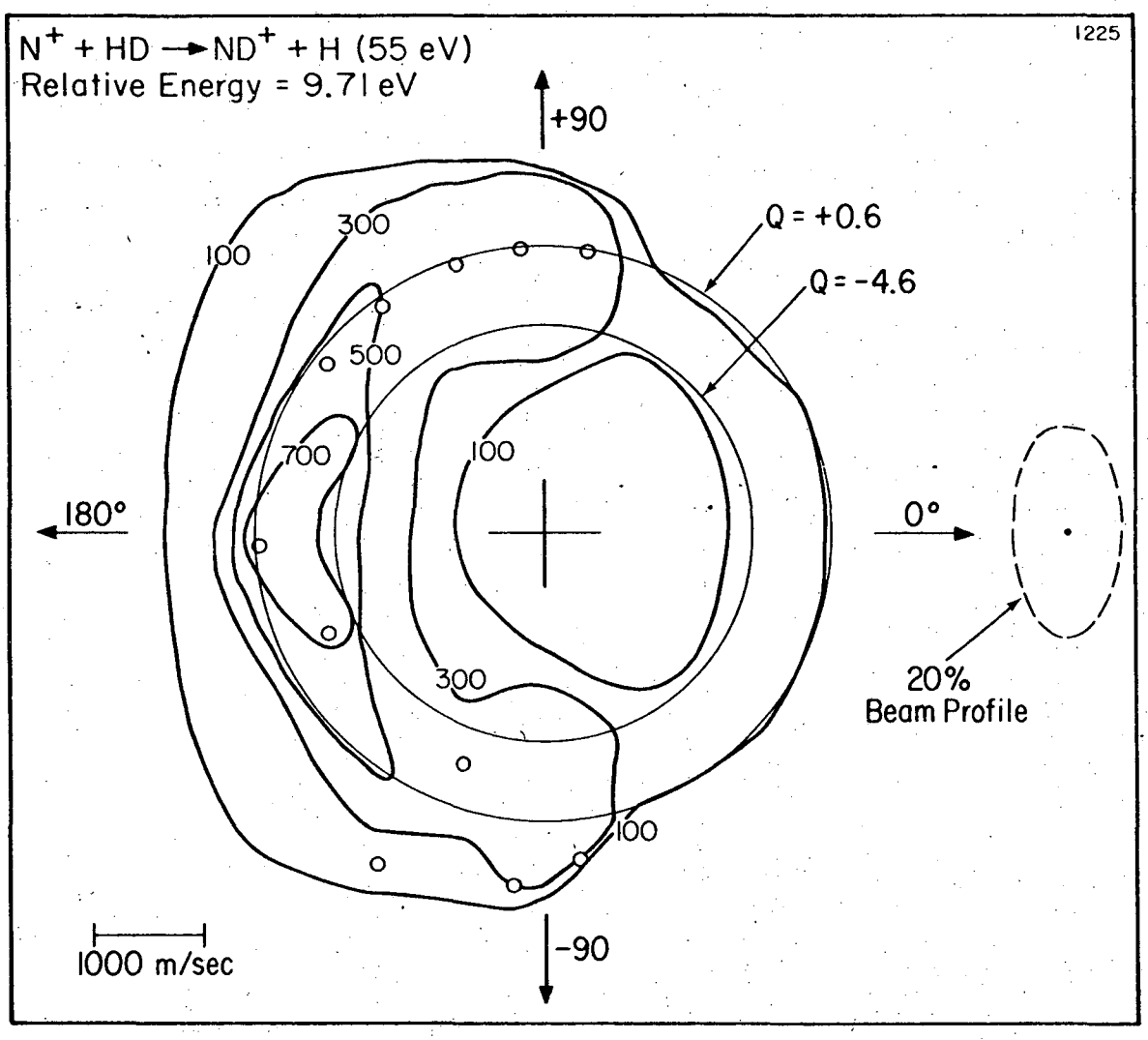
N+ + HD → ND+ + H (55 eV)
Relative Energy = 9.71 eV
1225
+90
Q = +0.6
Q = -4.6
300
100
500
700
100
180°
0°
300
20%
Beam Profile
100
1000 m/sec
-90
XBL 764-1586

Figure IV-12

the scattering is concentrated almost exclusively in the rear hemisphere, peaking on the centerline. Increasing the energy to 12.35 eV produces the results shown in Figure IV-13: the concentration in the 180° direction is even more marked.

In addition to the maps just described, additional experiments were undertaken to locate the intensity peaks at energies intermediate between those of the maps. All of these results are presented in graphical summary by Figures IV-14, IV-15, and IV-16. In Figure IV-14, the location of the peaks in energy is shown as a function of beam energy for reaction (1). Also shown are the predictions of the spectator stripping ideal rebound and the knockout models, the Q value of the centroid (equal to the relative collision energy), and the stability limits of various products. Figure IV-15 shows a simliar plot for reactions (2) and (3). In Figure IV-16, the angular dependence on energy of the principal peak is shown for all three reactions. On the abscissa is plotted, not the relative energy of the system, but the "impulsive relative energy," that is, the relative energy of the ion relative to the atom with which it reacts.

Figures IV-14 - IV-16 bear out the impressions given by the reactive maps, and allow us to summarize the behavior of reactions (1) - (3). Below the stability limit for spectator stripping, there is a large forward and a smaller back peak, both on the centerline; the energy of the forward peak is close to the spectator stripping prediction. Above the limit, the forward peak splits into two lobes located in the forward hemisphere. For reactions (1) and (2), the lobes

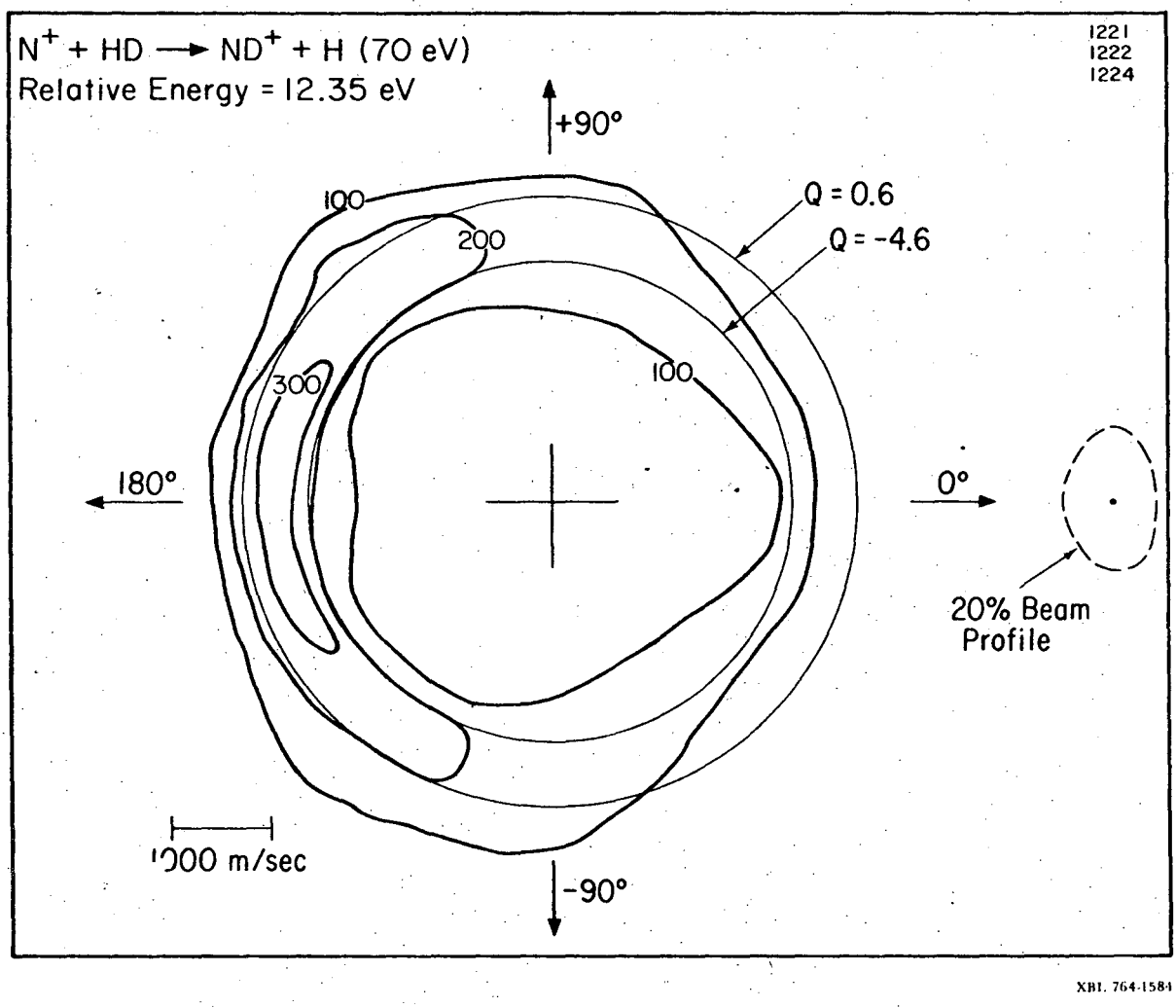
$N^+ + HD \longrightarrow ND^+ + H$ (70 eV)
Relative Energy = 12.35 eV
1221
1222
1224
+90°
100
200
300
100
Q = 0.6
Q = -4.6
180°
0°
20% Beam Profile
1000 m/sec
-90°
XBL 764-1584

Figure IV-13

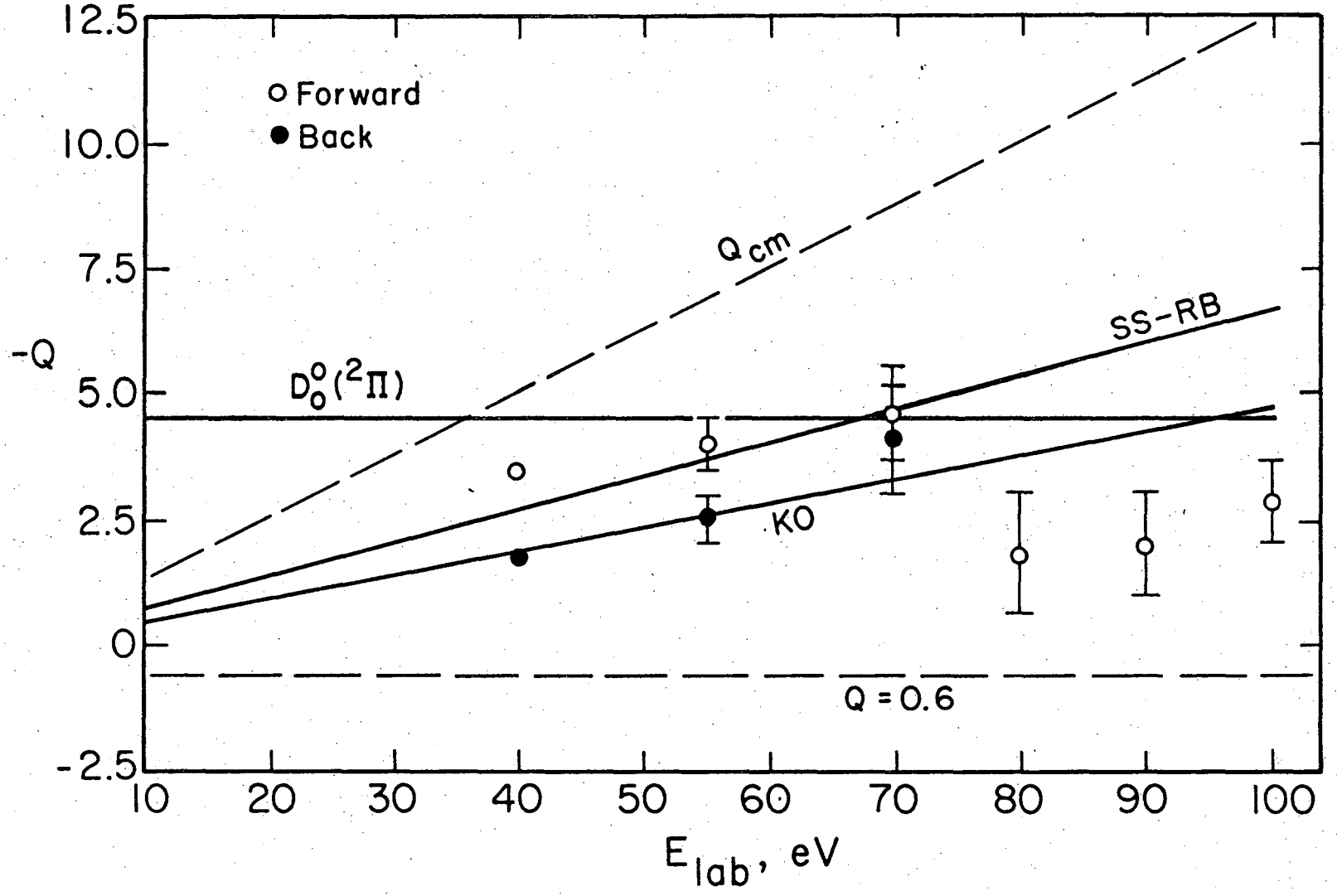


XBL 765-1767

Figure IV-14. Peak value of Q as a function of $E_{lab}$ for $H_2$ target.

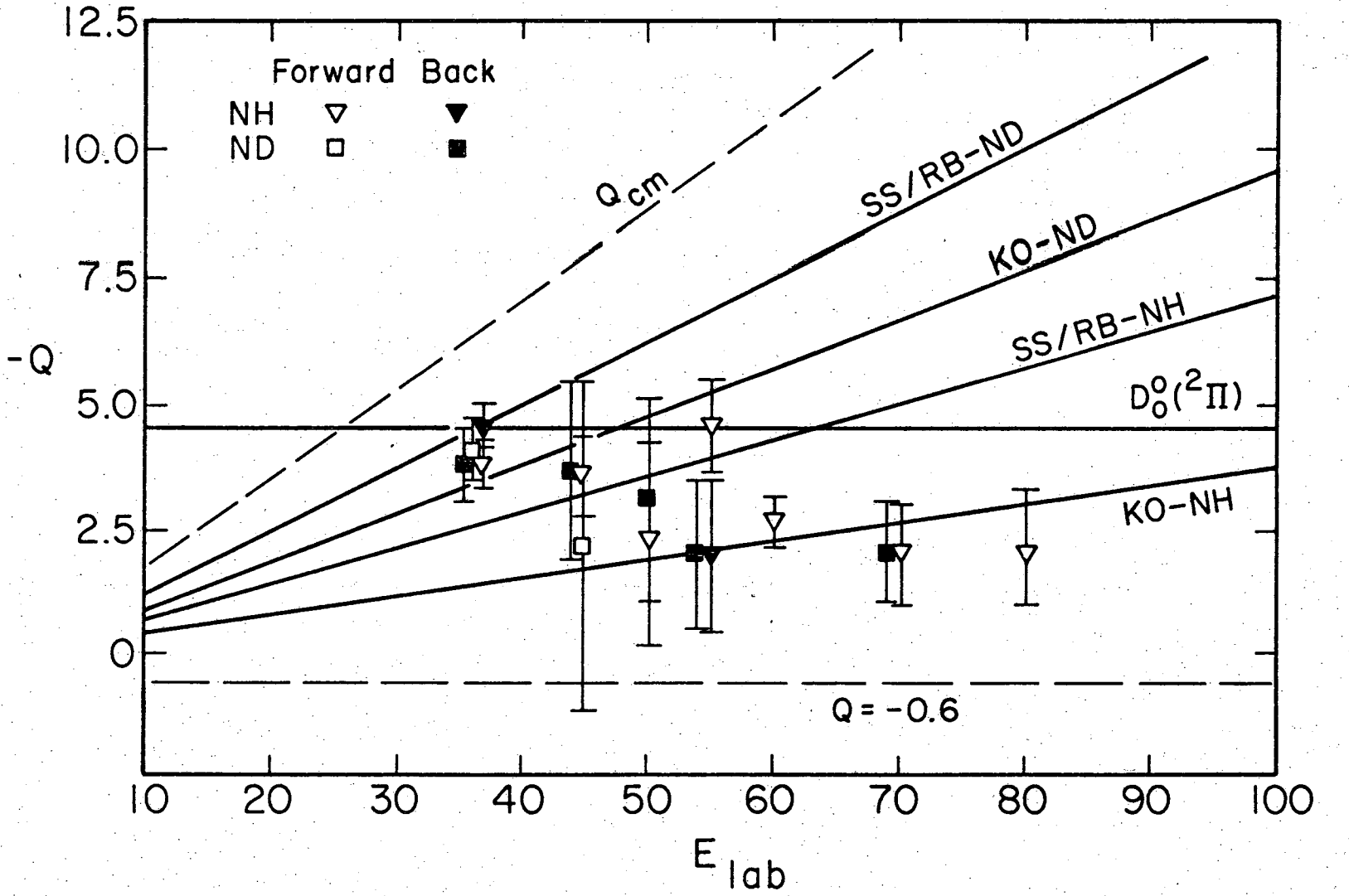


XBL 765-1766

Figure IV-15. Peak value of Q as a function of $E_{lab}$ for HD target.

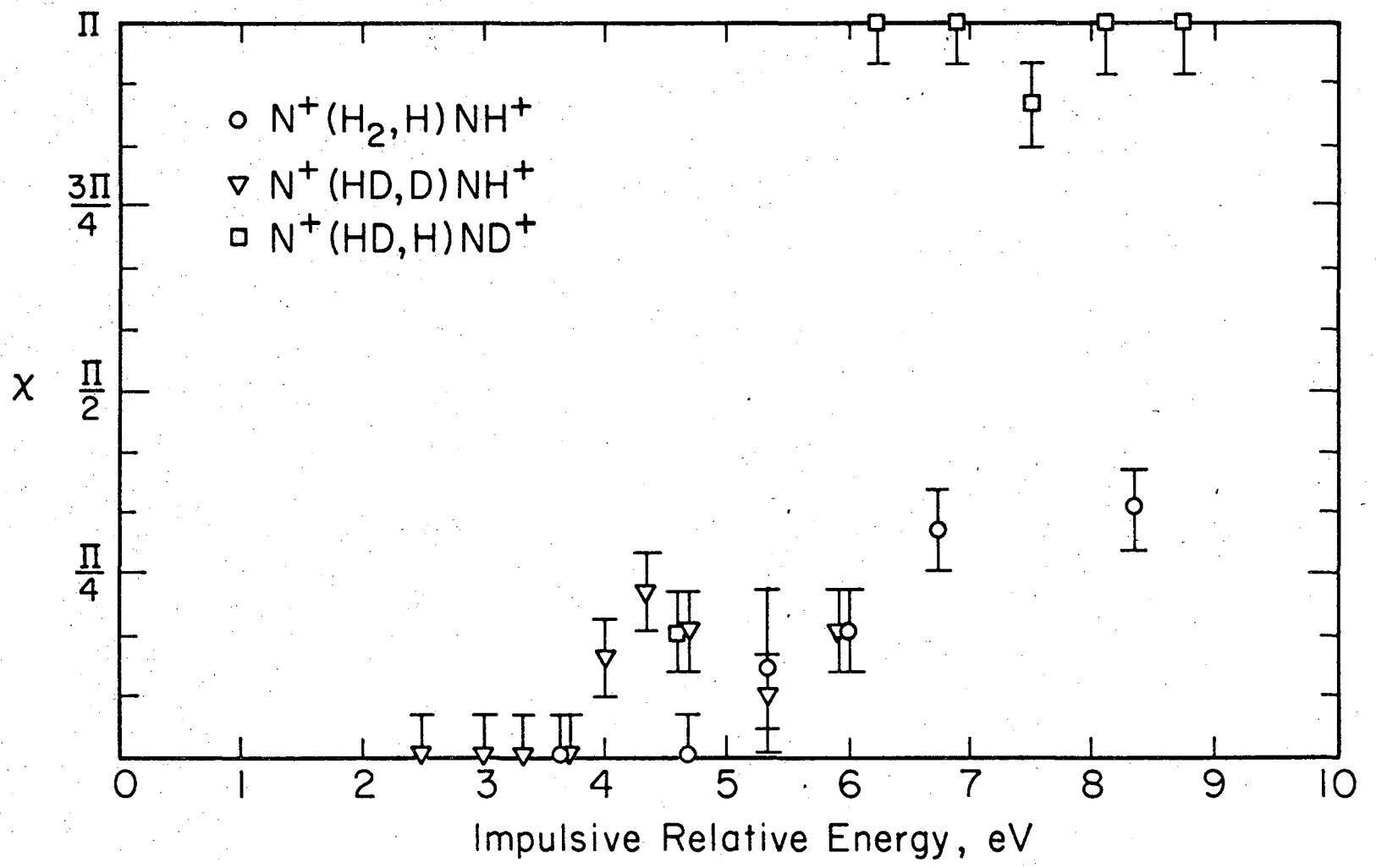


XBL 765-1765

Figure IV-16. Peak value of $|\chi|$ as a function of the impulsive relative energy $E_A(\frac{B}{A+B})$.

remain at an essentially constant CM angle and are the dominant feature of the map up to the highest energies. At the upper limits studied, a small residual peak on the centerline is observed. For reaction (3), the maps are dominated at all higher energies by a peak located at 180° in the CM system. Above the stripping limit, the energy of all peaks tends towards the center of the stability region.

## C. Non-Reactive Scattering

Our investigation of the non-reactive scattering events described by equations (5) and (6) covered the relative energy range from 6.8 to 15.6 eV. Five maps were obtained, in addition to centerline product energy distributions at a number of collision energies. The maps are presented as Figures IV-17 through IV-21. The Q circles shown in the figures represent the energies of a number of possible endothermic processes: Table IV-I collects the various values.

Two features stand out in each of the maps presented. The first is the cratered shape of the distribution, with product at all angles found at an essentially constant distance from the center of mass. The area near the centroid is devoid of scattered product, and the maximum intensity lies at moderately endothermic values of Q. For example, in Figure IV-20 the peak intensity is found at a Q value of -6.4 eV, far less than the maximum possible endothermicity of 15.6 eV. These results contrast with the behavior observed by Winn for the $O^+$ ion, where the product was scattered impulsively about the N-H center of mass instead of the system centroid.[2]

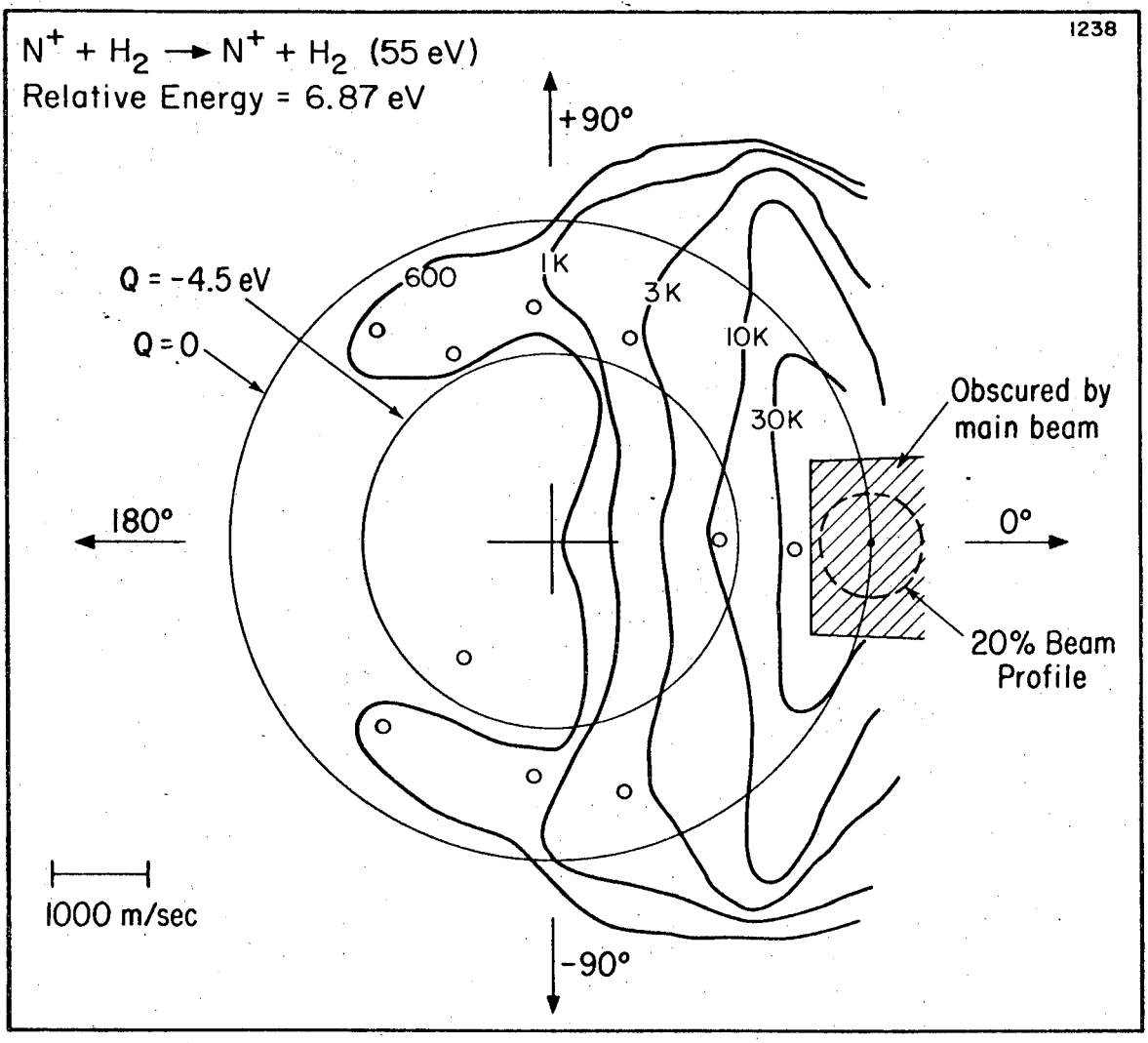


Figure IV-17

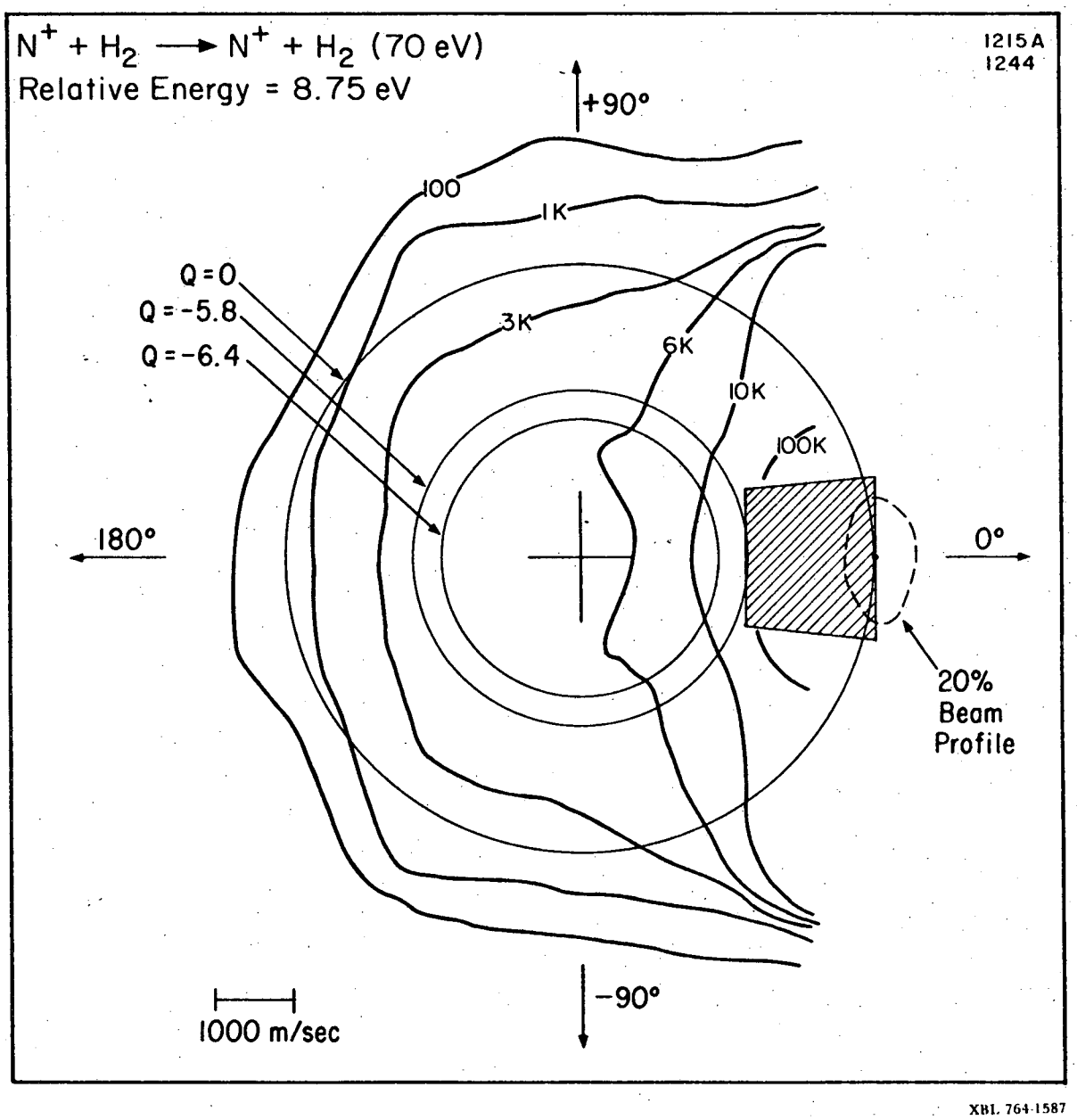
$N^+ + H_2 \longrightarrow N^+ + H_2$ (70 eV)
Relative Energy = 8.75 eV
1215A
1244
+90°
100
1K
3K
6K
10K
100K
Q = 0
Q = -5.8
Q = -6.4
180°
0°
20%
Beam
Profile
-90°
1000 m/sec
XBL 764-1587

Figure IV-18

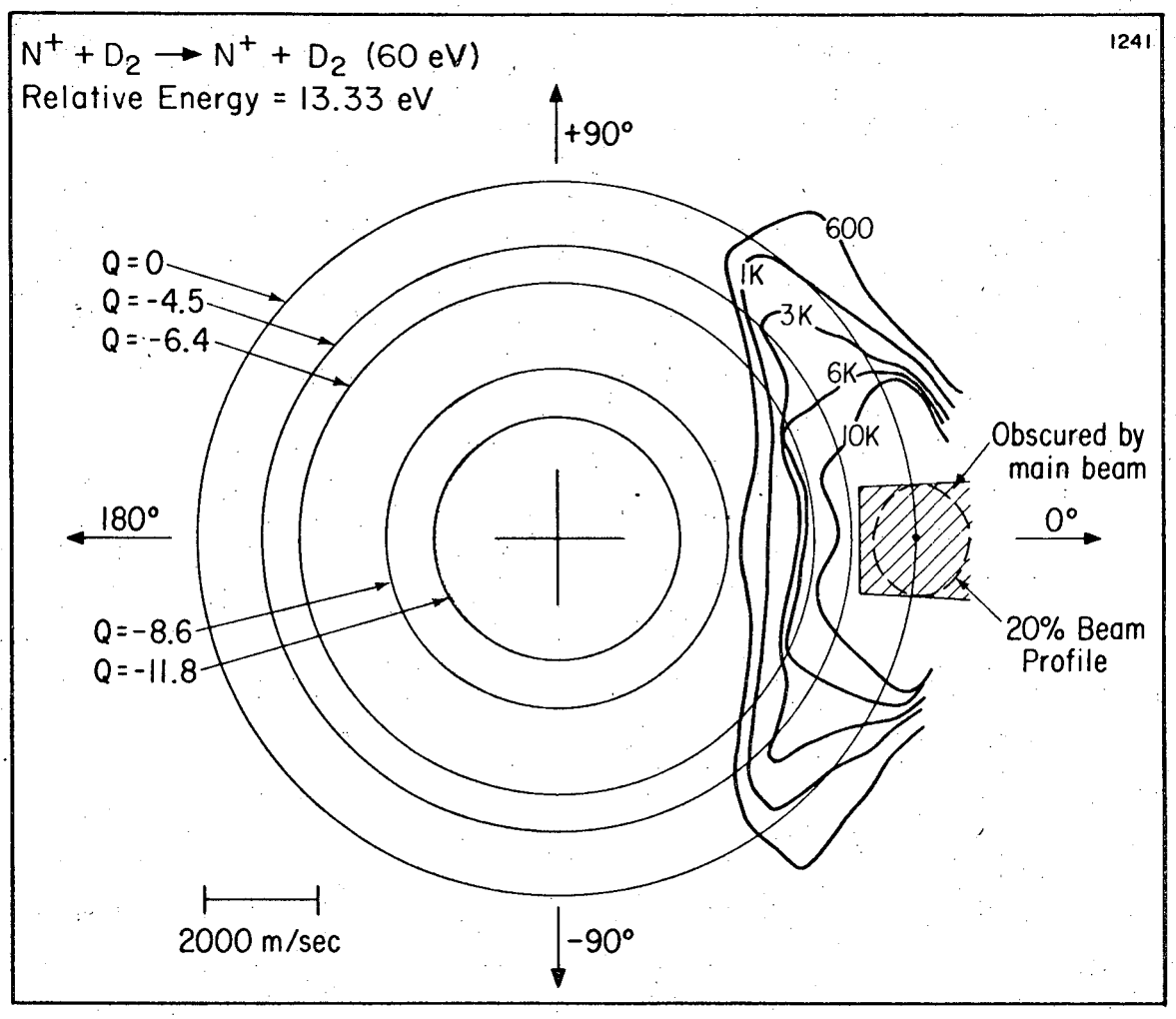


Figure IV-19

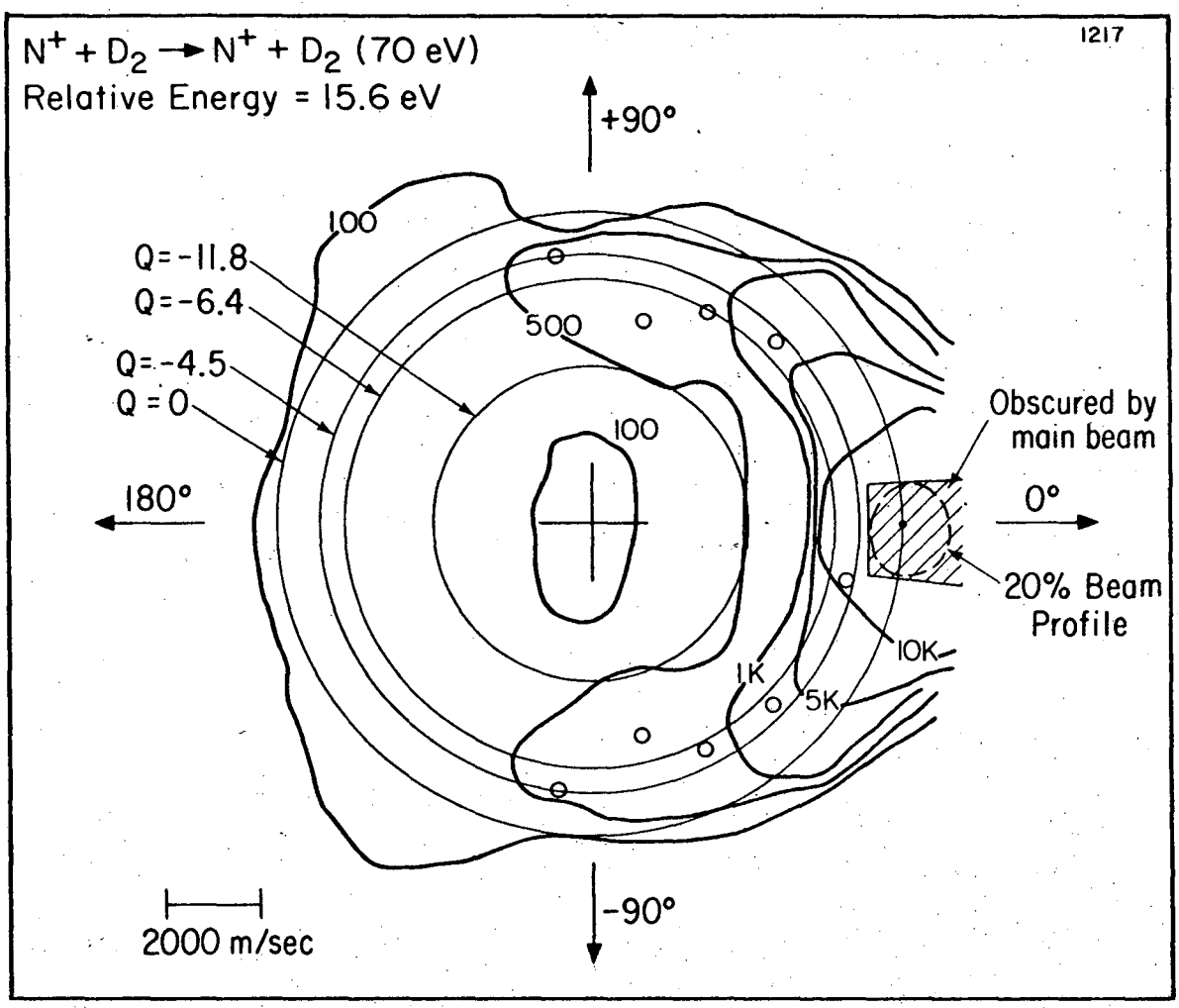
$N^+ + D_2 \rightarrow N^+ + D_2$ (70 eV)
Relative Energy = 15.6 eV
1217
+90°
100
Q=-11.8
Q=-6.4
500
Q=-4.5
Q=0
100
Obscured by main beam
180°
0°
20% Beam Profile
10K
1K
5K
-90°
2000 m/sec
XBL 764-1595

Figure IV-20

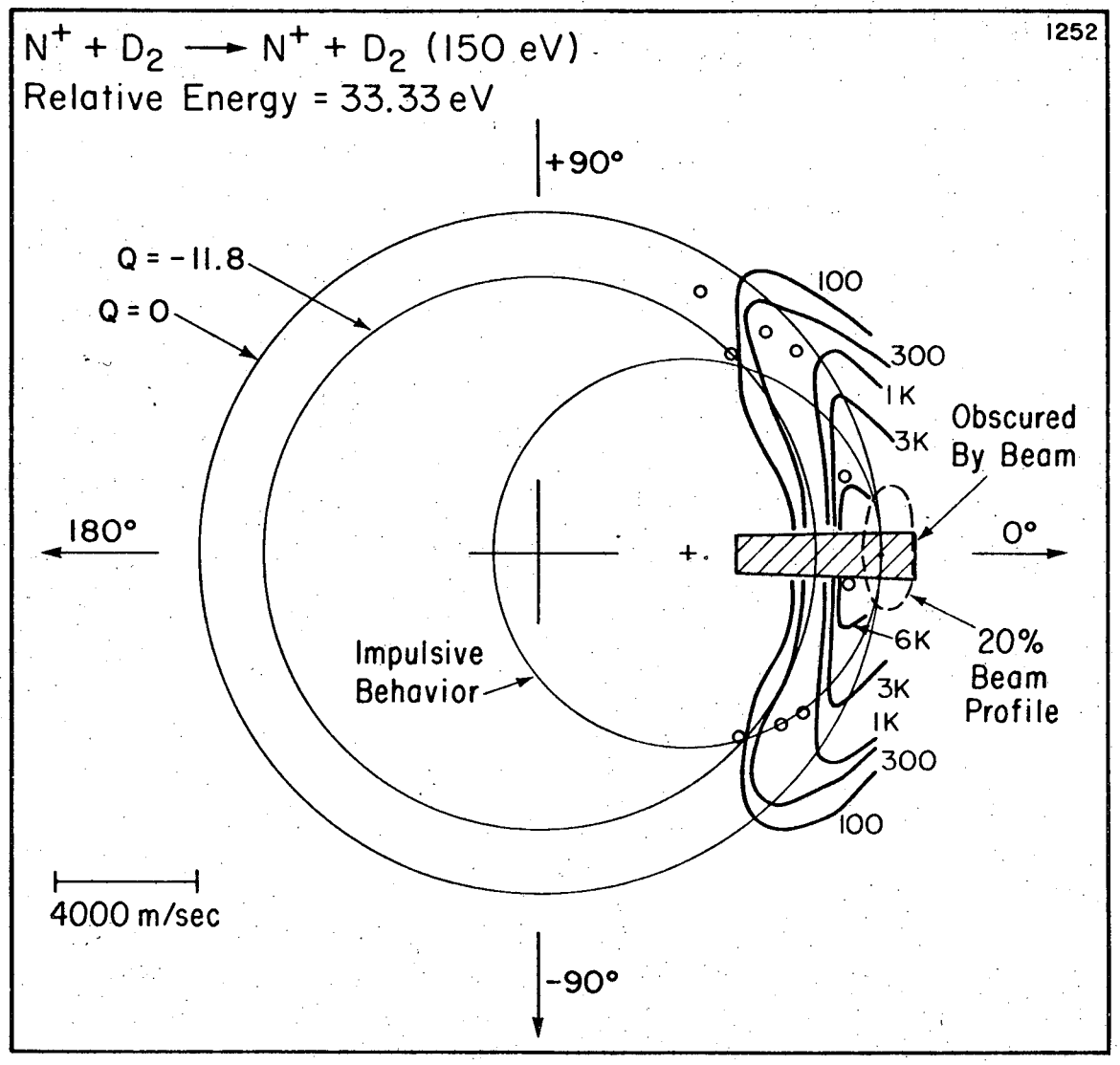


XBL 765-1763

Figure IV-21

TABLE IV-I

Energies for some Transitions of Interest

| Energy | |
|---|---|
| 1.9 eV | $N^+(^3P) + H_2 \rightarrow N^+(^1D) + H_2$ |
| 4.1 | $N^+(^3P) + H_2 \rightarrow N^+(^1S) + H_2$ |
| 4.5 | $N^+(^3P) + H_2 \rightarrow N^+(^3P) + H + H$ |
| 5.8 | $N^+(^3P) + H_2 \rightarrow N^+(^5S) + H_2$ |
| 5.9 | $N^+(^3P) + H_2 \rightarrow N^+(^2D) + H^+ + H$ |
| 6.4 | $N^+(^3P) + H_2 \rightarrow N^+(^1D) + H + H$ |
| 11.8 | $N^+(^3P) + H_2 \rightarrow N^+(^3D) + H_2$ |

Also prominent in the figures is the overwhelming concentration of the product at very small angles, near the beam position. This tendency, while marked at all energies, appears to increase somewhat with increasing beam energy.

For comparison, we also investigated the non-reactive scattering of nitrogen ion from helium at 15.6 eV. The energy and masses in this experiment are the same as those in Figure IV-20; thus we would hope to retain the kinematic features of the scattering while removing those due to the chemistry of the system. The result is shown in Figure IV-22. The scattering lies on the elastic circle, and shows considerably more intensity at moderately large angles than the $H_2$ and $D_2$ maps. Also apparent is a second ridge of intensity at a Q value of about -11.4 eV. This corresponds to the excitation of nitrogen ion from the $^3P$ to the $^3D$ state with an energy of 11.8 eV. We do not observe a transition corresponding to excitation of $^1D$ nitrogen ion to the $^1S$ state. Such a transition was observed by Tsao using electron impact ionization of nitrogen; our failure to observe it supports the arguments of Chapter II regarding the greater state purity of ion beams from microwave discharge.[3]

Our results so far have shown low intensities of both reactively and non-reactively scattered product over most of the energy range studied. Since the scattering gas pressure is chosen to provide a beam attenuation of about 15% for each experiment, the question arises as to how the remainder of the reactant beam is consumed. The most plausible channel not yet mentioned is that of charge exchange, reaction (8).

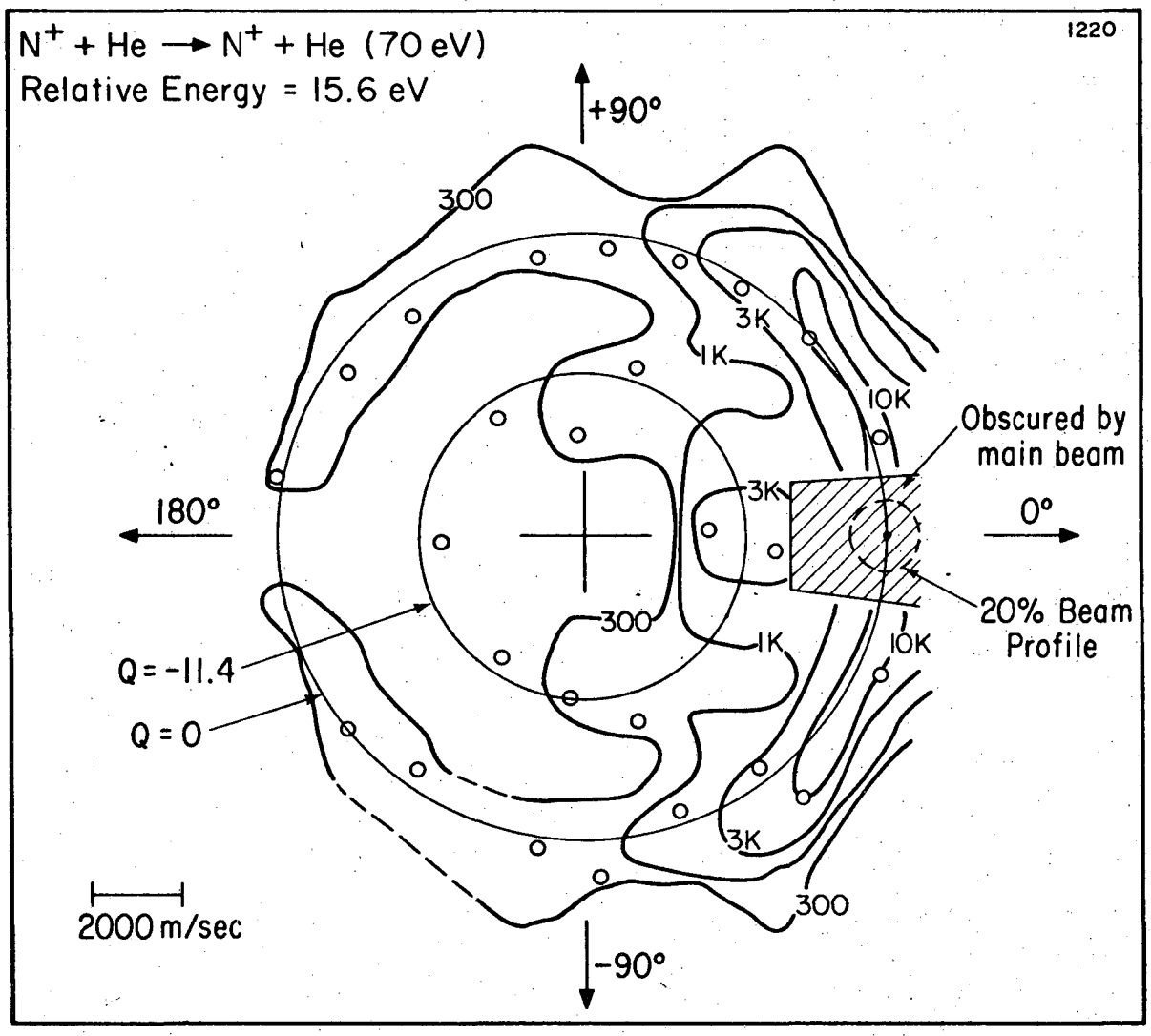
N+ + He → N+ + He (70 eV)
Relative Energy = 15.6 eV
1220
+90°
300
3K
1K
10K
Obscured by main beam
180°
0°
3K
300
1K
10K
20% Beam Profile
Q = -11.4
Q = 0
3K
300
2000 m/sec
-90°
XBL 764-1596

Figure IV-22

Unfortunately, the energy of the ionic product from charge exchange would be in large part below the detection threshold of our apparatus. The principles of Chapter I allow us to write the maximum laboratory velocity of the scattered hydrogen molecule:

$$v'_{H_2^+} \leq 2v_{cm} = \frac{2A}{M} V_a. \tag{9}$$

The corresponding laboratory energy is thus:

$$E'_{H_2^+} \leq \frac{B+C}{2} v'^2_{H_2^+} = 4 \frac{B+C}{M} \frac{A}{M} E_A \tag{10}$$

or about 31 eV for a 70 eV beam. The bulk of the product would lie at considerably lower energies still.

As an alternative to a complete measurement of the charge-exchange product distribution, however, we can collect the low-energy ion current and at least obtain a total cross-section for the process. Our apparatus is equipped to perform such a collection. An electrode near the wall of the scattering cell, roughly parallel to the beam, may be connected to an electrometer and floated at -20 volts. Ions of an energy less than the float voltage should be drawn out of the beam region to the electrode. In practice, of course, whether an ion is collected depends not only on the magnitude of its kinetic energy, but also on its initial location and direction of motion. Ions with trajectories which reach the cell walls or exit the cell before reaching the electrode will not be counted.

We have measured the low-energy ion current resulting from scattering a 70-eV beam from hydrogen as a function of the hydrogen gas pressure. The current is found to be proportional to pressure, and its magnitude is equal to about 60% of the corresponding beam attenuation. The pressure dependence is that expected for a reactive process such as charge exchange. The measured cross-section at 70 eV is about 25 $\mathring{A}^2$, which is probably a lower bound to the actual value. The magnitude of the current, considering that the collection efficiency is almost certainly less than unity, compels the conclusion that charge exchange is the predominant reaction channel at higher energies.

## References

1. Eric A. Gislason, Bruce H. Mahan, Chi-Wing Tsao and Arthur S. Werner, J. Chem. Phys. 54, 3897 (1971).

2. John S. Winn, Ph.D. Thesis, University of California LBL Report 1820 (1973, p. 216 ff.).

3. Chi-Wing Tsao, Ph.D. Thesis, University of California LBL Report UCRL-19140 (1970), p. 46-48.

# CHAPTER V

# CONCLUSIONS

## A. General Observations

Several conclusions may be drawn immediately from the experimental results of Chapter IV. One of these is the obvious importance of charge exchange in the dynamics of the system. We have previously mentioned that charge exchange appears to be by far the most important reactive channel at energies in the trans-stripping regime. While we have no direct evidence as to the details of the process, some indirect information may be gleaned from the non-reactive scattering shown in Figures IV-17 to IV-21.

We noted in Section IV-C the predominance of small-angle-scattering--or, conversely, the dearth of larger-angle scattering--in the non-reactive results. In addition, the reactive cross-sections above the stripping limit are exceedingly small. It seems only reasonable to assume that the "missing" $N^+$ product has been consumed by charge exchange. Small angle scattering is associated with grazing collisions, while more substantive encounters produce scattering to larger angles; the evidence thus implies that essentially all close-in collisions lead to charge-exchanged product. Supporting this conclusion is the distribution of the non-reactive scattering about the system center of mass. Close interactions of an impulsive nature, in which the projectile

"sees"clearly the bimolecular nature of the target, should produce scattering centered about the A-B and A-C centroids, as was observed in the $O^+ - H_2$ system.

None of the potential surfaces shown in Figure III-1 connects the reactants to the charge-exchanged products. Charge exchange must thus involve a transition from one surface to another, which we would expect only where surfaces of the same symmetry become close. There are two close approaches of appropriate surfaces in the diagram. One is the previously mentioned convergence of two $^3\Sigma^-$ surfaces as the linear $NHH^+$ configuration dissociates to $(NH + H)^+$. A transition at this point could produce $N(^4S)$ and ionized hydrogen. Another possibility is in the area of the correlation diagram representing perpendicular approach of the $N^+$ ion to form bent $HNH^+$. Here there is an avoided crossing of two $^3B_1$ surfaces, one arising from the reactants, and the other from hydrogen molecular ion and $N^+(^2D)$. This crossing, while avoided in the state correlation diagram, occurs as shown by the straight dotted lines in the poorer approximation of orbital correlation. Both transitions are energetically possible at all energies involved in our study: the first is endothermic by 0.94 eV and the second by 3.31 eV. An interesting object for future work at lower energies would be to investigate the charge exchange threshold energy in an effort to discriminate between the alternatives.

General conclusions may also be drawn from the reactive data presented. The direct nature of the reaction is marked,

as is the qualitative similarity to the $O^+ + H_2$ system. One exception to this resemblance is the small centerline forward peak which appears in Figures IV-4 and IV-9. It is our belief that this peak arises from the excited state reaction:

$$N^+(^1D) + H_2 \rightarrow NH^+(^2\Pi) + H. \qquad (1)$$

Strong evidence for this conclusion comes from the dependence of the center peak intensity on the method of beam preparation, reinforced by the attenuation results for the alternative beam sources. Table V-I presents the ratio of the center peak to the two side lobes in the $N^+ + H_2$ reaction at 15.6 eV, together with the excited state concentrations determined by attenuation experiments. The proportionality is convincing.

Since excited state concentration is independent of beam energy, why is the center peak not found at lower collision energies? We should first clarify exactly where such a peak is expected to occur. Previous experience with similar exothermic systems, as extensively reviewed in Chapter III, Section B, of this work, indicate that we can expect spectator stripping to predominate within the appropriate energy region. The predicted product velocity for stripping is independent of the heat of reaction; however, the stability limit for the model is not. We therefore expect a peak at the stripping velocity when the resulting Q value exceeds -2.1 eV. Above that energy, whatever mechanism becomes preeminent, we may expect a reasonably smooth progression of the peak towards Q = -4.6 eV, where we find it at the highest

TABLE V-I

Dependence of High-energy centerline peak upon beam state composition

| Ion Source Gas | Ratio of center to side peaks* | Excited state concentration |
|---|---|---|
| $N_2$ | 1 | <3% |
| $NH_3$ | 2 | 3% ± 3% |
| $N_2O$ | 4 | 6% ± 3% |

* For $N^+ + H_2 \rightarrow NH^+ + H$ at 125 eV LAB.

energies. Experience also calls for a marked drop in product intensity in this region.

A re-examination of the lower energy scattering maps now explains the elusiveness of the excited-state product peak. At the lower energies it should strictly coincide in location with the ground state product peak. In the intermediate energy range, where ground state stripping is stable but excited-state stripping is not, the latter will be at best a small peak very near the maximum intensity of the former. At yet higher energies, when the two lobes off the centerline come to dominate the maps, they remain linked with a bridge of non-zero intensity crossing the centerline which may either mask or comprise the excited-state scattering. Only at the highest energies, when the ground state scattering intensity essentially disappears, will the excited-state product become clearly observable.

If the centerline peak does indeed arise from the stabilization of impulsively-formed product by product repulsion, then the potential energy available for such repulsion must at least equal the excess internal energy of the product as initially formed. The relative energy of the ion to the abstracted H atom is 7.8 eV in the $H_2$ case, and lower in the HD case. Some 3.2 eV of this must be lost to produce the stable product observed near Q = -4.6 eV. The exothermicity of reaction (1) is 2.5 eV as written. If the barrier shown in the correlation diagram, Figure III-1, exists as shown, an additional 1 eV or so will be available

to product repulsion, and the energetics of excited state explanation are reasonable. On the other hand, if the argument is reversed, our evidence may be used to suggest an activation energy of at least some .7 eV for reaction (1).

To draw more detailed conclusions about the reactive dynamics of the system, some mathematical treatment may be necessary. The resemblance of the $N^+$ to the $O^+$ scattering suggests that the same methods may be applicable. In the $O^+$ case, considerable insight was gained from consideration of sequence of hard-sphere collisions. In this model, the incident ion, A, collides impulsively and elastically with one member of the target molecule, B. Atom B then collides with C elastically and impulsively. The trajectories of the three particles are then examined to see if AB product results. We shall refer to this mechanism as the sequential impulse problem.

## B. Collinear Sequential Collisions

We shall commence our consideration of the sequential impulse problem with the collinear special case, where all three atoms are constrained to lie in a line. This restriction achieves an immediate simplification of the problem. Of the nine degrees of freedom available to three bodies, three define the location of the system center of mass and two the absolute orientation of the system in space. Therefore, only four coordinates are required to describe relative motion of the bodies, and two of these are used to describe

the bending angles about the center particle. Fixing these angles equal to $\pi$ is the equivalent of the collinear assumption, and allows reduction of the degrees of freedom to two. Two coordinates fit nicely on a plain piece of paper, and allow easy visualization of the entire process.

The trajectories of collinear collisions may of course be obtained from the solution of equations of motion, but the method is lengthy if straightforward, and provides little intuitive insight. A preferable technique, sometimes referred to as the "skewed coordinate" method, allows solution of the entire collision problem by graphical means.[1] We commence by defining convenient coordinates. The "natural" coordinates for three bodies in collinear alignment are the two internuclear distances: $r_1$, the distance from A to B; and $r_2$, the distance from B to C. However, we shall use two other coordinates: X, the distance from the B-C centroid to the A atom, and Y, which is again the B-C distance. They are related to $r_1$ and $r_2$ by the equations:

$$X = r_1 + \gamma r_2 \tag{2a}$$

$$Y = r_2 \tag{2b}$$

where:

$$\gamma = C/(B+C). \tag{3}$$

Also, we may write the total relative kinetic energy T in terms of X and Y as:

$$T = \frac{1}{2}\frac{A(B+C)}{M}\dot{X}^2 + \frac{1}{2}\frac{BC}{B+C}\dot{Y}^2. \tag{4}$$

Now consider the effects of the substitutions:

$$x = X \tag{5a}$$

$$y = Y/a \tag{5b}$$

where a is a constant to be defined later. Substitution of these coordinates into equation (4) produces a new expression for the energy:

$$T = \frac{1}{2}\frac{A(B+C)}{M}\dot{x}^2 + \frac{1}{2}a^2\frac{BC}{B+C}\dot{y}^2. \tag{6}$$

It is useful to define a so that the coefficients of the two velocity terms are identical, that is:

$$T = \frac{1}{2}\frac{A(B+C)}{M}(\dot{x}^2+\dot{y}^2) \tag{7}$$

with:

$$a^2 = \frac{A(B+C)^2}{BCM}. \tag{8}$$

Equation (8) has a useful significance. If the course of the collision is plotted in the x - y system of Cartesian coordinates, it will describe the same motion as a particle of mass A(B+C)/M, sliding frictionless on a potential surface. The problem of the motion of three bodies in space is thus reduced to that of one body on a surface.

The simplest potential surface with a pretension to realism is the square-well type potential. Here the potential energy is considered infinite if the bodies approach within a certain minimum distance, and finite and positive beyond a given maximum. The energy is taken as zero between those bounds, producing a qualitative resemblance to the

attractive potential well between attracting atoms. Such a surface may be drawn in the $\underline{x}$ - $\underline{y}$ coordinate system if we can define lines of constant $r_1$ and $r_2$. Equations (2) and (5) may be made to yield the relations:

$$y = \frac{r_2}{a} = \frac{1}{\gamma_a}(x-r_1). \tag{9}$$

Therefore lines of constant $r_2$ parallel the x axis, while lines of constant $r_1$ have the slope $1/\gamma_a$. The angle between lines of constant $r_1$ and $r_2$ may be shown to be $\beta$, where,

$$\tan^2\beta = \left(\frac{1}{\gamma_a}\right)^2 = \frac{BM}{AC}. \tag{10}$$

The potential surface representing the square-well potential in the $\underline{x}$ -$\underline{y}$ system is shown in Figure V-1.

We may now release our frictionless mass point on this surface and observe its motion. If the reactants are atomic A and molecular BC, the point must begin in the attractive well at large $\underline{x}$ and small $\underline{y}$; collision will occur eventually if motion is toward the left. Motion parallel to the $\underline{x}$-axis represents zero vibrational energy in the B-C bond. If the trajectory has an initial angle $\theta$ to the $\underline{x}$-axis the vibrational energy $E_v$ is given by:

$$E_v = E \sin^2\theta \tag{11}$$

where E is the total kinetic energy of the system.

A reactive collision will eventually produce a particle trajectory in the attractive well for AB and moving toward large $\underline{y}$. Again, vibrational energy will be represented by

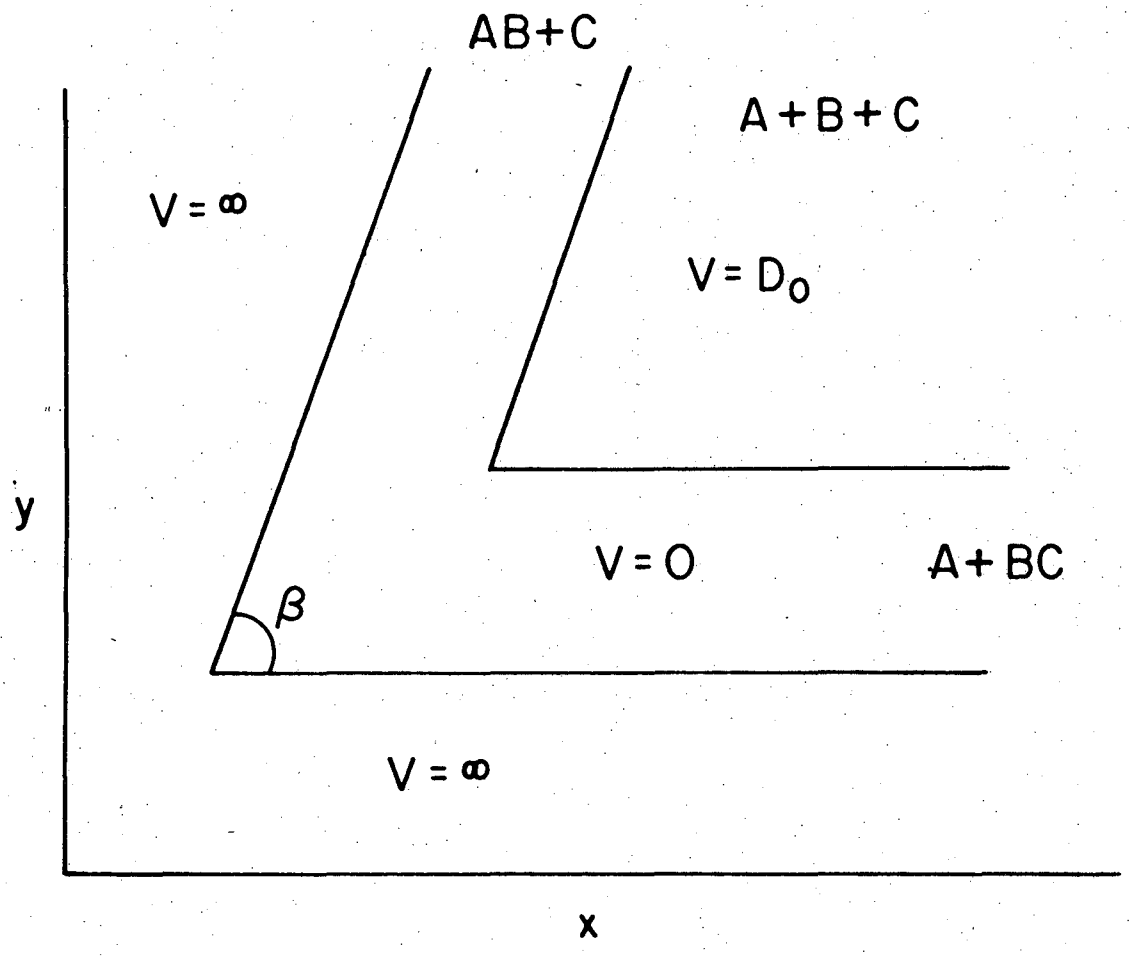


XBL 741-5402

Figure V-1. A square well potential for collinear A + BC → AB + C.

an angle $\theta'$ between the trajectory and the lines of constant $\underline{r}_2$, analogously to equation (11). If the collision sequence does produce product, simple geometry allows us to calculate $\theta'$ as a function of $\theta$ and $\beta$, and produces the relation:

$$E_v' = E \sin^2(\pi - 3\beta - |\theta|). \qquad (12)$$

Figure V-2 shows the effect of vibrational energy on several trajectories which occur when $\beta = 60°$.

Refinements may be added to the simple square well surface as desired. An obvious change is to account for exo- or endothermicity on the surface by means of energy wells and barriers. Simplicity is retained by introducing square potential energy steps. The result is a reflection or refraction of the particle trajectory as the step is encountered. Reflection results if the energy of the particle is less than the height of a barrier. Otherwise, the trajectory is refracted according to an analogue of Snell's Law:

$$E_1^{1/2} \sin\theta_1 = E_2^{1/2} \sin\theta_2. \qquad (13)$$

Here $E_1$ and $E_2$ are the total kinetic energies before and after crossing the energy step, and $\theta_1$ and $\theta_2$ are corresponding angles between the particle path and the ormal to the barrier. The effect of energy steps in the entrance and exit channels is illustrated in Figure V-3. We shall apply these methods with profit to the $N^+$ system, but first we shall examine the more general sequential impulse problem, where the atoms are free to move in three dimensions.

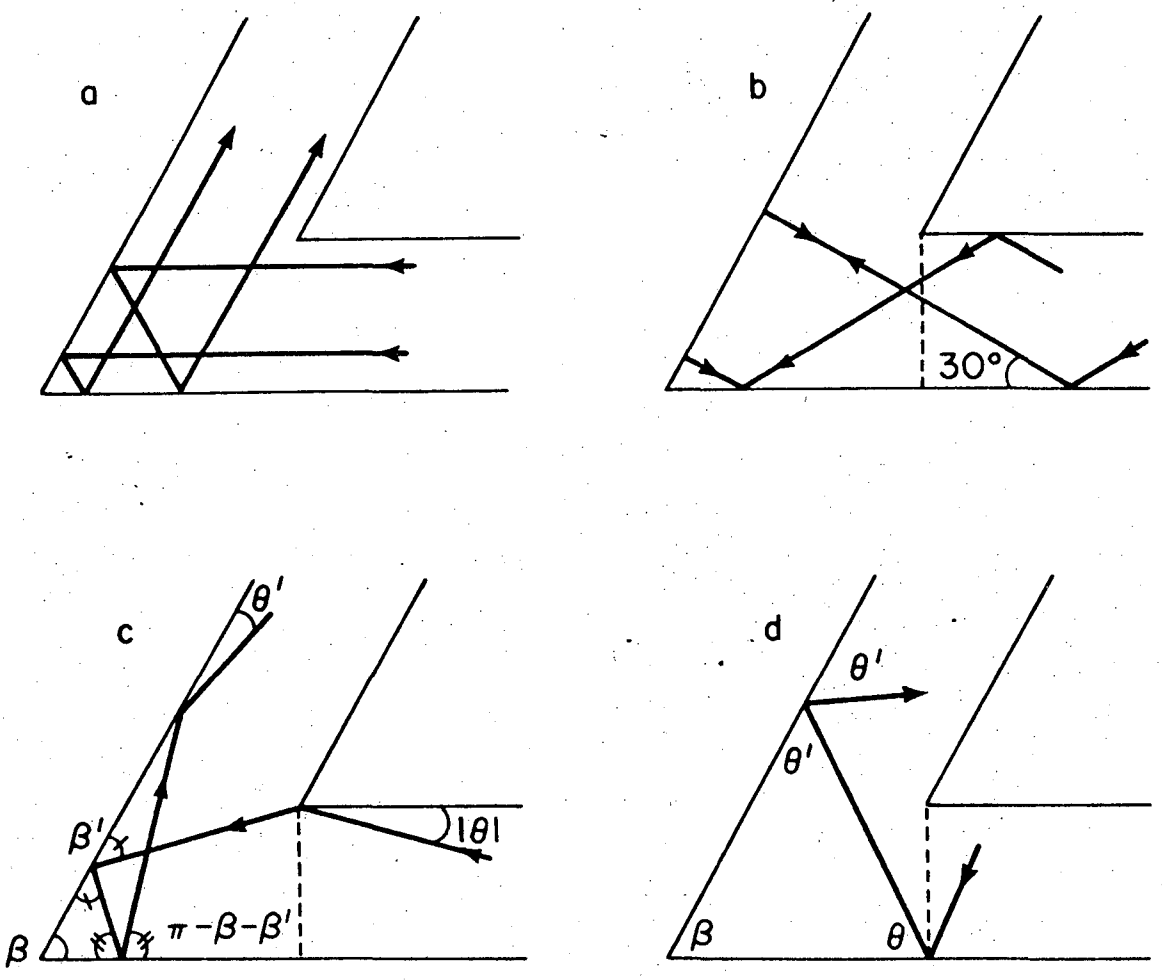


XBL 741-5401

Figure V-2. Effect of reactant vibrational energy $E_v$ on trajectories on a square-well potential surface, with $\beta = 60°$. (a) $E_v = 0$: all trajectories reactive. (b) $E_v = 1/2\ E$: all trajectories non-reactive. (c) $E_v < \frac{1}{2} E$, showing construction for finding $\theta'$. (d) $E_v > \frac{1}{2} E$, showing construction for $\theta'$.

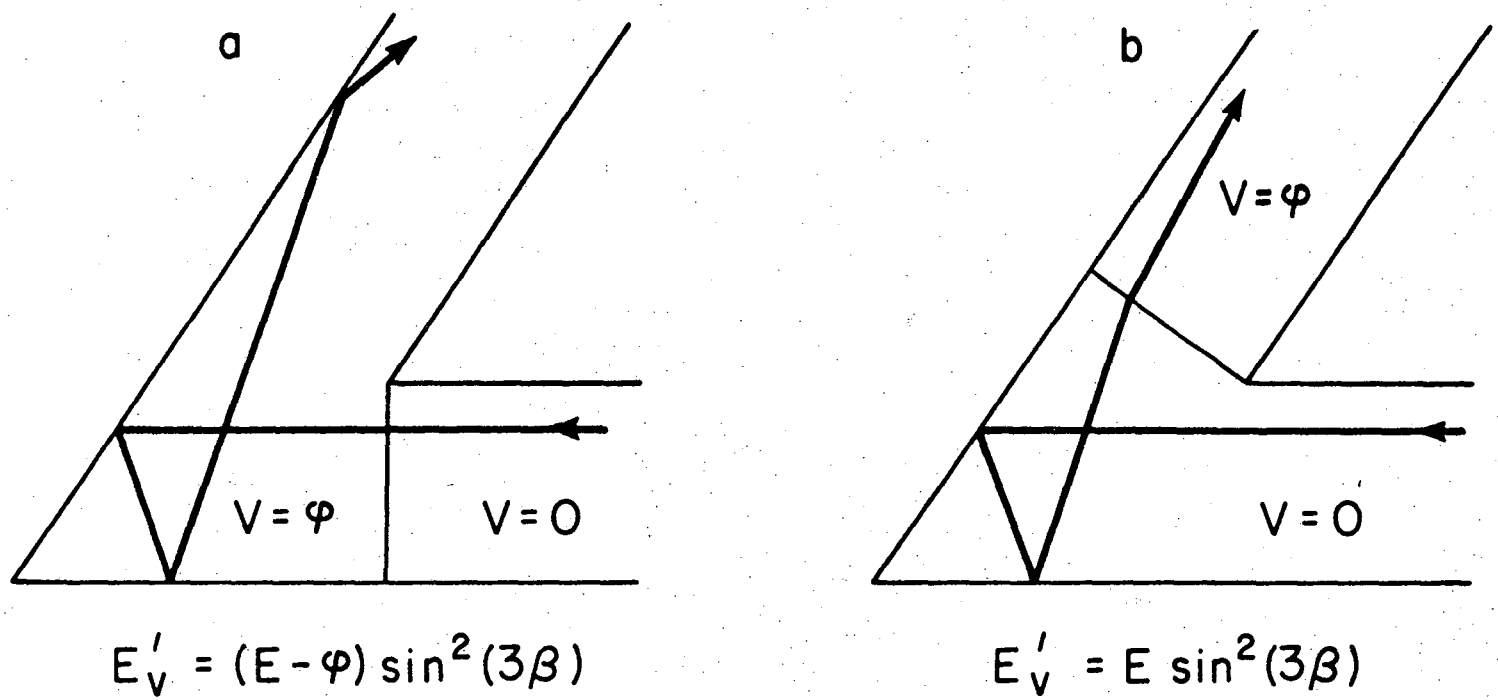


XBL 741-5400

Figure V-3. Effect of an energy step $\phi$ on trajectories on a square-well potential surface. (a) Step across entrance channel. (b) Step across exit channel. As shown, $\phi > 0$.

## C. Three-dimension Sequential Collisions

The collision sequence in which A strikes B, and B then strikes C, has been examined in three dimensions by Winn, who used trajectory methods, and by Mahan, who obtained a mathematical solution. The trajectory treatment, which was applied with considerable success to the $O^+ + H_2$ reaction, has been extensively documented elsewhere and will merely be sketched here.[2]

Winn used a FORTRAN program called BALLS to examine what he referred to as the Carom Model. Initially, the B atom, with radius $r_B$, is located at the origin, while the C atom, with radius $r_C = r_B$, is located at a distance $r_{BC}$ in a direction defined by the angles $\psi$ and $\Theta$ from B. The angle from the Z axis to the B-C internuclear axis is $\psi$, and the angle from the internuclear axis to the x-z plane is $\Theta$. Atom A of radius $r_A$ approaches B parallel to the z axis in the x-z plane, with unit velocity and an impact parameter $\underline{b}$. The radii $r_A$, $r_B = r_C$, $r_{BC}$, and the particle masses are taken from known properties of the reactant species, while $\psi$, $\Theta$, and $\underline{b}$ are varied to produce a number of initial conditions. The BALLS program produces 6878 sets of initial conditions for each of the four mass combinations possible when B or C equals H or D.

A collides with B, and the post-collision trajectories are computed from the laws of motion using hard-sphere potentials. B may then collide with C under the same conditions. The relative motions of A to B and to C are computed

and examined; if the relative energy of either pair is less than the dissociation energy of the corresponding molecule, a reactive event is considered to have occurred. It is weighted by the probability of the initial conditions which produced it. Angular and energy distributions are obtained for the reactive events and compared with the experimental results.

Numerical techniques, despite their frequent effectiveness, are inherently less satisfying than analytical solutions. A version of the Carom Model was cast into an integral equation by Mahan.[3] The result will be referred to as the Sequential Impulse Model (SIM).

The results of the Carom Model indicated that the effect of AC product on the distribution of scattered product was small. The SIM thus concentrates exclusively on the AB product distribution, again using the dissociation energy criterion for determining reactive events. The internal excitation and vector velocity of the AB product is related uniquely, by conservation of energy and momentum, to the vector velocity of the associated C product. The AB scattering map may thus be constructed if the C scattering map is known.

The C scattering can in turn be derived from the collision sequence by using a general result presented by Mahan. Let particle 1 with an initial velocity $\vec{v}_1$ strike particle 2 with initial velocity $v_2 = 0$. A simple graphical construction relates these values to the post-collision velocity of particle 2, $v_2'$, and the CM scattering angle $\chi_{12}$. The

perpendicular bisector of $\vec{v}_2'$ is found to bisect $\chi_{12}$ and to pass through the 1-2 centroid, which lies at $(m_1/(m_1+m_2))$ $\vec{v}_1$. The resulting formula for the magnitude of $v_2'$ is:

$$v_2' = 2 \frac{m_1}{m_1+m_2} \sin(\frac{\chi_{12}}{2}) \; v_1 \qquad (14)$$

where $m_1$ and $m_2$ are the particle masses. The sequential impulse scheme is a sequence of two collisions, each involving one partner at rest in the laboratory. Equation (14) may thus be applied twice in succession to obtain the final C velocity $v_C''$:

$$v_C'' = 4(\frac{A}{A+B})(\frac{B}{B+C}) \sin(\frac{\chi_{AB}}{2}) \sin(\frac{\chi_{AC}}{2}) \; v_A. \qquad (15)$$

This result is shown in graphical form in Figure V-4. The $\vec{v}_A$ or $\vec{v}_1$ vector is the beam velocity, and the $\vec{v}_C''$ or $\vec{v}_3''$ vector is an arbitrary C velocity. Also shown are two $\vec{v}_B'$ or $\vec{v}_2'$ vectors, representing possible outcomes of the first collision which may lead to the desired $\vec{v}_C''$ after the second collision. We observe the $\vec{v}_B'$ vectors to terminate on a circle drawn about the A-B centroid and through the origin. As we found in Chapter I, all $\vec{v}_B'$ vectors must end on this circle. For any $\vec{v}_B'$, moreover, the B-C centroid after the first collision must lie on $\vec{v}_B'$ at a distance $(B/(B+C))$ $\vec{v}_B'$ from the origin. As a result, the locus of all B-C centroids, after the first collision, lies on a circle of radius R, drawn about $R\hat{v}_A$. Here R is given by:

$$R = (\frac{A}{A+B})(\frac{B}{B+C}) \; v_A \qquad (16)$$

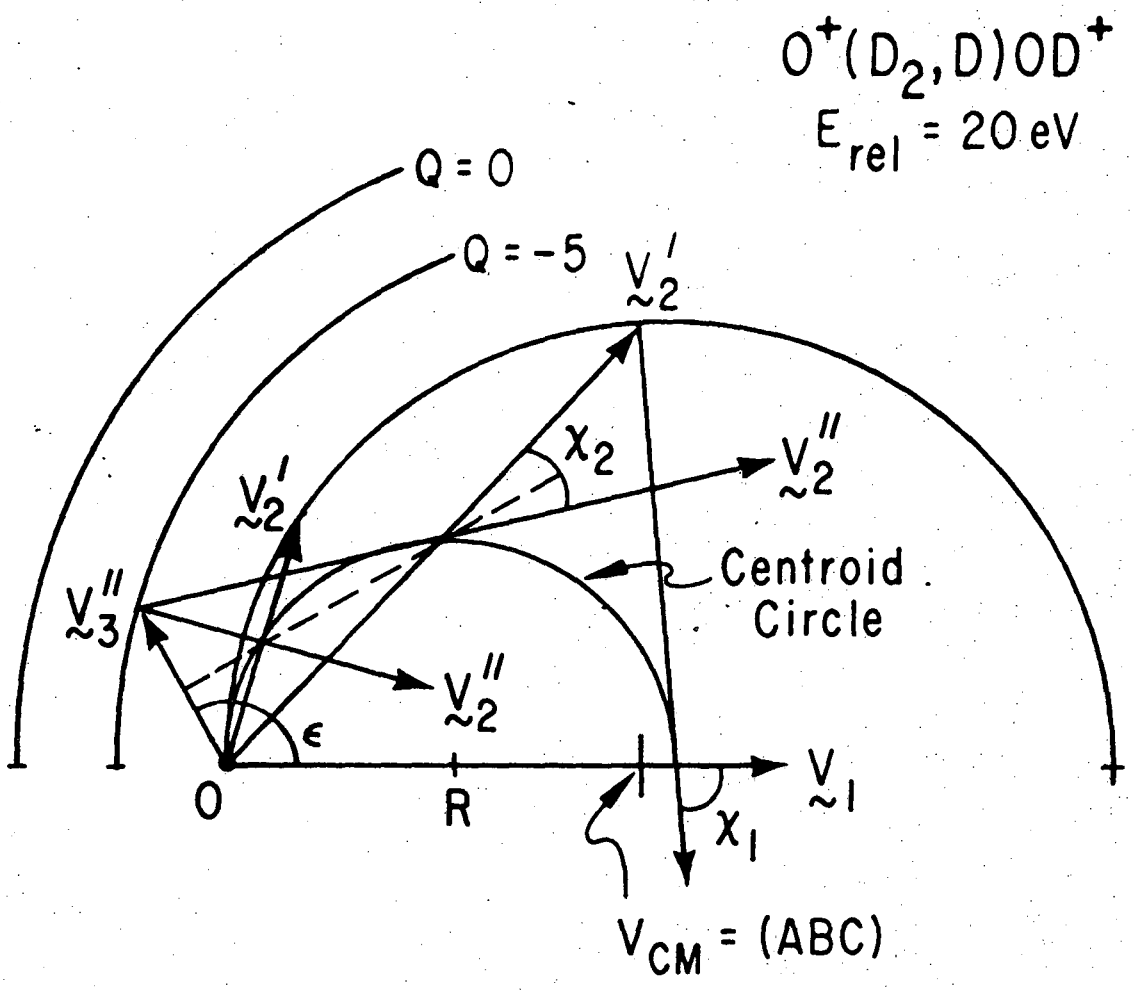


XBL 748-7056

Figure V-4. Construction for finding $\vec{v}_c''$ from $\chi_1$ and $\chi_2$ by the Sequential Impulse Model.

and $\hat{v}_A$ is the unit vector in the $\vec{v}_A$ direction. This circle shall be referred to as the centroid circle.

We are now able to find all of the $\vec{v}'_B$ vectors which can give rise to our arbitrarily chosen $\vec{v}''_C$. The centroids of these vectors must lie both on the centroid circle and on the perpendicular bisector of $\vec{v}''_C$. In the plane of the figure, there are only two such vectors, and they are the two shown. In three dimensions, the centroid circle becomes a sphere and the $\vec{v}''_C$ perpendicular bisector becomes a plane. Their intersection is a circle, designated by Mahan the "magic circle." On this circle lie the centroids of all $\vec{v}'_B$ vectors capable of giving rise to $\vec{v}''_C$. An interesting consequence of this construction is a limiting equation for the possible loci of $v''_C$. It may be shown that, in order to have a perpendicular bisector which intersects the centroid sphere, a $v''_C$ vector must have a magnitude given by:

$$v''_C \leq 2R(1+\cos\varepsilon) \qquad (17)$$

where $\varepsilon$ is the angle between $v''_C$ and $v_A$. We shall call the cardioid resulting from the equality in equation 17 the limiting cardioid.

Let us now turn to a quantitative evaluation of the scattering predicted by the Sequential Impulse Model.[4] We seek the flux of events into a differential volume, $d^3v''_C$ surrounding an arbitrary $v''_C$ vector, which we shall indicate by $F_C$. This flux will have units of time$^{-1}$ velocity$^{-3}$, so that $F_C\, d^3v''_C$ will have units of events/time. We may easily

express the number of initial A-B collisions in the same units of events/time. For unit scattering gas concentration, this quantity, $R_A$, follows from the definition of the A-B cross section $\sigma_{AB}$ as:

$$R_A = N_A v_A \sigma_{AB}, \tag{18}$$

where $N_A$ is the beam density. Once a B atom has been scattered, its probability of producing a desired $v_C''$ by a given route, $dP_v$, depends on a chain of independent probabilities. The first is $P_\omega$, the probability that $v_B'$ will be such as to produce a B-C centroid in a given surface angle element $d^2\omega$ on the centroid sphere. The second is $P_\chi$, the likelihood that the subsequent B-C collision will have the $\chi_{BC}$ required to give $v_C''$, according to equation (15). The product of these two probabilities is the chance of obtaining $v_C''$ by a chosen combination of $\chi_{AB}$ and $\chi_{BC}$. There are a number of such combinations leading to $v_C''$, and the total probability $P_C$ of any A-B collision producing the required C vector is given by summing over the combinations:

$$P_C = \int_{\text{all comb}} P_\chi \cdot P_\omega \tag{19}$$

Multiplying this probability times the rate of A-B collisions gives $F_C\, d^3v_C''$ in the proper units:

$$F_C\, d^3v_C'' = N_A v_A \sigma_{AB} \int P_\chi P_\omega \tag{20}$$

The volume element $d^3v_C''$ may of course be expressed in terms of the solid angle element $d^2\Omega$ and the velocity element $dv_C''$:

$$F_C v_C''^2 \, d^2\Omega \, dv_C'' = N_A v_A \, \sigma_{AB} \int P_\chi P_\omega . \qquad (21)$$

The probability $P_\omega$ of scattering B into a given solid angle element is found easily from the assumption of hard-sphere scattering. The differential cross-section for hard spheres is a constant, and thus the $v_B'$ vectors, as seen from the A-B centroid, are distributed uniformly in all directions. As a result, the centroid sphere is also populated uniformly, and the weight of any solid angle element $d^2\omega$ is simply equal to its area divided by the surface area of the sphere:

$$P_\omega = \frac{1}{4\pi R^2} R^2 d^2\omega . \qquad (22)$$

The probability $P_\chi$ requires somewhat more effort to obtain. Figure V-5A shows the B-C pair immediately after the A-B collision, and serves to define some useful quantities. The likelihood that $\alpha$ is in the range $\alpha, \alpha+d\alpha$ is equivalent to $P_\chi$, and is given by:

$$P_\chi = \frac{1}{4\pi} \sin\alpha d\alpha d\gamma . \qquad (23)$$

It is clear from the figure that:

$$\sin\alpha = b/r_{BC} \qquad (24)$$

$$d\alpha = db/r_{BC} \cos\alpha \qquad (25)$$

so that expression (23) becomes:

$$P_\chi = \frac{1}{4\pi r_{BC}^2} \frac{b db d\gamma}{1-b^2/r_{BC}^2} . \qquad (26)$$

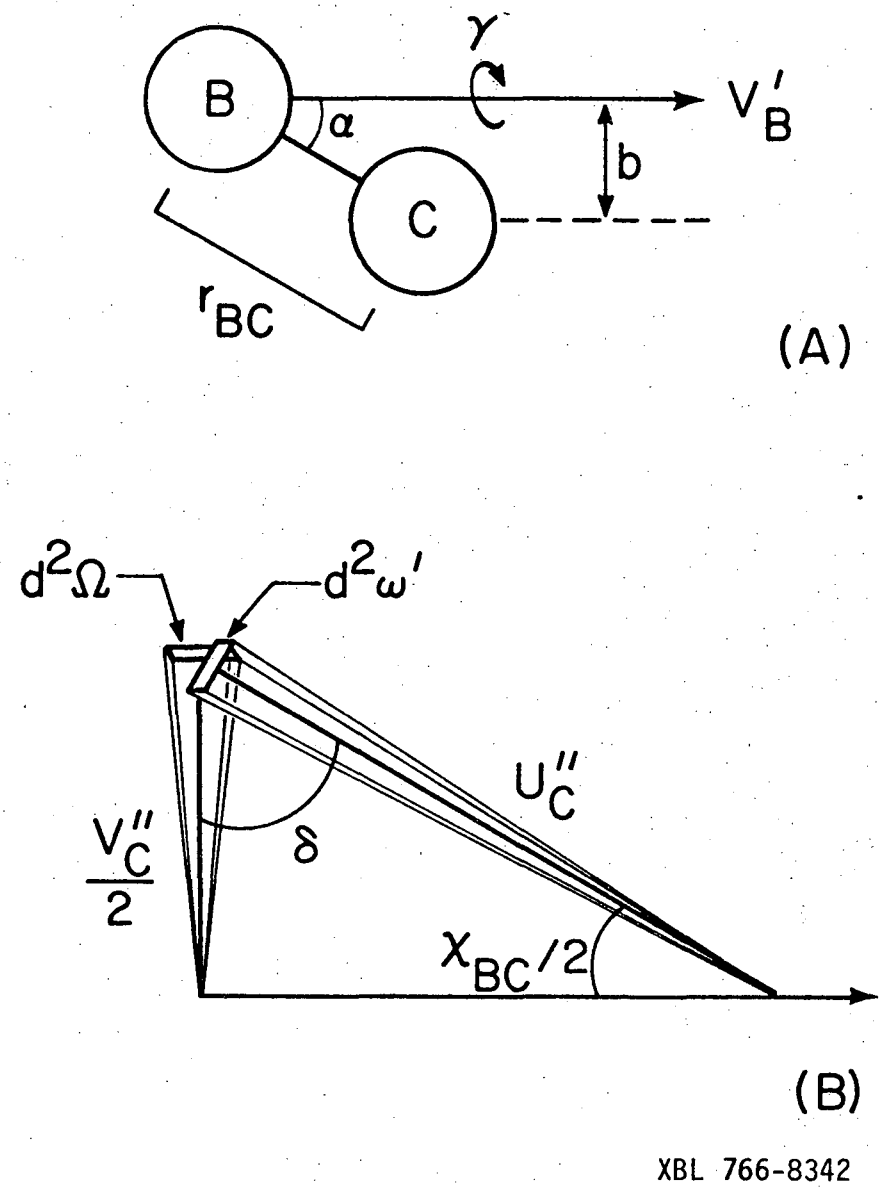


XBL 766-8342

Figure V-5. A. The B-C pair immediately after the first collision. B. The solid angle elements of equation (31).

We can rewrite this expression in terms of molecular parameters and the scattering angle $\chi$ by recalling the classical scattering formula:

$$bdb = I_{BC} \sin\chi \, d\chi \tag{27}$$

and the hard-sphere scattering result:

$$b^2 = d_{BC}^2 \cos^2 \chi/2, \tag{28}$$

where $d_{BC}$ is the sum of the radii of atoms B and C. Substituting these into equation (26) gives:

$$P_\chi = I_{BC}/4\pi r_{BC}^2 \frac{\sin\chi d\chi d\gamma}{\sqrt{1-d_{BC}^2\cos^2(\chi/2)/r_{BC}^2}} \cdot \tag{29}$$

Finally, we note that $\sin\chi d\chi d\alpha$ is simply the B-C CM solid angle element $d^2\omega'$ and write:

$$P_\chi = \frac{I_{BC} d^2\omega'}{4\pi r_{BC}^2} (1-d_{BC}^2/r_{BC}^2(\cos^2(\chi/2)))^{-1/2}. \tag{30}$$

It is useful to convert $P_\chi$ into LAB instead of CM coordinates. Figure V-5B shows the relation of $d^2\omega$ to the LAB solid angle element $d^2\Omega$. We may apply the standard LAB-CM volume element conversion:

$$v_C''^2 \, d^2\Omega = u^2 d^2\omega' \cos\delta. \tag{31}$$

The geometry of the figure allows this to be rewritten as:

$$d^2\Omega_{BC}/d^2\omega' = \frac{u^2}{v_C''^2} \sin\frac{\chi}{2}. \tag{32}$$

The CM velocity $\underline{u}$ lies on the perpendicular bisector of $v_C''$ and thus has the value:

$$u_{BC} = \frac{v_C''}{2} \frac{1}{\sin(\chi_{BC}/2)}. \tag{33}$$

Therefore:

$$d^2\omega' = 4\sin\frac{\chi_{BC}}{2}\, d^2\Omega \tag{34}$$

and:

$$P_\chi = \frac{1}{4\pi T_o^2} \frac{4I_{BC}\sin(\chi_{BC}/2)d^2\Omega}{(1-d_{BC}^2\cos^2(\chi_{BC}/2)/r_{BC}^2)^{1/2}}. \tag{35}$$

The next step in our derivation is to integrate over all possible routes to $v_C''$, as required by equation (19). Figure V-6 shows a method of carrying out this integration. The dotted circle is the magic circle for $v_C''$. The sphere is the centroid sphere with radius R. The coordinates $\theta$ and $\phi$ serve to define the volume element $d^2\omega$ in such a way that we may sum over all points on the magic circle by integrating in $\phi$ only. The magic circle, we recall, contains all of the points which may produce $v_C''$. With:

$$d^2\omega = \sin\theta d\theta d\phi \tag{36}$$

we can write the integral by combining $P_\omega$ and $P_\chi$:

$$P_v = \int_{\chi_{min}}^{\chi_{max}} \frac{\sin\theta d\theta d\phi}{4\pi\cdot 4\pi r_{BC}^2} \frac{4I_{BC}\sin(\chi/2)d^2\Omega}{(1-d_{BC}^2\cos^2(\chi/2)/r_{BC}^2)} \tag{37}$$

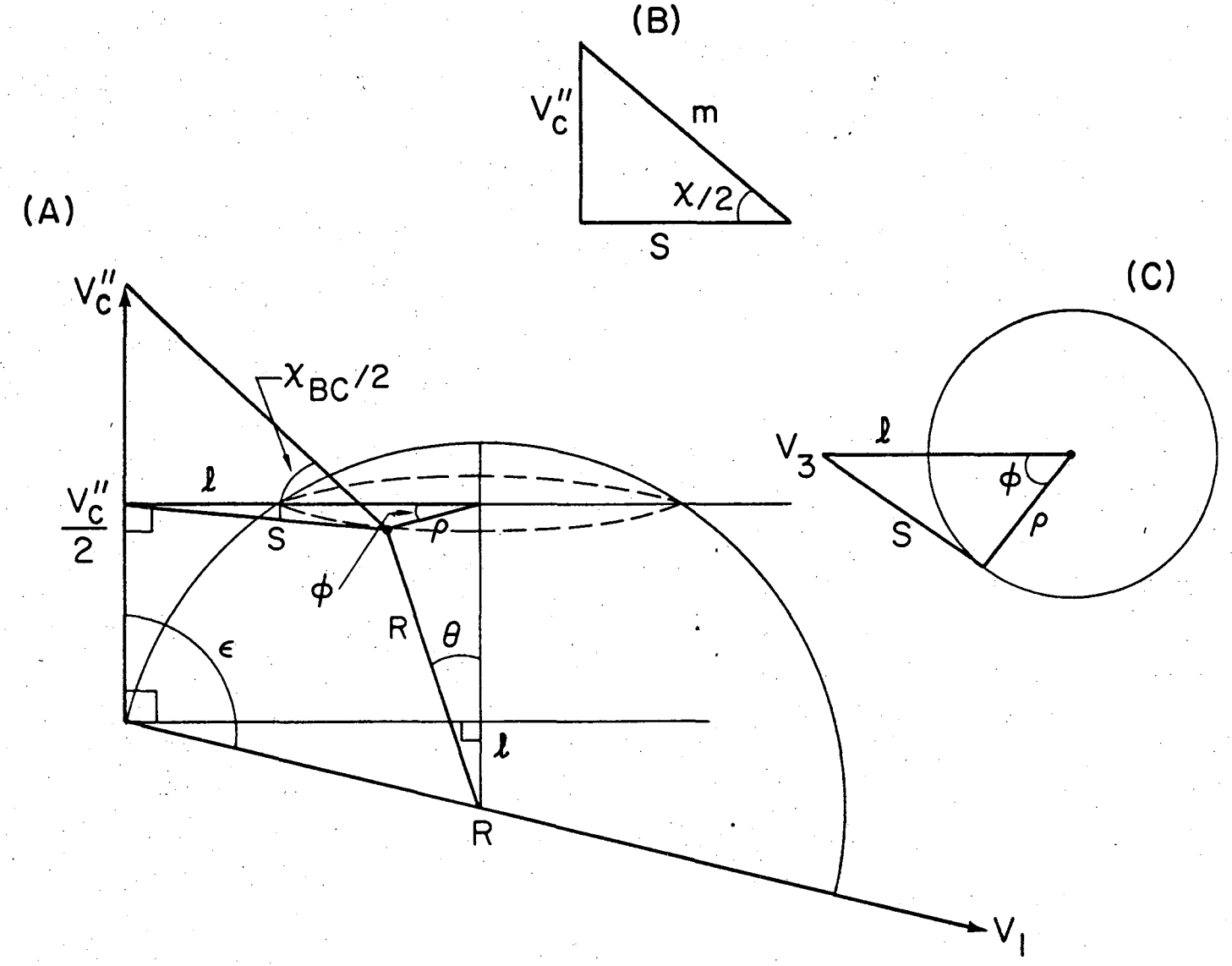


XBL 766-8344

Figure V-6. Relationships used to integrate the SIM problem. A. Overall. B. Detail of the $v_C''/2$,s,m triangle. C. Detail of the $\ell$,s,$\rho$ triangle.

The term $d^2\Omega$ is a property of $v_C''$ and will remain unchanged during the integration, as will the functions of $\theta$. The functions of $\chi$, however, are dependent on $\phi$.

Therefore $\chi$ and $\phi$ must be expressed in interdependent terms. Two triangles, shown in perspective in Figure V-6A and in plane in Figures V-6B and V-6C, allow this conversion. Using the Law of Cosines in the 1, s, $\rho$ triangle of Figure V-6C, we may write:

$$s^2 = \ell^2 + \rho^2 - 2\ell\rho \cos\phi. \tag{38}$$

The $v_C''/2$, s, m triangle, shown in Figure V-6B, illustrates the relationship:

$$s/(v_C''/2) = \cot\ (\chi_{BC}/2). \tag{39}$$

Eliminating s between the two equations yields:

$$\cot^2\left(\frac{\chi_{BC}}{2}\right) = \frac{4}{v_C''^2}\ (\ell^2+\rho^2-2\ell\rho\ \cos\phi) \equiv Z. \tag{40}$$

The quantity Z, defined by equation (34), proves useful in simplifying the integral. We may use it to express the functions of $\chi$:

$$\csc^2(\chi/2) = Z + 1 \tag{41a}$$

$$\sin\ (\chi/2) = (Z + 1)^{-1/2} \tag{41b}$$

$$\cos\ (\chi/2) = (Z/Z + 1)^{1/2} \tag{41c}$$

and to express functions of $\phi$:

$$\cos\phi = (Zv_C''^2/4 - \ell^2 - \rho^2)\left(-\frac{1}{2\ell\rho}\right) \tag{42a}$$

$$\sin\phi = \left[\frac{-16(\ell^2-\rho^2)^2 + 8v_C''^2 Z(\ell^2+\rho^2) - v_C''^4 Z^2}{64\ell^2\rho^2}\right]^{1/2} \tag{42b}$$

$$d\phi = \frac{v_C''^2}{8\ell\rho}\,\frac{1}{\sin\phi}\,dZ. \tag{42c}$$

Combining and simplifying gives equation (37) in terms of Z:

$$P_v = \frac{\sin\theta d\theta d^2\Omega I_{BC}}{4\pi^2 r_{BC}^2}\int_{\chi_{min}}^{\chi_{max}} v_C''^2\{[-16(\ell^2-\rho^2)^2 + 8v^2Z(\ell^2+\rho^2) - v^4Z^2] \times [Z(1-d_{BC}^2/r_{BC}^2)+1]\}^{-1/2}\,dZ. \tag{43}$$

A series of further substitutions produces an integral of a more easily recognizable form. Let:

$$\delta = 1 - d_{BC}^2/r_{BC}^2 \tag{44a}$$

$$\overline{Y} = \sqrt{Z+1/\delta} \tag{44b}$$

$$\alpha = -v_C''^4 \tag{44c}$$

$$\beta = 8v_C''^2(\ell^2+\rho^2) + 2\alpha/\delta \tag{44d}$$

$$\gamma = -16(\ell^2-\rho^2)^2 - 8v^2(\ell^2+\rho^2)/\delta - \alpha/\delta^2. \tag{44e}$$

Then:

$$P_v = \frac{I_{BC}\sin\theta d\theta}{2\pi^2 r_{BC}^2}\,\frac{v_C''^2}{\delta}\int_{\chi_{min}}^{\chi_{max}} (\alpha\overline{Y}^4 + \beta\overline{Y}^2 + \gamma)^{-1/2}\,d\overline{Y} \tag{45}$$

We recognize this as an elliptic integral, as may be made clearer by the further set of substitutions:

$$t = \bar{Y}/y+ \tag{46a}$$

$$C = y+/y- \tag{46b}$$

$$y\pm = \frac{1}{2\alpha}\left(-\beta\pm\sqrt{\beta^2-4\alpha\gamma}\right). \tag{46c}$$

These yield the familiar elliptic form:

$$\int(\alpha y^4+\beta y^2+\gamma)^{-1/2}\, dY = y\overset{2}{+}y- \int \frac{dt}{\sqrt{(1-t^2)(1-c^2t^2)}}. \tag{47}$$

Elliptic integrals have no analytical solution, although they have been extensively studied and their properties are well-known. For the moment, we shall indicate the integral as written in equation (43) by the symbol $I$:

$$P_v = \frac{\sin\theta d\theta d^2\Omega I_{BC}}{4\Pi^2 r_{BC}^4} I. \tag{48}$$

We note that $I$ and $P_v$ are both dimensionless, as befits probabilities.

We are now in a position to return to equation (20) and write an expression containing the desired flux $F_c$. Combining equations (20) and (48) gives:

$$F_C v_C''^2\, d^2\Omega\, dv_C'' = N_A v_A \sigma_{AB} \frac{d^2\Omega I_{BC}\sin\theta d\theta}{4\Pi^2 r_{BC}^2} I. \tag{49}$$

Referring again to Figure 6, we may eliminate the functions of $\theta$. We note that:

$$\cos\theta = \frac{v_C''/2-R\cos\varepsilon}{R}. \tag{50}$$

So that:

$$\sin\theta d\theta = -\frac{1}{2R} dv_C''. \tag{51}$$

Since we are using $dv''_C$ as a length in velocity space, the negative sign is not significant and may be dropped. We may also write $I_{BC}$ and $\sigma_{AB}$ in terms of the molecular parameters by using the hard-sphere scattering relations:

$$\sigma_{AB} = \pi d_{AB}^2. \tag{52}$$

And:

$$I_{BC} = d_{BC}^2/4. \tag{53}$$

Substituting all of these results into equation (49) and simplifying gives the SIM equation for the flux:

$$F_C = N_A v_A \, d_{AB}^2 \, d_{BC}^2 \, I/32\pi \, r_{BC}^2 \, R v_C''^2 \tag{54}$$

where $I$ requires numerical integration.

The SIM flux equation has several interesting characteristics. For instance, while the B-C mutual diameter $d_{BC}$ is found in the integral and thus effects the relative intensity distribution, $d_{AB}$ enters only as a multiplicative constant. This fact reflects a subtle approximation in the method. We have implicitly assumed the applicability of the hard-sphere differential cross-section, which is a constant at all scattering angles. This cross-section, however, is accurate only at infinite distance. Each collision partner sweeps out a cylindrical shadow zone, directly "behind" it, into which its partner cannot be scattered. At infinite distance from the collision, this cylinder subtends zero solid angle, but at the moderate distances involved in the SIM the

shadows are of significant size. When we test the SIM, we will be in part testing the reasonableness of this approximation.

It is also worthy of note that the SIM equations, again excepting multiplicative constants, do not depend on the beam velocity $v_A$ or the masses A, B or C. This means that the relative magnitude of $F_C$, with $v''_C$ expressed in units of R, is independent of the beam energy and the reactant masses. This result is surprising to our intuition, and while it should not be overstated, neither should it be undervalued. The masses do, of course, enter explicitly into the momentum conservation relations which allow construction of the AB from the C product distribution. Both the masses and the beam energy are used to locate the stability circles dividing bound from unbound AB product, and thus determining the observed reactive scattering. Thus, the insensitivity of $F_C$ to mass and energy results both from our focus on the C product and from our normalization of $v''_C$ to the mass-dependent quantity R. Nevertheless, the SIM allows us to visualize the reactive collision process in terms independent of the two most obvious collision variables. If the model is accurate, this insight may prove to be not insignificant. We shall be particularly interested in the dependence of $F_C$ on $d_{AB}$, $v_A$, and the masses as we test the Sequential Impulse Model.

Finally, we should note the behavior of equation (54) at some limits of interest. As $v''_C$ approaches zero, the coefficient grows without limit, while the integration limits

on $I$ become undefined. Scattering at $v_C'' = 0$, representing spectator stripping, occurs when B does not interact with C, and thus is not properly described by the arguments we have used. The integration limits on $I$ become identical when $\varepsilon = 0$, corresponding to scattering on the centerline: the flux there is thus zero. This is because there is only one $\chi_{AB} - \chi_{BC}$ combination leading to scattering on the centerline, while there are many for other values of $\varepsilon$. As a result, centerline scattering has zero relative probability.

D. Preliminary Application to the Experimental System

Let us now compare the Carom and Sequential Impulse Models with each other and with experiment. To evaluate the SIM flux equation we used a computer program, written in FORTRAN IV for the LBL CDC 7600 computer and designated SIMPLOT. A listing of SIMPLOT comprises Appendix B. The program first establishes a grid of points spanning the limiting cardioid, each representing a possible value of $\vec{v}_C''$. Equation (54) is then evaluated at each grid point. The integral is evaluated numerically, using the form of equation (37), which appears to be smoother than equation (45). The integration routine is an adaptive Simpson's Law program supplied by the Lawrence Berkeley Laboratory Computer Center.[5] It was set to meet a relative error bound of .001. Since only relative intensities are of interest, the multiplicative factors of equation (54) are omitted, and a constant factor of $10^3$ is introduced to produce output intensities on the

same order of magnitude as our arbitrary experimental units. The hydrogen atom radii were taken to be 0.25 Å, a value appropriate to relative energies around 8 eV. The internuclear axis $r_{BC}$ was taken as the equilibrium value of 0.74 Å. As discussed in the previous section, the A atom radius does not effect the relative results.

After the value of F was obtained for each grid point, five plots were produced showing the results. The first displays the $v''_C$ intensity contours in LAB velocity space, in units of R. The other four show the AB product intensities in units of $u_A$, for each of the four mass combinations possible when A = 14 and B, C = 1 or 2. These plots are wholly comparable to our experimental plots for the same mass system. The five SIM maps are reproduced in Figures V-7 through V-11.

In Figure 7, the large cross represents the LAB origin, while the arrow to the right marks the position of the $2\vec{R}$ vector, which is parallel to $\vec{v}_A$. The shape of the limiting cardioid is evident in the configuration of the outer contour line. The contours are interrupted crossing the centerline due to the singularity there, referred to in the previous section. In Figures 8 through 11, the cross is the CM origin for the reacting system, and the x shows either $\vec{u}_A/2$ or $\vec{u}_A/3$, as marked. In each case, the small square represents the grid size for the $v''_C$ evaluation. As previously mentioned, the position of the stability circle dividing bound from unbound AB product depends on the beam

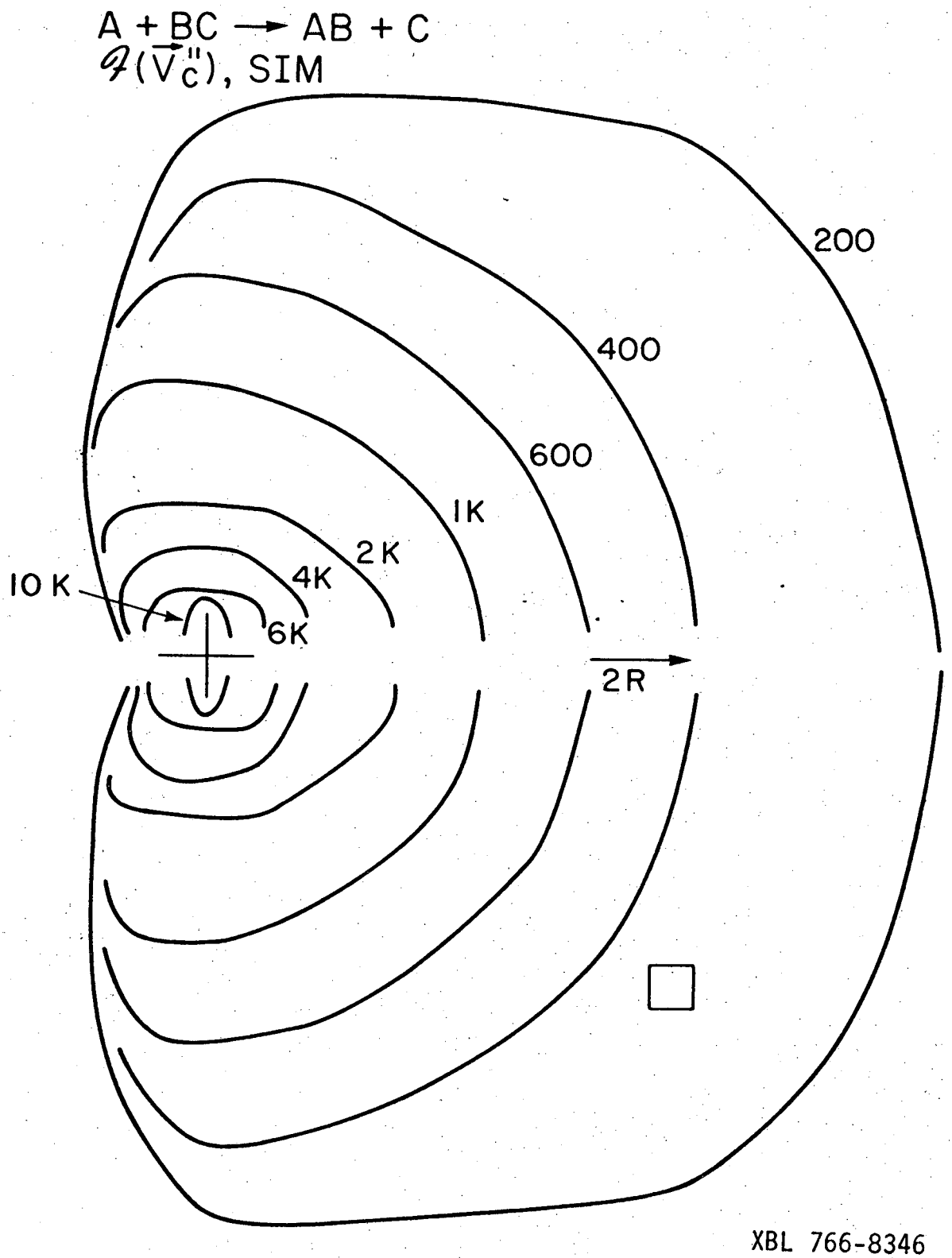


Figure V-7. The SIM solution for $F(v_C'')$.

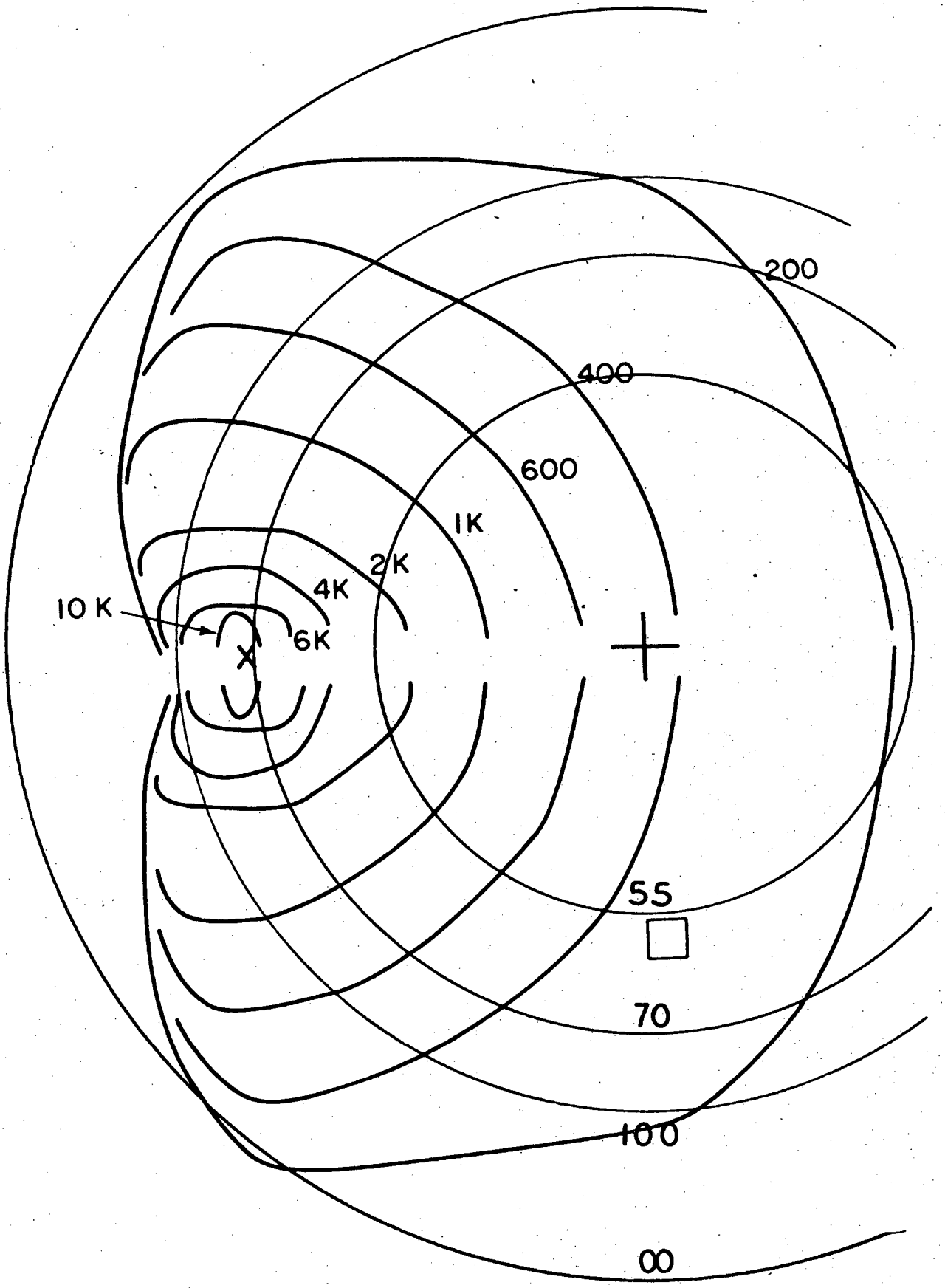


XBL 766-8472

Figure V-8. $F(\vec{U}''_{AB})$ for $N^+ + H_2 \rightarrow NH^+ + H$: + = centroid, x = $\frac{1}{2}\vec{U}_A$.

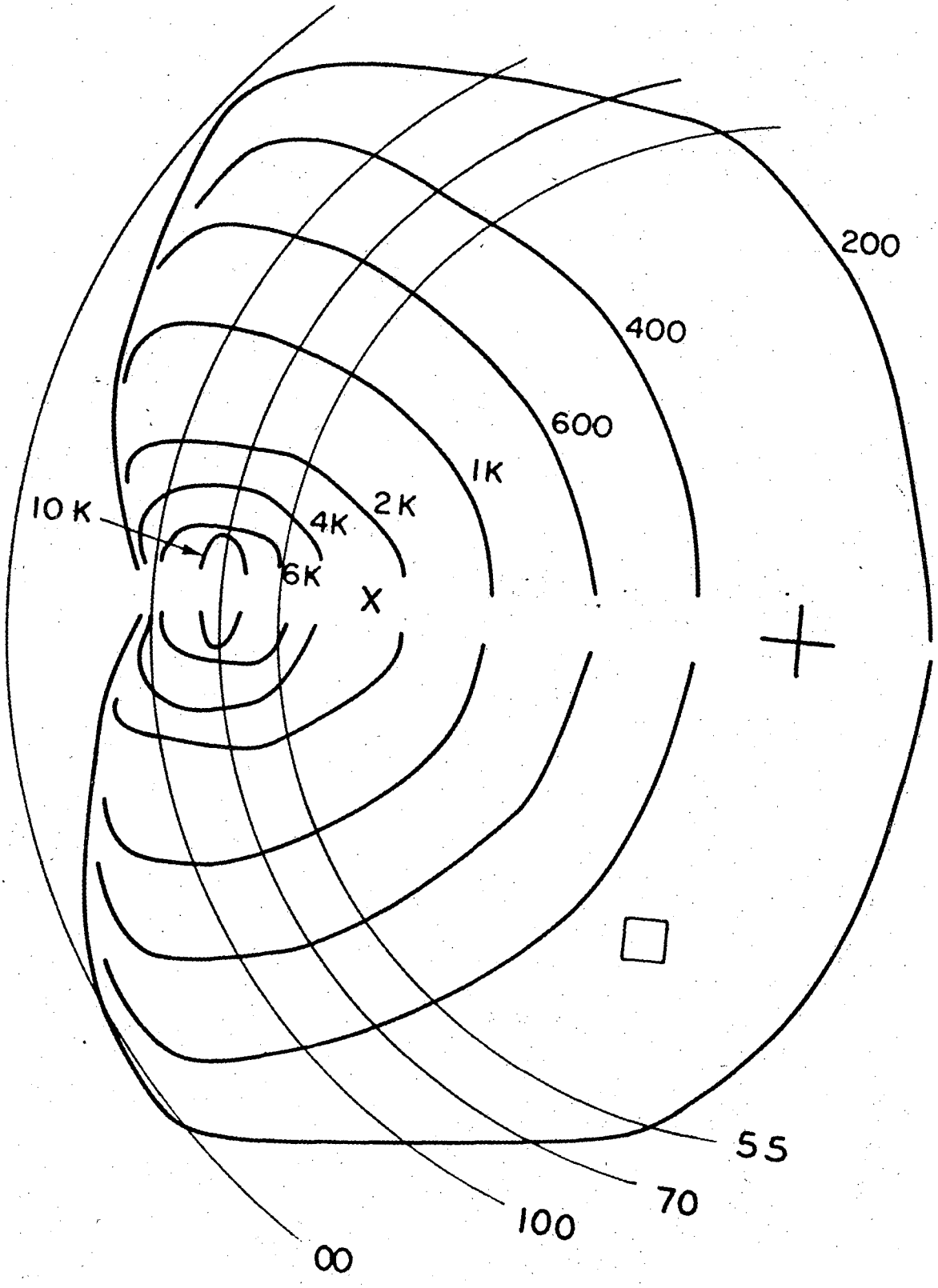


Figure V-9. $F(\vec{U}''_{AB})$ for $N^+ + HD \rightarrow NH^+ + D$: $x = \frac{1}{2}\vec{U}_A$. XBL 766-8471

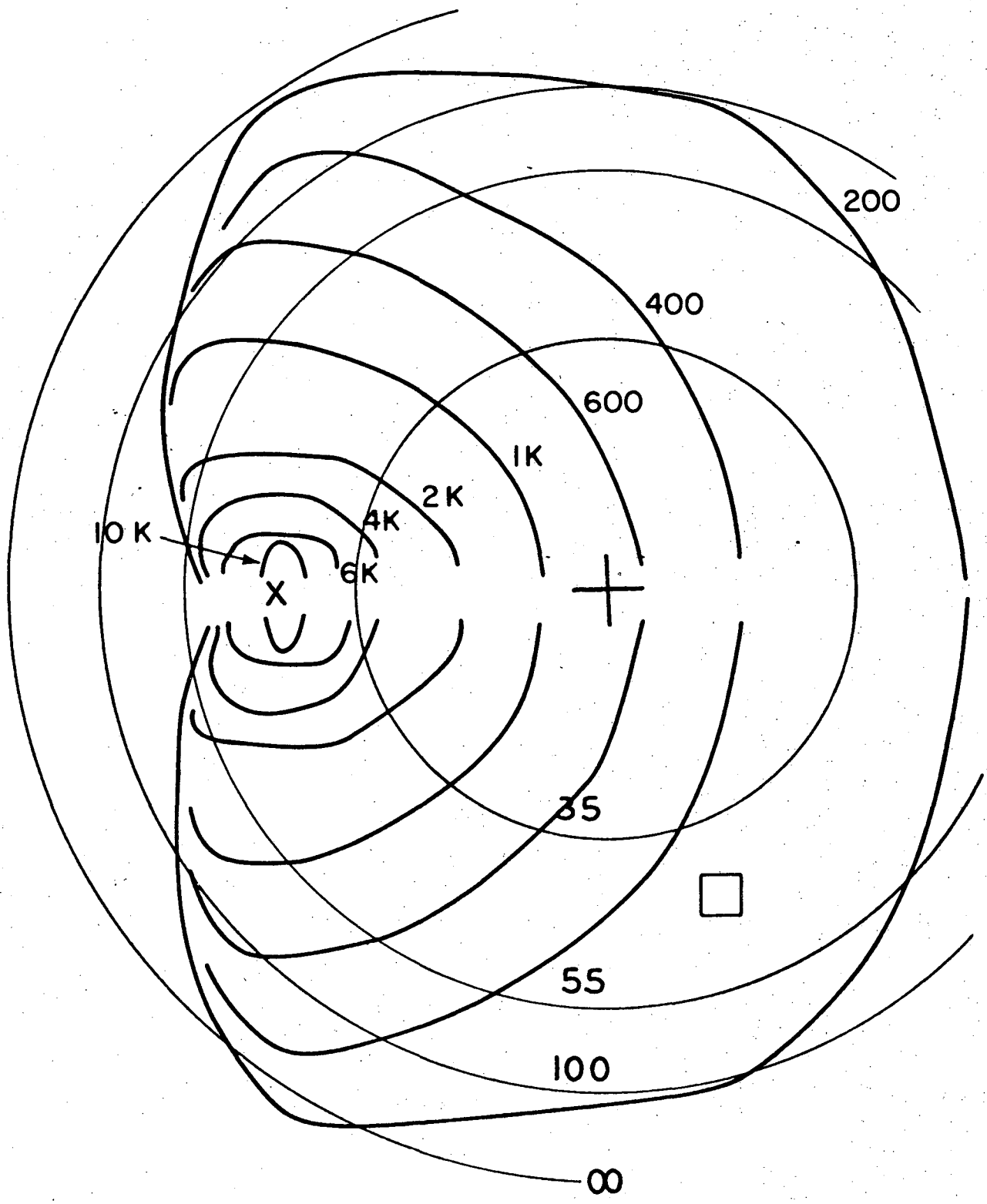


XBL 766-8473

Figure V-10. $F(\vec{U}''_{AB})$ for $N^+ + HD \rightarrow ND^+ + H$: $x = \frac{1}{3}\vec{U}_A$.

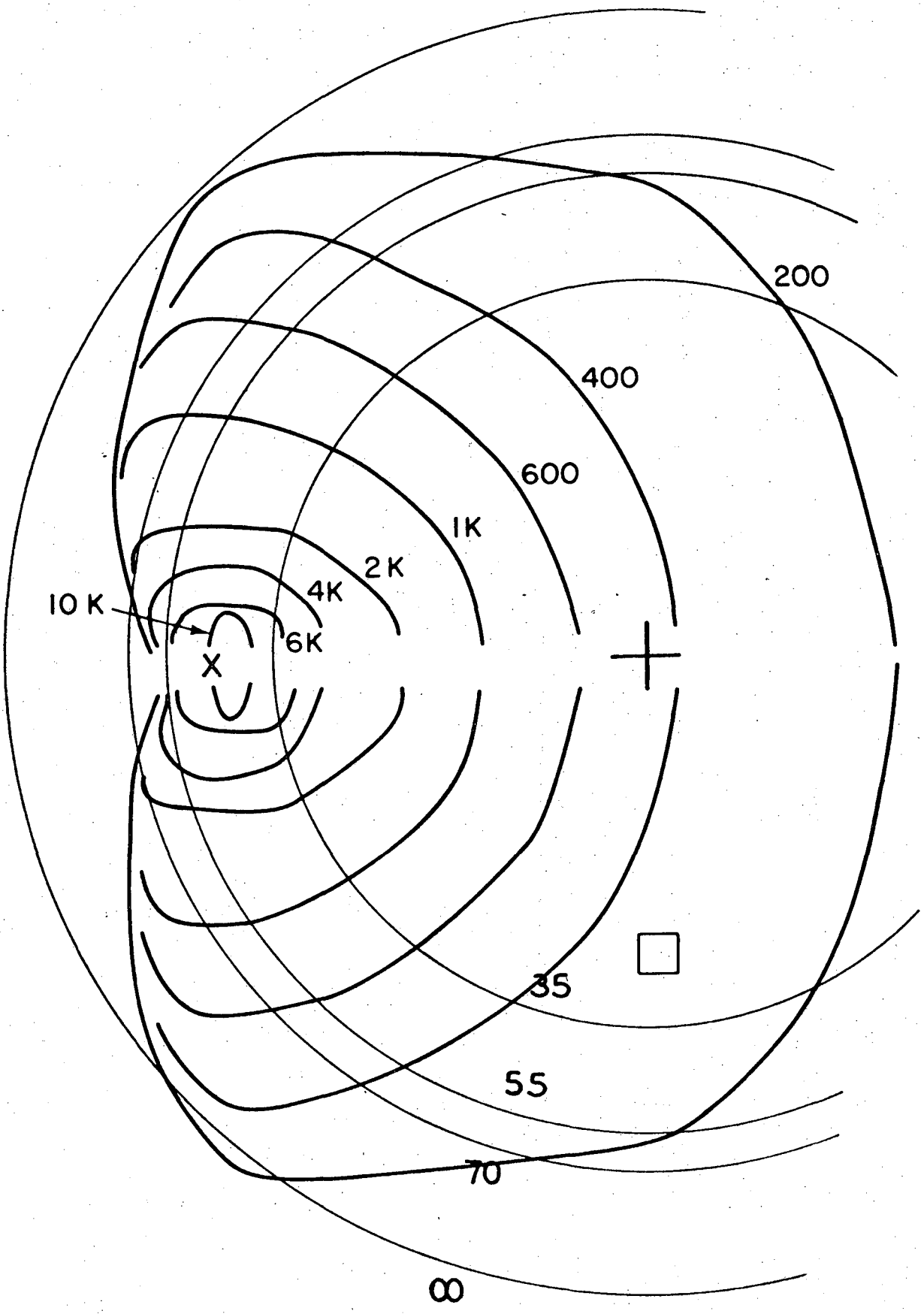


XBL 766-8474

Figure V-11. $F(\vec{U}''_{AB})$ for $N^+ + D_2 \rightarrow ND^+ + D$: $x = \frac{1}{2} U_A$.

energy. The radii of these circles is one of the outputs of the SIMPLOT program. Figures 8 through 11 display the stability limits for the designated mass combinations at several experimentally significant energies. The circle marked "$\infty$" is the Q = 0 circle and thus marks the outer boundary at which any product may be formed.

To predict experimental product distributions from the SIM, we take the appropriate one of Figures 8 through 11, and find the stability circle corresponding to the experimental energy. All product intensity outside of this circle is bound according to the SIM assumption, and the $F(v''_{AB})$ distribution lying outside the circle should represent the experimentally observed map. We may use this method to predict the angle of maximum product intensity as a function of beam energy. These predictions are shown graphically in Figure 12. The abscissa again represents the impulsive relative energy $E_A(A/A+B)$.

Since the Carom Model is essentially a statistical solution of the SIM problem, the predictions of the two should coincide. To test this equivalence, a modification of the BALLS program was prepared and christened NEWBALL. The atomic and molecular radii were taken equal to those of SIMPLOT. Here the A atom radius is also required, and was initially taken as 0.48 Å.

The BALLS program produces predictions for four laboratory energies which were fixed by Winn at 100, 150, 200, and 250 eV. To fit more closely the energy range of our

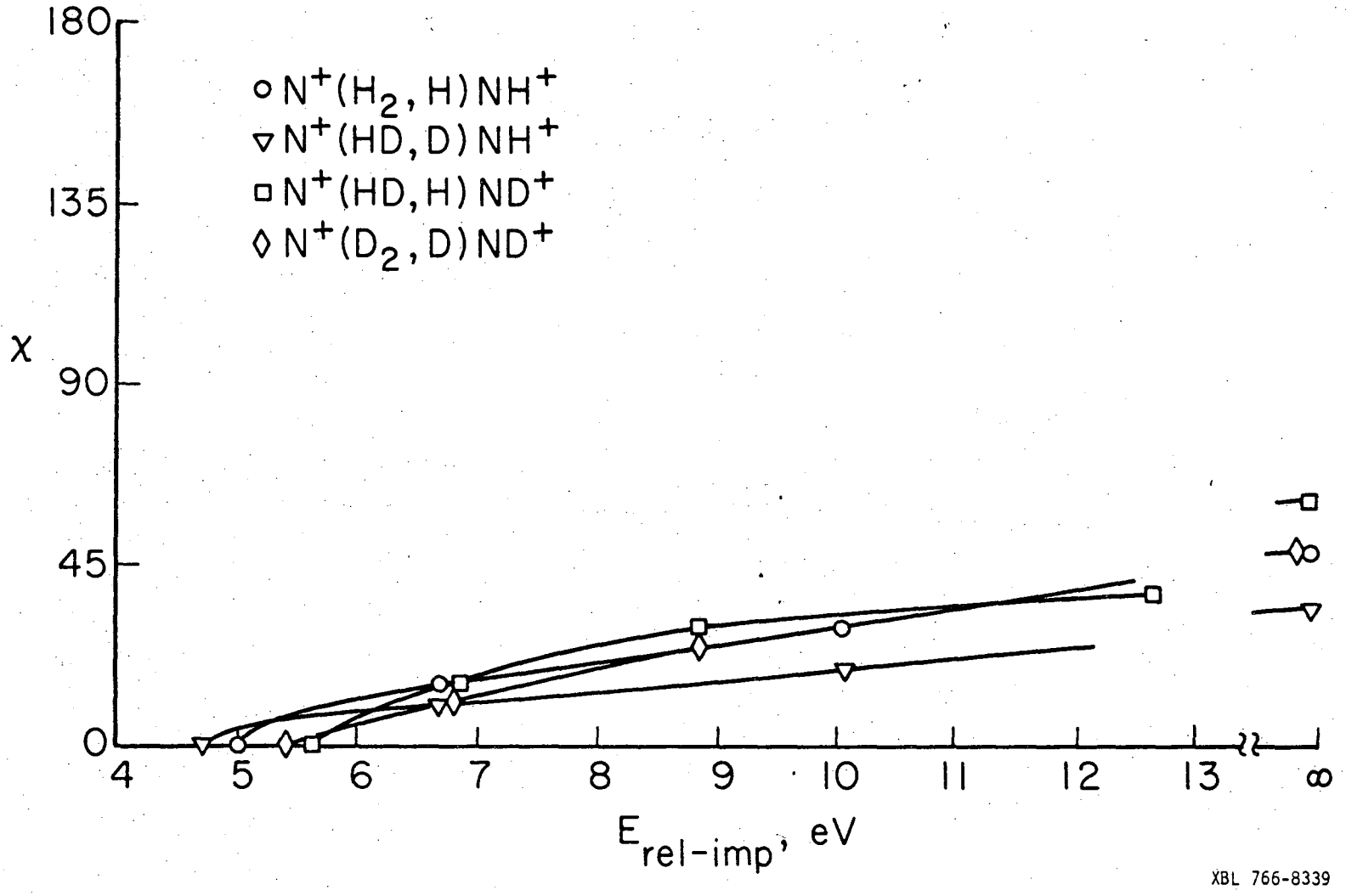


Figure V-12. Peak intensity angle as predicted by the S.I.M.

experiments, they were changed to 70, 100, 150, and 250 eV, with an assumed dissociation energy of 4.6 eV. A subroutine was written to evaluate $v_C''$ explicitly for each trajectory. Another subroutine collected the $v_C''$ predictions into bins according to two separate methods.

Both collections employ a grid in velocity space identical to that in SIMPLOT, and construct a bin centered on each grid point. The in-plane collection simply counts each event into the bin and within 2° of the detector plane. The all-space collection system collected all events of the proper $\varepsilon$ and $v_C''$, regardless of inclination to the detector plane. The events were then weighted by $(v_C'' \sin^{-1})$. This method in effect expands the bins into annular rings about the $\vec{v}_A$ vector, and weights the collection by the relative volume of the ring. The advantage is that all scattered intensity is collected into some bin: the effect is identical to choosing more values of the azimuthal angle $\Theta$ in the initial conditions. No statistical discrepancy arises, since all values of $\Theta$ are equally probable.

After preliminary results were obtained, a few additional modifications were found necessary in NEWBALL. The in-plane collection method failed to produce statistically significant product intensity, and even the all-space method left many unpopulated bins. The bin size was thus multiplied by nine by collecting a three-by-three square array of bins into the center one. A multiplicative constant of $10^4$ was introduced to produce values similar in magnitude to the SIM and experimental results. At the lower collision

velocities examined, numerous trajectories produced both AB and AC bound product. These trajectories were assumed to produce AB product, on the grounds that in the overwhelming number of instances A and B reapproach before A and C.

The output of NEWBALL was converted into CM plots of product intensity analogous to the experimental and SIMPLOT output. The results are shown in Figure V-13. The effect of the enlarged bin size is obvious; the actual collected amplitudes are shown in the lower hemisphere. Figure V-13 may be compared with Figure V-7, with one technical proviso. Strictly speaking, the figures are not fully equivalent: Figure V-6 shows value of $F_C$ at the grid points. Figure V-13 shows $F_C$ integrated over the volume surrounding the grid point, i.e., $\int F d^3v''_C$. As long as the surfaces are reasonably smooth, the difference should remain only nominal.

The similarity in the figures is most reassuring. Within the accuracy of the grid size, they appear identical. Figure V-14 shows the Carom Model predictions for peak angle as a function of impulsive relative energy, and corresponds to Figure V-12. Even though Figure V-14 includes both AB and AC product, the predictions are quite similar. Also of interest is the Carom Model dependence on mass and on $d_{AB}$, predicted by the SIM to be zero. By presenting only one plot of C product intensity for the Carom model, we have implicitly answered the former question, for both BALLS and NEWBALL present separate results for each of the four mass combinations. With the exception of a single trajectory in

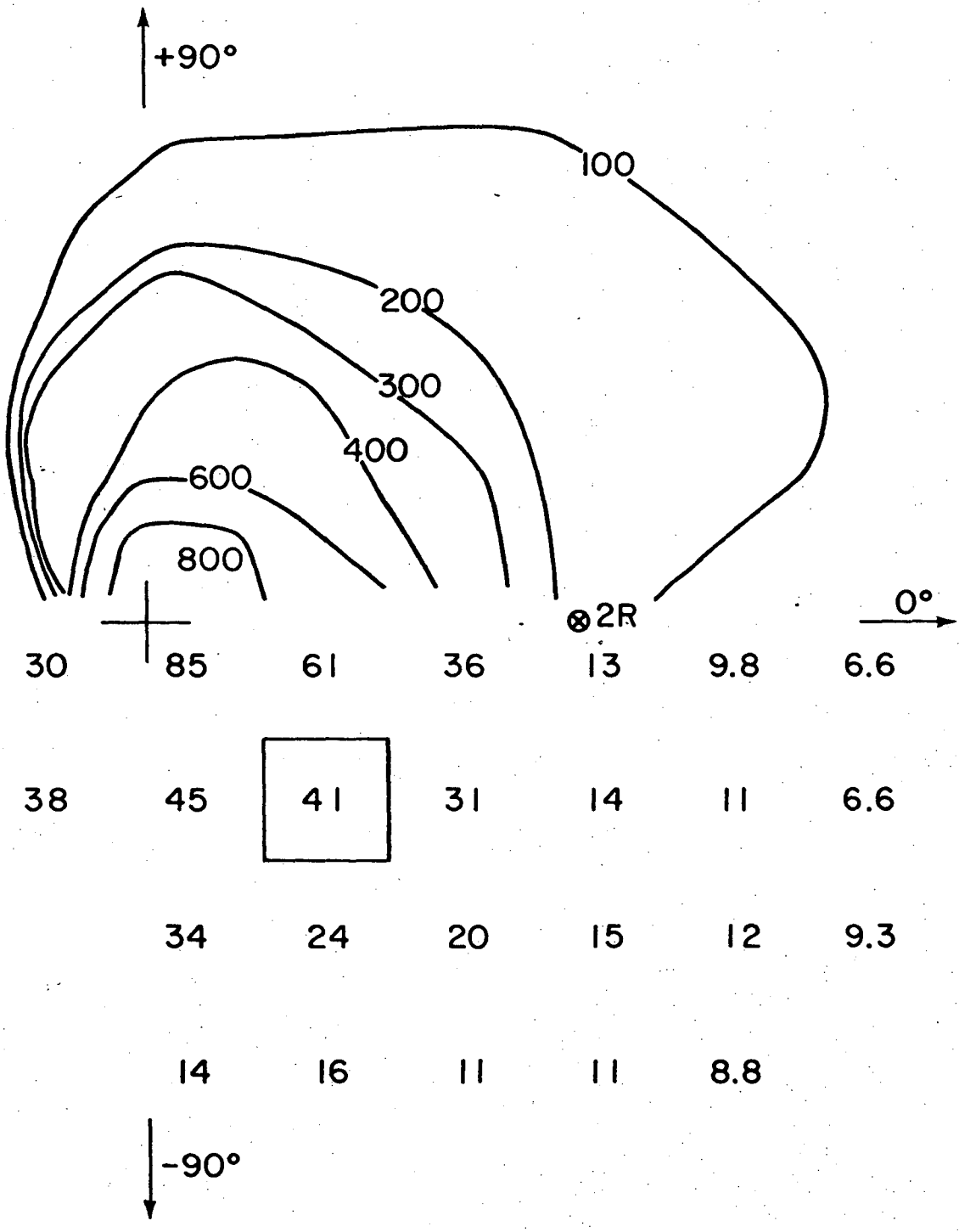


CAROM MODEL: $V_e''$ LAB VELOCITY DISTRIBUTION, OVER ALL SPACE

XBL 766-8348

Figure V-13. Carom model prediction for $F(v_C'')$.

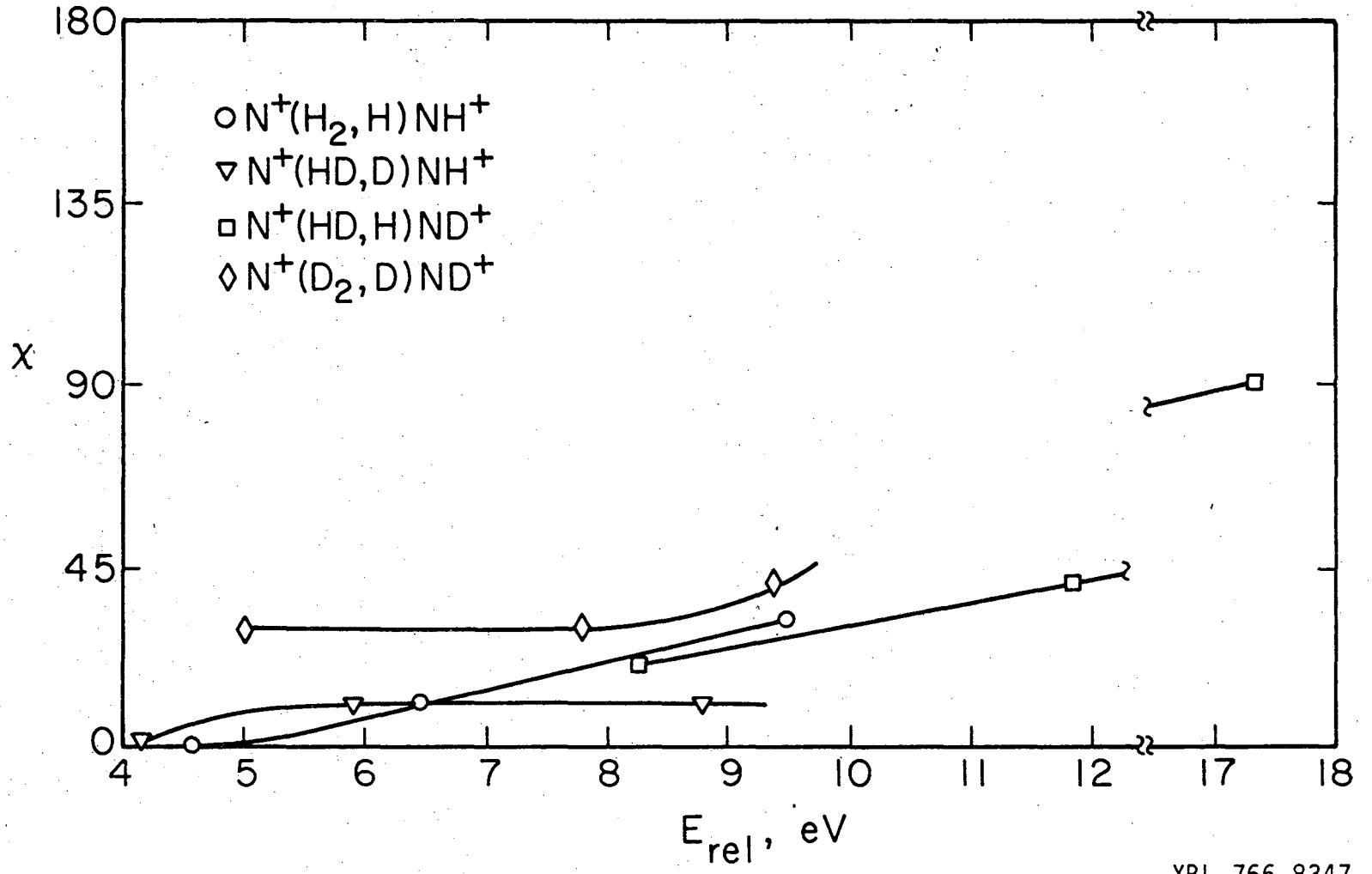


XBL 766-8347

Figure V-14. Peak intensity angle predicted by the Carom model, including AC product.

Lacking in

Pagination Only

the $H_2$ case, the four results were completely identical. The degree of similarity is both surprising and convincing: the single exception provides a welcome reassurance that the identity does not arise from a programming error. As a test of the sensitivity of $d_{AB}$, NEWBALL runs were made with two extreme values of the mutual radius: $d_{AB} = r_{BC}$ and $d_{AB} = d_{BC}$. Within the expected multiplicative constant, the C product distributions were essentially identical. Both of the unexpected predictions of the SIM are therefore supported by the trajectory results.

This agreement between theoretical models is gratifying, but does not guarantee the correspondence of either model to uncompromising reality. For this confirmation, we must compare the theoretical and experimental results. In overall appearance the SIM plots, Figures 8 through 11, are indeed similar to the experimental maps in Chapter V. Stripping predominates in the region where the product is stable; at higher energies, the intensity peaks move to larger angles. The angles are isotope-dependent and not highly energy-dependent. For a quantitative comparison, we may examine Figure V-12 and its experimental equivalent, Figure IV-16. For the two reactions producing $NH^+$ product, the results are quite similar. For $ND^+$ product, however, there is a disturbing discrepancy. While the SIM predicts a peak angle below 90°, the experimental maximum lies at 180° at all higher energies. The partial success of the model argues that it contains a profitable measure of truth,

but the partial failure indicates that further refinements are necessary.

However, before proceeding to the modification of our hypothesis, we should consider a plausible alternative version of the Sequential Impulse Model. Thus far, we have assumed that the incident ion must react with the atom B which it originally struck. However, it is natural to ask whether it may react instead with atom C. We shall call this alternative the "wrong-atom" version of the SIM. This problem involves the final B atom vector, $v''_B$, in the same manner that the "right-atom" case concentrated on the $v''_C$ vector. In general, the probability weighting of this vector presents a considerably more complex situation mathematically, and a solution has not yet been found. However, some of the characteristics of the problem have been determined, which may allow us to judge the plausibility of the wrong-atom mechanism. These results will merely be stated here; Appendix A contains the mathematical details.

For homonuclear targets, the right- and wrong-atom versions turn out to be equivalent. We may therefore focus on the heteronuclear cases. These are profitably discussed using the factor $\eta$, where $\eta = C/B$. The magic circle in the heteronuclear case is no longer given by the intersection of the centroid sphere with a plane. Instead, the centroid sphere intersects a second sphere of radius:

$$\rho = \left|\frac{\eta v''_B}{1-\eta^2}\right| \qquad (55)$$

centered on the point:

$$\vec{d} = \vec{v}''_B/(1-\eta^2) \tag{56}$$

which lies on the extension of the vector $v''_B$. The limiting cardioid for this case is the equality of the expression:

$$v''_B \leq 2R(\cos\varepsilon+\eta). \tag{57}$$

In order to perceive the experimental implications of the wrong-atom case, we must shift our perspective somewhat. So far, we have focused on the mechanism, defining B as the struck and C as the unstruck (by the ion) atom. Experimentally, however, we observe all product of a given mass, which may originate in either mechanism. Therefore, let us designate by $B^*$ and $C^*$ the reacting and non-reacting atoms respectively. The right-atom case then corresponds to:

$$B = B^* \qquad C = C^* \tag{58}$$

while, for the wrong-atom mechanism:

$$C = B^* \qquad B = C^*. \tag{59}$$

The vector of interest becomes the $v''_{C^*}$ vector in each case. The right-atom cardioid from equation (17) is thus:

$$v''_{C^*} = 2R(\cos\varepsilon+1) \tag{60}$$

and the wrong-atom equivalent is:

$$v''_{C^*} = 2R^*(\cos\varepsilon+B^*/C^*). \tag{61}$$

Here $R^*$ is the wrong-atom value of R in terms of B and C. Converting it to a function of $B^*$ and $C^*$ results in:

$$R^* = \frac{C^*}{C^*+B^*} \frac{A}{A+C^*} \quad \frac{C^*}{B^*} \frac{A+B^*}{A+C^*} R. \tag{62}$$

And therefore the limiting wrong-atom cardioid, in $B^*$-$C^*$ terms, is:

$$v''_{C^*} = 2 \frac{A+B^*}{A+C^*} R\left(\frac{C^*}{B^*} \cos\varepsilon+1\right). \tag{63}$$

The right- and wrong-atom cardioids, for both mass combinations, are shown in units of R in Figure V-15. We observe, in each case, regions where the right-atom product is forbidden, while wrong-atom product is allowed. For $NH^+$ product, these are at CM angles near 90° and greater; for $ND^+$ product, at small angles and forward of the stripping location. If the wrong-atom mechanism contributes significantly to the scattering pattern, it is here that we should expect to observe the product most clearly.

The wrong-atom results should be reflected in the BALLS program output, since that is a trajectory solution of the SIM problem. Histograms presenting the angular product distribution predicted by BALLS, for a 250 eV LAB ion energy, are presented in Figure 16. Each bar represents the relative intensity of stable AB* product scattered into a 10° angular range of X. The lower, shaded area is the right-atom component and the upper, blank portion the wrong-atom component. The results agree with what we expect from the limiting cardioids. In the homonuclear cases, the wrong- and right-atom

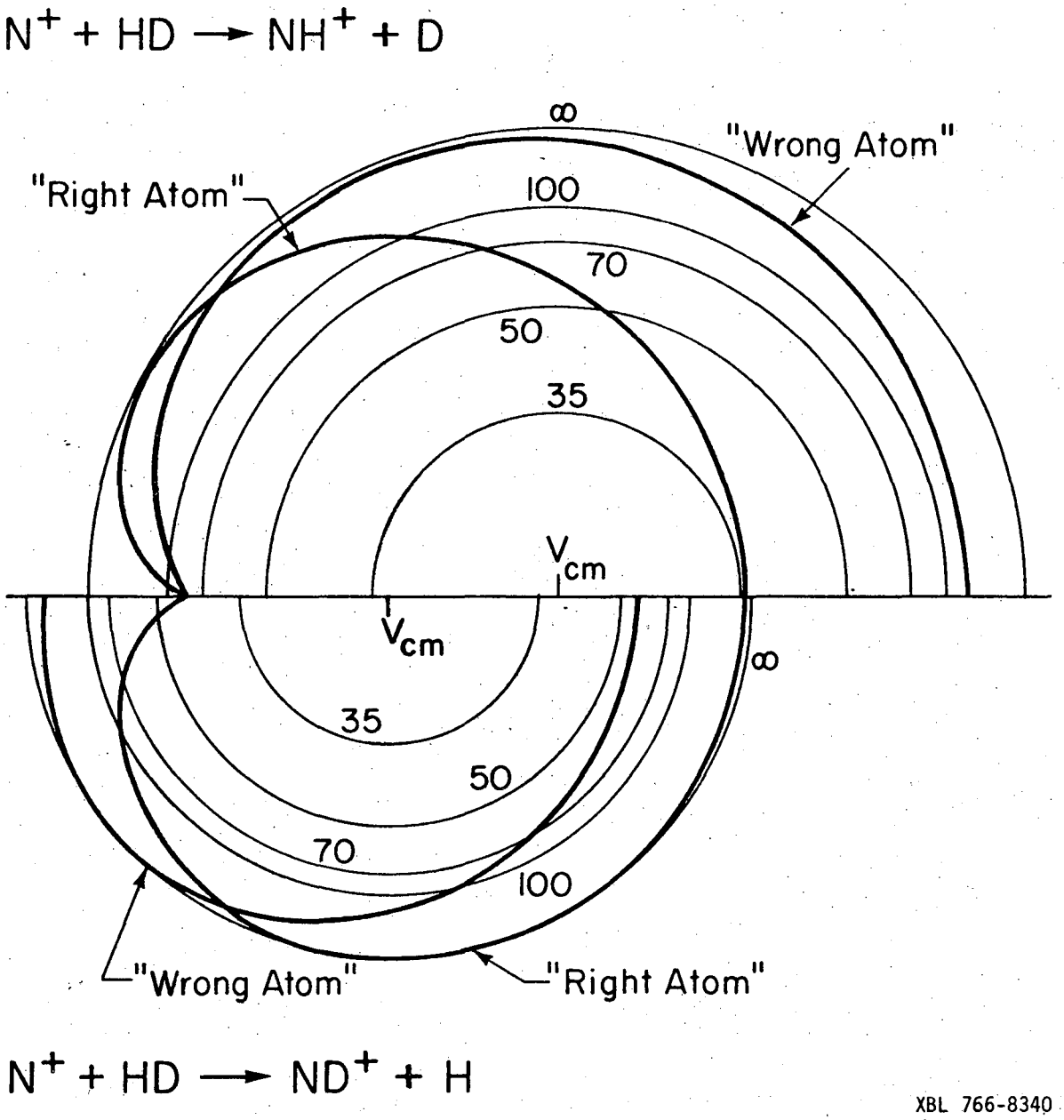


XBL 766-8340

Figure V-15. Limiting cardiods for heteronuclear "Right-" and "Wrong-atom" cases.

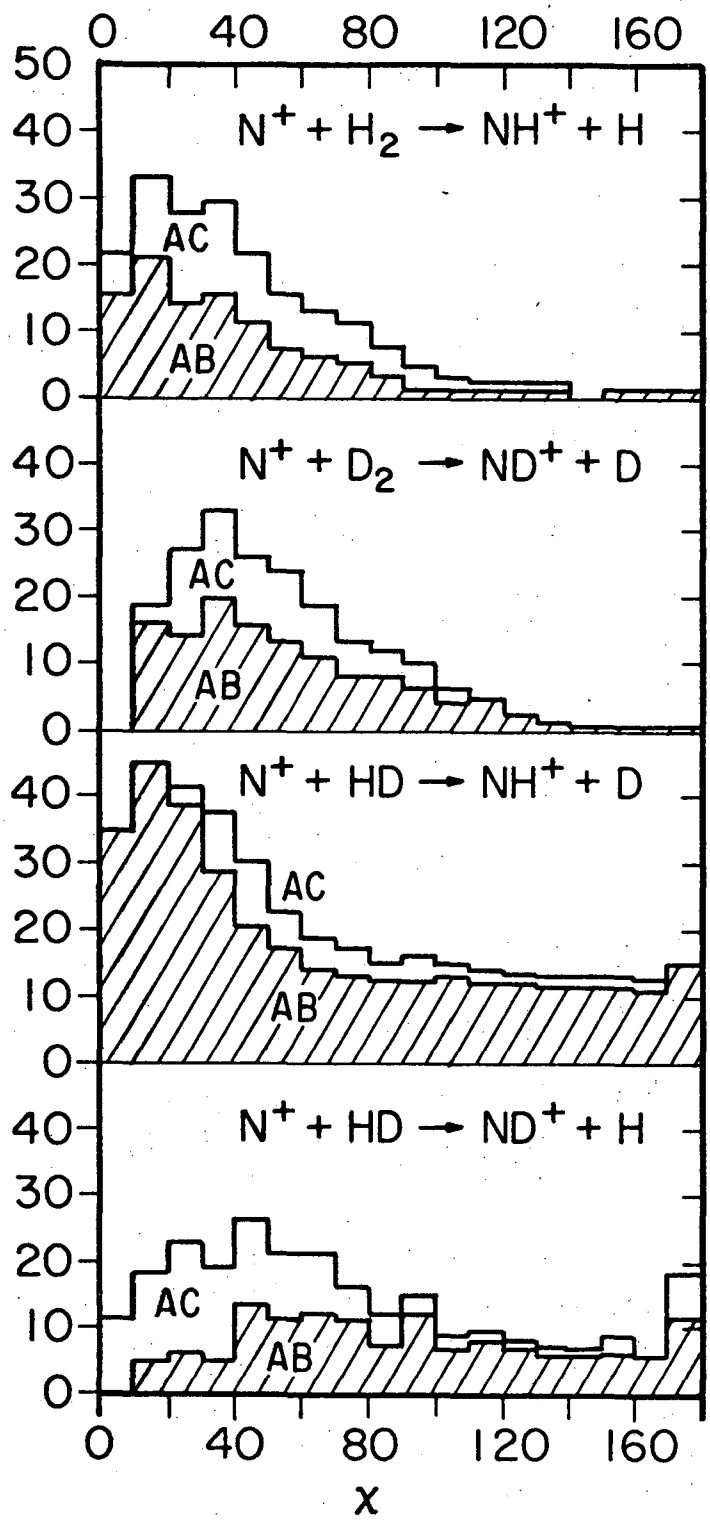


XBL 766-8343

Figure V-16. Angular distribution bins from the Carom Model, showing AB and AC product.

contributions appear to be proportional across the angular range. For $NH^+$ product, the wrong-atom component is concentrated at larger angles, and for $ND^+$ product, at smaller angles. In general, the wrong-atom component is of considerable, though somewhat lesser intensity. It does not significantly change the predicted angle of peak intensity, but it does noticeably, influence the shape of the distribution.

Examination of the experimental data does not reveal any effect from the wrong-atom alternative mechanism. We observe neither large-angle $NH^+$ scattering or small-angle, high velocity $ND^+$ product at higher energies. Instead, the experimental distributions more closely resemble the right-atom SIM distributions of Figures V-7 - V-11 and the right-atom part of the BALLS histograms. The exception, the $ND^+$ scattering, is more intense than expected at large, instead of small, CM angles. Based on what we know of the wrong-atom mechanism, then, it appears likely that it does not contribute significantly to the observed scattering. This fact is not extremely surprising. Our dissociation energy criterion for determining reactive events is clearly extremely simplified: proximity, as well as relative energy, should determine the reactivity of an atom pair. It appears reasonable that the struck atom will be closer to the incident ion than the unstruck atom for a good part of the time span of the reaction, and it is thus also reasonable that the struck atom contributes more reactive product.

## E. Refinement of the Model

Having examined the wrong-atom version of the Sequential Impulse Model, and found it of limited experimental influence in our system, we may concentrate henceforth on the right-atom variant. The Sequential Impulse Model is a hard-sphere model operating freely in three dimensions. It should thus be most effective when the potential surface for the reaction is essentially flat. By concentrating on the SIM we have been implicitly restricting our attention to events likely to occur on the $^3A_2$ - $^3\Pi$ surface of Figure III-1. There is, however, another surface connecting reactants and products, and that is the $^3B_2$ - $^3\Sigma^-$ surface. Perhaps by considering events which are more likely on this surface we can bring our model into better accordance with experiment.

This surface is also essentially flat in the area representing collinear approach. For perpendicular approach, however, there is a barrier of around an electron volt on the surface, leading to the avoided crossing with the $^3B_1$ component of the $N(^2D) + H_2^+$ surface. The barrier will discourage perpendicular approach on this surface in any case. If the avoided crossing is a significant contributor to charge exchange, as suggested in Section A of this chapter, most perpendicular approaches will be removed from the surface entirely. In any event, we may expect nearly collinear events to dominate the $^3B_1$ - $^3\Sigma^-$ surface.

Collinear events on an impulsive surface are predicted by the skewed coordinate method of Section B. Application of this method to the nitrogen system may thus be enlightening. First, however, let us collect in tabular form the experimental data which a successful collinear model must predict. Collinear events necessarily produce product at 180° in the CM system, for there is no way for the incident ion to "get past" the target molecule in one dimension. Collinear models will thus be concerned with $NH^+$ product scattered directly backward from the centroid. We recall that such a peak is seen in the lower energy work performed by Tsao, and re-examined in our Figure IV-1. We also note that, although there is considerable backscattering at some energies under the SIM, a backwards peak with a maximum at 180° does not appear. In the collinear model, as with all others, there will be some isotope-dependent collision energy E* above which stable product will not be formed. We can test the applicability of the collinear model to the observed back peaks by examining the experimental results for intensity maxima at 180°. If they are present at energies below E*, for each set of reactants and products, and absent above E*, we may place some confidence in the model.

In Table V-II are collected the maximum laboratory energies at which 180° peaks are found, for the three reactions studied. For $H_2$ target, an indefinite rear ridge may be present at 70 eV; certainly the back peak is present below and absent above that energy. For $NH^+$ product from HD target, a backwards peak is never observed, and the upper

Table V-II

Maximum Stability Energies for Collinear Impulsive Collisions

| Isotopic Variant: | $N^+(H_2H)NH^+$ | $N^+(HD,D)NH^+$ | $N^+(HD,H)ND^+$ | $N^+(D_2,D)ND^+$ |
|---|---|---|---|---|
| Value of $\beta$: | 48.81 | 31.26 | 67.62 | 52.13 |
| Value of $E^*$: | | | | |
| Experimental | ~70 | $\lesssim$37 | $\gtrsim$70 | - |
| Square Well, $D_o^o = 4.6$ | 120 | 26 | 173 | 129 |
| Square Well, $D_o^o = 3.7$ | 91 | 19 | 129 | 95 |
| Generalized Attraction, $D_o^o = 3.7$ | 83 | 13.5 | 123 | 91 |
| Localized Attraction, $D_o^o = 3.7$ | 95.2 | 72.8 | 152.4 | 101 |

limit is the lowest energy studied. For $ND^+$ product from HD, backscattering dominates the maps at the highest energy for which detectable intensity remains. In this case, the disappearance of the peak may be due to the decreasing cross-section for reaction, and E* may lie at still higher energies.

Now we apply the skewed coordinates technique to predict E* values from theory. The experimental reactant molecules are overwhelmingly in the ground state, and it is thus proper as well as convenient to assume zero initial vibrational energy. As a first approximation, we shall ignore the slight exothermicity of the reaction and use the simple square-well potential of Figure V-1. When $\theta$ is zero, the angle $\theta'$ is given by:

$$|\theta'| = \Pi - 3\beta. \tag{64}$$

Each mass combination will correspond to a different value of $\beta$; they are compiled in Table V-II. From this $\beta$ arise differing values of $\theta'$. These in turn yield values for the ratio $E_v/E$ according to an analogue of expression (11). E* is the laboratory energy where:

$$D_o^o = E^*(E_v/E). \tag{65}$$

Using $D_o^o$ equal to 4.6 eV, we obtain the $E^*$ values listed in Table V-II under the designation of "Square Well, $D_o^o = 4.6$."

The agreement with experiment is qualitatively respectable, especially for a crude approximation. If we accept that we are dealing with the $^3\Sigma^-$ surface, we can make some

immediate refinements. The first is to realize that reaction on this surface produces $^4\Sigma^-$ product, which dissociates, not to $N^+(^3P)$ + H with a $D_o^o$ of 4.6 eV, but to $N(^4S)$ + $H^+$ with a $D_o^o$ of 3.7 eV. By using this more appropriate value of the dissociation energy in equation (57), we obtain an immediate improvement in the predictions. The new values of E* are listed in the table as "Square Well, $D_o^o$ = 3.7."

More realism is added to the model surface by explicit inclusion of the energetics of the reaction. To begin with, the reaction is about 0.6 eV exothermic. In addition, the correlation diagram, Figure III-1 shows a well in the collinear portion of the $^3\Sigma^-$ surface of about 1 eV, which has been confirmed by theoretical calculations. One way to introduce this fact is to place a 1.6 eV drop in potential energy perpendicular to the entrance channel and a 1 eV rise perpendicular to the exit channel. Such a surface is a combination of the two examples shown in Figure V-3. The E* values resulting from this modification are presented in Table V-II with the label "Generalized Attraction." The effect on the reliability of the predictions is fairly minimal. Several alternative arrangements of energy steps also have little effect.

A significant consequence does result, however, if the 1 eV energy step in the exit channel is placed perpendicular to the $\underline{y}$ axis instead of the x channel. This is not an unreasonable configuration. It implies that the attraction is exerted solely between the B and C atoms, instead of

between C and the AB centroid. Since in a collinear configuration B and C are adjacent, and particularly since they are bound at the outset, such localized attraction is not only possible, but likely. The values of E* consistent with this assumption are on the line of Table V-II marked "Localized Attraction." The effect of this step is to refract all trajectories towards larger angles from the $\underline{y}$ axis, preferentially stabilizing those reactions with small values of $\beta$. The result is a significantly higher value of E* for $NH^+$ product from HD, and a modest increase in the other figures.

It is most likely that the true nature of the product attraction on the collinear surface lies between the two extremes: partly, but not entirely localized. The appropriate value of E* will then lie between the generalized and localized values of Table V-II. These ranges are consistent with experiment. The addition of an adjustable parameter would allow even greater precision in prediction, but such a procedure is hardly justified given the crudity of the model. It is fairer to conclude at this point with the assertion that the collinear impulsive model, with scrupulously reasonable assumptions, reproduces the observed behavior of the 180° product peaks within experimental accuracy. We have now produced two theoretical models of the $N^+ + H_2$ system, each operating on a separate potential surface. The SIM effectively describes the behavior of peaks forward of the centerline, and the collinear impulse

model justifies the peaks in the backward direction. A few additional comments will weld the two components into an integrated structure capable of supporting the full weight of experimental examination. We should first deal explicitly with the status of the collinear impulsive model as a special case of the SIM. The events of the simple square well collinear model are exactly those of the SIM when collinearity is present. The predictions of the collinear model should thus appear in the SIM scattering at 180°. There is zero intensity there in the SIM solely because exactly collinear events have a vanishing probability on a flat potential surface. Only if a mechanism exists on the surface to enhance the probability of nearly collinear collisions will the 180° peak become prominent. The energy barrier to perpendicular approach on the $^3\Sigma^-$ surface, and the probability of charge exchange for trajectories surmounting the barrier, provide that mechanism. They thus constitute an essential link in our argument.

Subject to these considerations, we regard the observed scattering as resulting from the sum of two components. One occurs on the $^3A_2$ - $^3\Pi$ surface, is scattered according to the SIM, and produces product in the $^2\Pi$ state. The other occurs on the collinear part of the $^3B_1$ - $^3\Sigma^-$ surface and produces the $^4\Sigma^-$ state of the product as predicted by the collinear impulse model. For $H_2$ target, both forward and backward scattered product is observed up to about 70 eV; the rear peak then becomes unstable and the forward scattering

dominates the map. For $NH^+$ product from HD, the result is similar, except that the rear component becomes unstable at considerably lower energies. When $ND^+$ product is formed from HD, however, both components remain stable up to considerable energies. Experimentally, the rear component dominates the map at the higher energies, and this dominance must be based on other grounds then stability. However, Figure V-9 reminds us that the expected intensity from the forward-scattering mechanism is low at the predicted high CM angles. In addition, such events result from strongly interactive collisions, which we have inferred to be most conducive to charge exchange from our non-reactive data. Thus charge exchange from the $^3\Pi$ surface to produce $^4S$ product will lower the forward $ND^+$ scattering intensity even further. The result should be weak product intensity somewhat forward of $\chi = 90°$ such as appears in Figures IV-12 and IV-13.

All of our models have provided predictions for all five mass combinations possible when B or C is either H or D. As a result, we are in a position to predict the distribution of $ND^+$ product scattered from $D_2$ target, which we could now observe experimentally. The forward component is predicted by the SIM to be formed near 45°, as shown in Figures V-11 and V-12. Table V-II indicates that the rear peak will be stable at energies up to 100 eV. We therefore expect both forward and back peaks to be prominent in the reaction of $N^+$ with $D_2$.

## F. Summary of Conclusions

This essentially completes our examination of the reaction of nitrogen ion with hydrogen isotopes. It seems proper, however, to summarize our conclusions, stating concisely the most important of the observations which are dispersed through the preceding pages.

Two electronic surfaces are found to dominate the reaction. One of these is the $^3A_2$ - $^3\Pi$ surface, producing $^2\Pi$ product. The distribution of the product is essentially as predicted by the SIM calculations. The other is the $^3B_1$ - $^3\Sigma^-$ surface. Only essentially collinear trajectories proceed to product on this surface. The product is in the $^4\Sigma^-$ state, and behaves consistently with the collinear impulsive model, as adjusted to the expected characteristics of the surface.

Charge exchange becomes the predominant reactive channel at higher energies, resulting from most of the highly interactive collisions. It may occur either from the $^3B_1$ surface to produce $N(^2D)$, or from the $^3\Pi$ surface to produce $N(^4S)$. Charge exchange by the former channel contributes to the collinearity of the reactive scattering on that surface, while exchange by the latter route may explain the low magnitude of forward scattered $ND^+$ from HD target. Both channels are therefore expected to contribute.

A number of predictions arise from these conclusions, which may become testable in future work. Two of these appear to be inevitable if the model proposed here is

substantially correct. For one, the distribution of $ND^+$ product from $D_2$ target should exhibit both a rear peak and two forward lobes at angles near 45°. Secondly, the forward and rear components of each scattering map should be of different states as denoted in the preceding paragraph. Other predictions appear to be probable, but not vital, consequences of our conclusions. The nitrogen product of charge exchange should be of both the $^2D$ and $^4S$ states, and should not show a sharp threshold at 3.3 eV. Reaction (1) probably has an activation barrier of at least 0.7 eV.

As a final note, we may comment on the significance of this work in the larger context of chemical kinetics. It tends to support the general suppositions of Section III-B regarding energy regimes and the effect of exothermicity on product stability. It also shows that a rather complex reactive system, involving extensive portions of two potential surfaces and the probable interaction of two others, can be effectively treated by the use of correlation diagrams and simple hard-sphere models. As a result, it encourages the hope that kinetic theory need not be mathematically impenetrable in order to be effective.

## References

1. For a review of the method and appropriate references, see Bruce H. Mahan, J. Chem. Educ. 51, 308 (1974) and J. Chem. Educ. 51, 377 (1974).

2. John S. Winn, Ph.D. Thesis, University of California LBL Report LBL-1820 (1973), p. 246 ff.

3. Bruce H. Mahan, in Interactions Between Ions and Molecules, P. Ausloos, ed., Plenum, New York (1974), pp. 75-93.

4. Bruce H. Mahan, personal communication.

5. Library SOURCE, subset ASMPSN. See the Computer Center Librarian, Lawrence Radiation Laboratory, Berkeley, CA., 94720 for listing and documentation.

# APPENDIX A

## THE "WRONG-ATOM" SEQUENTIAL IMPULSE MODEL

This appendix examines the "wrong-atom" case of the Sequential Impulse Model, defined in Chapter V, Section D. Figure A-1 shows the appropriate construction for the problem. We observe that the quantity of interest is now the final B-atom velocity, $v''_B$. This will be the only velocity discussed in this appendix, and will be indicated by $\underline{v}$. The quantity $\eta$ is defined as C/B. Three results will be deduced. They are: (1) The identity of the right- and wrong-atom cases for homonuclear targets; (2) The location of the heteronuclear magic circle; (3) The location of the heteronuclear limiting cardioid.

### 1. Homonuclear Case

When $\eta = 1$, the vectors $\underline{b}$ and $\underline{c}$ become of identical length in Figure A-1, and the construction is identical to that of Figure V-4. However, the scattering angle $\chi'$ in Figure A-1 is supplementary to the scattering angle $\chi$ of Figure V-4. Using the properties of supplementary angles, we may write:

$$\sin\chi' = \sin\chi \tag{A1}$$

$$\cos\chi' = -\cos\chi \tag{A2}$$

So that:

$$\cos^2\chi' = \cos^2\chi. \tag{A3}$$

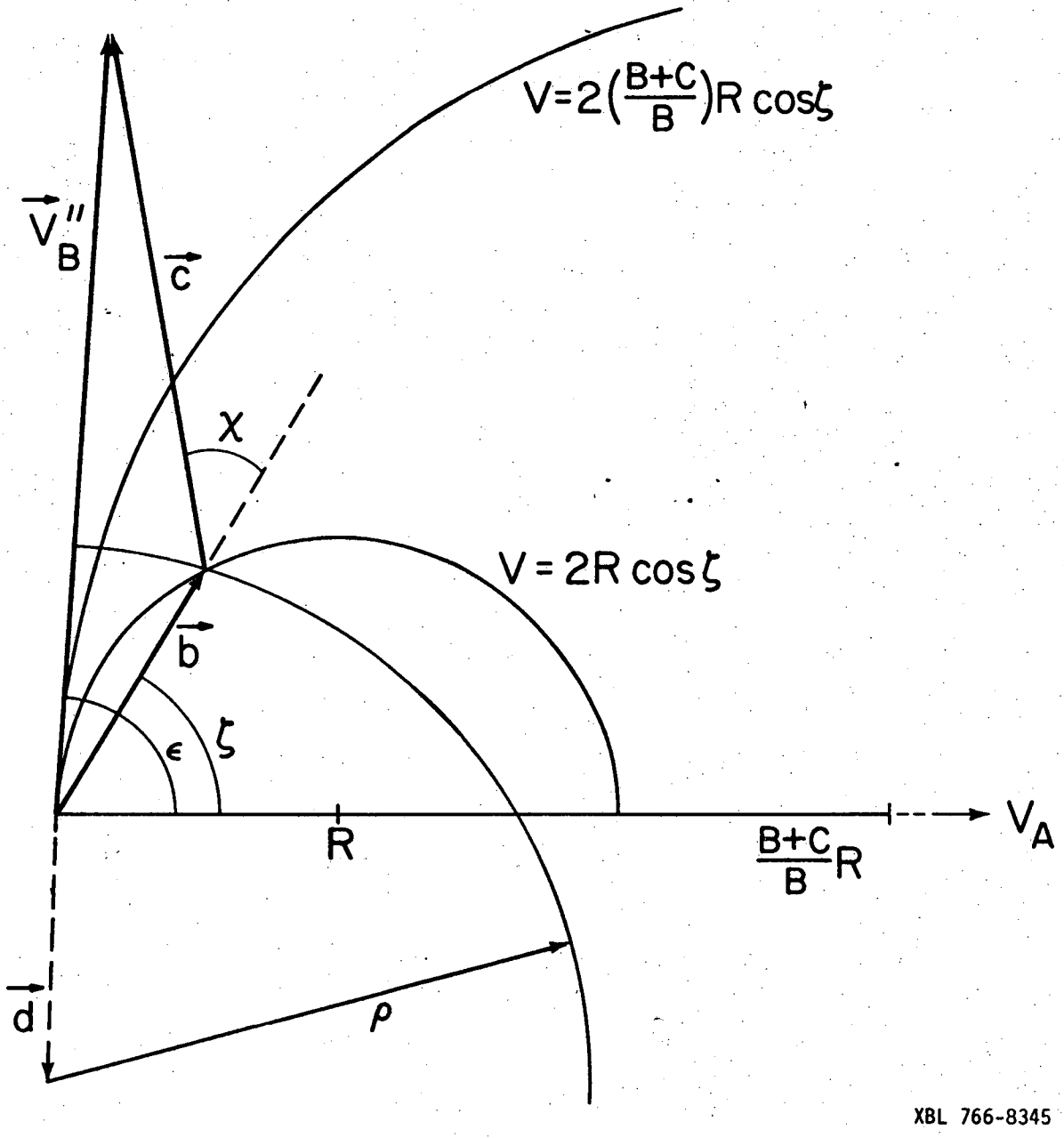


Figure A-1. Relationships pertinent to the "Wrong-atom" SIM.

But $\cos^2\chi'$ and $\sin\chi'$ are the only functions of $\chi'$ required in expression V-(37), and the magic circle and vector relationships are identical. Therefore expression V-(37) and thus the SIM results are invariant to the choice of reacting atom, for the homonuclear case.

2. Magic Circle

Referring to Figure A-1, we may define geometrically the problem of finding the magic circle in the general case. We desire the locus of all vectors $\underline{b}$ and $\underline{c}$ such that:

$$\vec{v} = \vec{b} + \vec{c} \tag{A4}$$

under the constraint:

$$c/b = \eta. \tag{A5}$$

This locus may be shown to be a sphere either by construction or by analytic geometry. We therefore require only the radius $\rho$ and center $\vec{d}$ of the sphere.

Consider the maximum values of $\underline{b}$ and $\underline{c}$, $b_+$ and $c_+$. They will be parallel and thus be related to $\underline{v}$ by:

$$v = |b_+ - c_+|. \tag{A6}$$

Similarly, the minimum values $b_-$ and $c_-$ are related to $\underline{v}$ by:

$$v = |b_- - c_-|. \tag{A7}$$

Since the magic circle is defined by $\underline{v}$, $\underline{v}$ is invariant for a given magic circle. The definition of $\eta$ allows us to remove $\underline{c}$ from equations (A6) and (A7), producing:

$$v = b_+|1-\eta| = b_-|1+\eta|. \tag{A8}$$

But the radius of the sphere of interest is clearly given by:

$$2\rho = b_+ - b_-, \tag{A9}$$

so that $\rho$ is found to be:

$$\rho = \left|\frac{\eta v}{1-\eta^2}\right| . \tag{A10}$$

We may then use $\rho$ to find the center of the sphere, $\vec{d}$, from the relation:

$$\vec{d} = \vec{b} + \rho, \tag{A11}$$

yielding:

$$\vec{d} = \frac{\vec{v}}{1-\eta^2} . \tag{A12}$$

The vector $\underline{d}$ may thus lie on $\underline{v}$ or on its negative extension, depending on the sign of $1-\eta^2$. We note that, when $\eta = 1$, both $\rho$ and $\underline{d}$ are infinite. This is consistent with our statements regarding the homonuclear ($\eta$=1) case in Part 1 of thie appendix. The homonuclear case is equivalent to the right-atom SIM, where the intersecting "circle" is the perpendicular bisector plane of $\underline{v}$. A plane is a "circle" of infinite radius.

3. Limiting Cardioid

Figure A-1 defines coordinate angle $\xi$. We may use this angle to write the Law of Cosines for the $\underline{v}$ - $\underline{b}$ - $\underline{c}$ triangle,

as:

$$(2\frac{B+C}{B}\,R\cos\xi - 2R\cos\xi)^2 = v_2^2 + (2R\cos\xi)^2 - 2v_2(2R\cos\xi)\cos(\varepsilon-\xi). \tag{A13}$$

After straightforward manipulation, this expression may be written as a simple quadratic in $\cos^2\xi$

$$\ell\cos^4\xi + m\cos^2\xi + n = 0 \tag{A14}$$

where:

$$\ell = v^2R^2 + R^4(\alpha^2-2\alpha)^2 + 2vR^3\cos\varepsilon(\alpha^2-2\alpha) \tag{A15a}$$

$$m = -\frac{1}{2}Rv^3\cos\varepsilon - \frac{1}{2}R^2v^2(\alpha^2-2\alpha) - R^2{}^2\sin^2\varepsilon \tag{A15b}$$

$$n = (\frac{v}{2})^4 \tag{A15c}$$

$$\alpha = \frac{B+C}{B} = 1 + \eta. \tag{A15d}$$

If $\xi$ is to be real, the condition:

$$m^2 - 4\,\ell n \geqslant 0 \tag{A16}$$

must hold. Substituting the values of equations (A15) into (A16) gives:

$$(-\frac{1}{2}v^2)^2\,[Rv\cos\varepsilon + R^2(\alpha^2-2\alpha-2\sin^2\varepsilon)]^2 =$$

$$4(\frac{v}{2})^4\,R^2[v^2+2Rv\cos\varepsilon(\alpha^2-2\alpha) + \eta^2(\alpha^2-2\alpha^2)^2] \tag{A17}$$

Collecting terms, removing common factors of $(v/2)^4$, and $R^2$, and converting terms in $\cos^2\varepsilon$ into terms in $\sin^2\varepsilon$, produces:

$$v^2 - 4Rv\cos\varepsilon + 4R^2(\alpha^2-2\alpha^2-\sin^2\varepsilon). \tag{A18}$$

append = 0.

Solving for v:

$$v = \frac{4R\cos\varepsilon \pm [(16R^2)(\cos^2\varepsilon+\sin^2\varepsilon+\alpha^2-2\alpha^2)]^{1/2}}{2} \qquad (A19)$$

which reduces to:

$$v = 2R(\cos\varepsilon \pm (\alpha^2-2\alpha+1)^{1/2}) \qquad (A20)$$

or, since $\alpha = (B+C)/B$:

$$v = 2R(\cos\varepsilon \pm C/B) \qquad (A21)$$

an expression for the limiting cardioid. When $\eta$ is less than unity, choosing the positive root produces a positive $\underline{v}$ for all $\varepsilon$. When $\eta$ is greater than unity, the negative root produces the inner loop of a cardioid which lies completely inside the outer loop produced by the positive root. The positive root is thus chosen.

# APPENDIX B

## LISTING OF PROGRAM SIMPLOT

The following pages contain a complete listing of the program SIMPLOT, used in Chapter V, Section D, of this work to evaluate the results of the Sequential Impulse Model. The program is written in FORTRAN IV for use on the LBL CDC 7600 computer. The main program evaluates the SIM expression at a number of grid points, and then determines the coordinates of the grid and of the stability circles for various mass combinations. The subroutine MAP PLOT performs the actual plotting, with the aid of the subroutine SEARCH. Function ASMPSN carries out the Simpson's Law integration of the SIM integral, using the functional form stored in function FINIG.

```
      PROGRAM SIMPLOT (OUTPUT,PLOT,TAPE9=OUTPUT,TAPE98,TAPE99=PLOT)
      DIMENSION COMMX(2,4), ULIM(4),B(4),C(4)
      DIMENSION BC(4),AB(4),VCORR(4),UCORR(4)
      DIMENSION UX(4,700),UY(4,700)
      EXTERNAL FINTG
      COMMON/INTEG/EL,RHO,DDD,V
      COMMON/MAP ARAY/GX(700),GY(700),TY(700),IZ,TOTPK
      COMMON/DEFINE/VR,VCM
      COMMON/ID/COMMENT(6)
      DATA RZERO,D23,PI,D12,IJ/0.740,0.50,3.141592654,0.73,0/
      DATA A,B,C/14.,1.,1.,2.,2.,1.,2.,1.,2./
      DATA COMMENT/10HSEQ. IMPUL,10HSE MODEL- ,10HC  PRODUCT,10H FROM A
     $+ ,10HBC, UNITS ,10HOF 2RV(0)./
      DATA COMMX/10HNH PRODUCT,10HH2, UNITS ,10HNH PRODUCT,10HHD, UNITS
     $,10HND PRODUCT,10HHD, UNITS ,10HND PRODUCT,10HD2, UNITS /
C         SIMPLOT IS DESIGNED TO PLOT TH EXPECTED PRODUCT DISTRIBUTION
C         FROM MAHANS'S ANALYTICAL SOLUTION OF THE SEQUENTIAL IMPULSE
C         MODEL AS A CONTOUR MAP. THERE IS NO INPUT. OUTPUT CONSISTS OF
C         FOUR MAPS, ONE FOR EACH AB+C COMBINATION, REPRESENTING AB DIST-
C         RIBUTION IN UNITS OF THE BEAM RELATIVE VELOCITY, AND ONE MAP
C         REPRESENTING THE C ATOM DISTRIBUTION, IN UNITS OF BEAM VELOCITY
C         DIVIDED BY TWO R, WHERE R IS MAHANS MASS FACTOR R.
C         THE PROGRAM IS PRESENTLY CONFIGURED FOR N+ + H2,HD,D2. TO CHANGE
C         TO ANOTHER REACTION, VALUES IN THE FIRST TWO DATA STATEMENTS
C         AND THE CAPTIONS IN THE SECOND TWO DATA STATEMENTS MUST BE
C         ALTERED APPROPRIATELY. A,B,AND C ARE MASSES OF REACTANTS IN AMU,
C         D23 AND D12 ARE BC AND AB DIAMETERS, AND RZERO IS THE BC DIAM.
C          ALSO CHANGE THE VALUE OF QSEVERAL STATEMENTS AFTER STMT. 500.
      WRITE(9,1001)
      WRITE(9,1002)
      WRITE(9,1003)
      WRITE(9,1004)
      DDD=D23*D23/(RZERO*RZERO)
```

```
C         THIS LOOP ESTABLISHES USEFUL MASS SUMS FOR THE FOUR REACTANTS.
      DO 110 K=1,4
      BC(K)=B(K)+C(K)
      AB(K)=A+B(K)
C           VCORR AND UCORR CONVERT V(C) TO U(AB).
      UCORR(K)=A*C(K)/(AB(K)*BC(K))
      VCORR(K)=2.*B(K)*(A+BC(K))/(AB(K)*BC(K))
  110 CONTINUE
      DO 100 I=1,24
C         DO LOOP SPANS RANGES OF X ALLOWED TO V3.
      X=-0.4+0.1*I
C         HERE THE MAX VALUE OF Y FOR A GIVEN X ARE COMPUTED.
      RRAD=1.+4.*X
      IF(RRAD) 31,31,32
   32 IF (RRAD-9.) 33,33,34
   33 CMAX=0.5*(SQRT(RRAD)-1.)
      YMAX=(CMAX+1.)*SQRT(1.-CMAX*CMAX)
      IYMAX=IFIX(10.*YMAX)+1
      GO TO 30
   34 IYMAX=21
      GO TO 30
   31 IYMAX=1
   30 CONTINUE
      DO 200 J=1,IYMAX
C         DO LOOP SPANS RANGE OF Y PERMITTED FOR GIVEN X.
      Y=-0.1+0.1*J
C         INCREMENT IJ THE RUNNING INDEX OF POINTS.
      IJ=IJ+1
C         CALCULATION OF ANGLE EPSILON FOR GIVEN X AND Y.
      V=SQRT(X*X+Y*Y)
      IF(V.EQ.0..C.Y.EQ.0.) GO TO 20
   23 COSEP=X/V
      SINEP=Y/V
```

```
C        CALCULATION OF INTENSITY GIVEN BY S. I. M.  FACTOR OF 1,000
C        IS ARBITRARY. NOTE OMISSION OF SEVERAL CONSTANT FACTORS.
      EL=SINEP/2.
      RHOSQ=1.-(COSEP-V)**2
C         RHOSQ .LE. 0 MEANS V IS OUTSIDE LIMITING CARDIOD, TY= C.
      IF(RHOSQ.LE.0.) GO TO 20
      RHO=(SQRT(RHOSQ))/2.
      SINTH=RHO/2.
      DDD=1.-(D23*D23/(RZERO*RZERO))
C         NOW CALL THE NUMERICAL INTEGRATION. THE FUNCTION FINTG WILL BE
C         INTEGRATED BY THE ROUTINE ASMPSN OVER THE RANGE FROM 0 TO 6.28318.
C         THE REL. ERROR BOUND IS .001, AND THE RESULT IS STORED AS ANSWR.
C         IF THE ERROR BOUND IS NOT ACHIEVED, THE PROGRAM WILL JUMP TO 61.
      IF(ASMPSN(FINTG,0.,6.28318,.001,ANSWR).LE.0.) GO TO 61
      TY(IJ)=1.0E3*ANSWR/(V*V)
      GO TO 22
   61 WRITE(9,6100) V,SINEP,EL,RHO
   20 TY(IJ)=0.
   22 CONTINUE
C        GX AND GY ARE THE VALUES PASSED TO THE PLOT ROUTINE.
C        X AND Y GO TO GY AND GX BECAUSE THE PLOTTER PLOTS SIDEWAYS.
      GX(IJ)=Y
      GY(IJ)=X
      DO 300 K=1,4
C        THE UX AND UY FOR VARYING MASSES ARE THE RELATIVE AB PRODUCTS DISTS.
      UX(K,IJ)=UCORR(K)*(X*VCORR(K)-1.0)*(-1.0)
      UY(K,IJ)=UCORR(K)*(Y*VCORR(K))
  300 CONTINUE
C        OUTPUT THE VALUES OBTAINED FOR THIS PARTICULAR LOOP.
      WRITE(9,2001) IJ,TY(IJ),X,Y,UX(1,IJ),UY(1,IJ),UX(2,IJ),UY(2,IJ),UX
     $(3,IJ),UY(3,IJ),UX(4,IJ),UY(4,IJ)
C        SYMMETRIC (Y=-Y) VALUES ARE DONE HERE INSTEAD OF RECALCULATING.
C        NOTE THAT THEY DO NOT APPEAR IN THE PRINTOUT, ONLY THE MAP.
```

```
      IF(Y) 41,41,42
   42 IJ=IJ+1
      TY(IJ)=TY(IJ-1)
      DO 450 KK=1,4
      UX(KK,IJ)=UX(KK,IJ-1)
      UY(KK,IJ)=-UY(KK,IJ-1)
  450 CONTINUE
C        REMEMBER, THE PLOTTER PLOTS SIDEWAYS.
      GX(IJ)=-GX(IJ-1)
      GY(IJ)=GY(IJ-1)
   99 CONTINUE
   41 CONTINUE
  200 CONTINUE
  100  CONTINUE
C        NOW DO THE MAPS...FIRST THE V3 MAP.
      IZ=IJ
      VR=1000. $ VCM=0.
      CALL MAP PLOT
C        NOW THE FOUR U12 MAPS, WITH APPROPRIATE LABELS.
      COMMENT(4)=10H FROM N +
      COMMENT(6)=10HOF U(0).
      DO 500 K=1,4
      COMMENT(3)=COMMX(1,K)
      COMMENT(5)=COMMX(2,K)
      DO 400 L=1,IZ
C        X AND Y GO TO GY AND GX BECALSE THE PLOTTER PLOTS SIDEWAYS.
      GX(L)=UY(K,L)
      GY(L)=UX(K,L)
  400 CONTINUE
      CALL MAP PLOT
  500 CONTINUE
C        THE REMAINDER OF THE PROGRAM PROVIDES THE RADIUS OF THE STABILITY
C        CIRCLES TO BE DRAWN ON THE FOUR U12 MAPS, FOR 5EV LAB ENERGY
```

```
C         INCREMENTS UP TO 240 EV.
      WRITE(9,5001)
      WRITE(9,5002)
C           Q IS THE STABILITY LIMIT IN EV.
      Q=-5.2
      DO 600 L=1,40
      EO=20.+5.*L
      DO 700 K=1,4
      PAREN=        A*C(K)*(1+(A+BC(K))*Q/(BC(K)*EO))/(BC(K)*AB(K))
C         BELOW A CRITICAL ENERGY, THE VARIABLE PAREN IS NEGATIVE. THIS
C         IMPLIES ALL PRODUCT IS BOUND, AND ULIM IS GIVEN AS ZERO.
      IF(PAREN) 51,51,52
   52 ULIM(K)=SQRT(PAREN)
      GO TO 50
   51 ULIM(K)=0.
   50 CONTINUE
  700 CONTINUE
      WRITE(9,6001) EO,ULIM(1),ULIM(2),ULIM(3),ULIM(4)
  600 CONTINUE
 2001 FORMAT(1X,I3,2X,E10.3,2(2X,F8.4),5X,8(2X,F8.4))
 1001 FORMAT(1H1,1X,1HN,4X,9HINTENSITY,2X,17HC COORDS,VO UNITS,25X,41HAB
     $ PRODUCT CM COORDINATES, UNITS OF U(AC))
 1002 FORMAT(1H-,44X,15HN + H2 = NH + H,5X,15HN + HD = NH + D,5X,15HN +
     $HD = ND + H,5X,15HN + D2 = ND + D)
 1003 FORMAT(22X,2HVX,8X,2HVY,5X,4(8X,2HLX,8X,2HLY))
 1004 FORMAT(1H-)
 5001 FORMAT(1H1,6X,51HRADIUS OF INSTABILITY LIMIT(C=-5.2), UNITS OF V(A
     $O))
 5002 FORMAT(6X,6HE(LAB),6X,9HN(H2,H)NH,4X,9HN(HD,D)NH,4X,9HN(HD,H)ND,4X
     $,9HN(D2,D)ND)
 6001 FORMAT(5(5X,F8.4))
 6100 FORMAT(36H INTEGRATION ERROR AT V,SINEP,EL,RHO,4(2XF6.3))
      STOP
```

```
      END
      SUBROUTINE MAP PLOT
      COMMON/NONSYM/CARE(600)
      COMMON/ID/COMMENT(6)
      COMMON/MAP ARAY/GY(700),GX(700),TY(700),IZ,TOTPK
      COMMON/DEFINE/VR,VCM
      COMMON/CCFACT/FACT
      COMMON/CCPOOL/XMIN,XMAX,YMIN,YMAX,CCXMIN,CCXMAX,CCYMIN,CCYMAX
      DIMENSION B(4)
      DIMENSION PEAKX(2),PEAKY(2),GMAX(2)
      DIMENSION ROUND(14),XP(2),YP(2)
      DATA((ROUND(I),I=1,14)=1.,1.2,1.4,1.7,2.,2.5,3.,3.5,4.,4.8,5.5
     *,6.5,7.6,9.)
C         THE SUBROUTINE MAPPLOT IS TAKEN DIRECTLY FROM JOHN WINN'S PROGRAM
C         DATAMAP, WITH THE FEATURES FOR MAKING A SYMMETRIC MAP REMOVED.
      FACT=1.
      TOTPK=1.
      DO 10 I=1,600
   10 CARE(I)=0.0
    1 CCXMIN=100. $ CCXMAX=1100. $ CCYMIN=70. $ CCYMAX=1070.
      DO 800 J=1,IZ $ GX(J)=-GX(J)
  800 GY(J)=-GY(J) $ CALL SEARCH(GX,IZ,PEAKX(1))
      CALL SEARCH(GY,IZ,PEAKY(1)) $ DO 801 J=1,IZ $ GX(J)=-GX(J)
  801 GY(J)=-GY(J) $ CALL SEARCH(GX,IZ,PEAKX(2))
      CALL SEARCH(GY,IZ,PEAKY(2)) $ CALL SEARCH(PEAKY,2,GMAX(1))
      CALL SEARCH(PEAKX,2,GMAX(2)) $ IF(GMAX(1).EQ.0.) GMAX(1)=GMAX(2)
C FOR CENTERLINES
      XRAT=GMAX(2)/GMAX(1)
      IF(XRAT.LT.1.0) XRAT=1.0
      IF(XRAT.GT.2.0) XRAT=2.0
      IF(XRAT.EQ.2.0) GMAX(1)=0.5*GMAX(2)
      PART=20.
      GMAX(2)=-GMAX(1) $ CALL LINEUP(GMAX,2,ROUND,14,PART,YMIN,YMAX)
```

```
      XMIN=XRAT*YMIN $ XMAX=XRAT*YMAX $ CCXMAX=600.+500.*XRAT
      CALL SEARCH(TY,IZ,PK) $ PK=PK*TOTPK $ TOTPK=PK
      PK=TOTPK
      TOTPK=TOTPK*.1
   55 DO 803 J=1,IZ $ GX(J)=GX(J)/YMAX*500.
  803 GY(J)=GY(J)/YMAX*500.
      XLIM=PEAKX(2)/YMAX*500. $ CCLIM=CCXMIN+500.+XLIM
  115 DO 804 J=1,IZ
      ENCODE(10,8,INT) TY(J)
    8 FORMAT(1PE6.0)
      IF(TY(J).EQ.0.) INT=4H 0E+
      CCX=CCXMIN+494.+GX(J)
      CCY=CCYMIN+491.+GY(J)
      CALL CCLTR(CCX,CCY,0,1,INT,2)
      CCX=CCX+9. $ CCY=CCY+7.
      INT=LEFT(INT,18)
      CALL CCLTR(CCX,CCY,1,1,INT,1)
      CCY=CCY+5.
      INT=LEFT(INT,12)
      CALL CCLTR(CCX,CCY,1,1,INT,1)
  804 CONTINUE
      DO 920 MI=1,IZ $ GX(MI)=GX(MI)*YMAX/500.
  920 GY(MI)=GY(MI)*YMAX/500.
  901 XP(1)=YMIN $ XP(2)=YMAX $ YP(1)=YP(2)=0.
      XMIN=YMIN $ XMAX=YMAX $ CCXMAX=1100.
      CALL CCPLOT(XP,YP,2,4HJOIN,3,1) $ CALL CCPLOT(YP,XP,2,4HJOIN,7,1)
      CCXMAX=XRAT*500.+600. $ XMAX=XRAT*YMAX $ XMIN=XRAT*YMIN
      CALL CCGRID(1,6HNOLBLS,1)
      CALL CCLTR(CCLIM +70.,CCYMIN+ 97.,1,2,COMMENT,60)
      GNOM=(VR-VCM)/1000./YMAX*500. $ CCX=509.+CCXMIN+GNOM
      CCY=494.+CCYMIN
      CALL CCLTR(CCX,CCY,1,3,1HX,1)
      CALL CCNEXT
```

```
      RETURN
      END
      SUBROUTINE SEARCH(A,N,P)
      DIMENSION A(N)
C          SEARCH IS A SUBROUTINE OF MAPPLOT.
      P=A(1) $ DO 1 I=2,N
    1 IF(A(I).GT.P) P=A(I)
      RETURN
      END
      FUNCTION FINTG(FI)
      REAL L
      COMMON/INTEG/L,P,D,V
C          FINTG CONTAINS THE FUNCTION INTEGRATED BY ASMPSN.
      BIGA=4.*(L*L+P*P-2.*L*P*COS(FI))/(V*V)
      SINCH=1./SQRT(BIGA+1.)
      CSQCH=BIGA/(BIGA+1.)
      FINTG= SINCH/SQRT(1.-D*CSQCH)
      RETURN
      END
      FUNCTION ASMPSN(F,XA,XB,EPS,AREA)
C         ADAPTIVE  SIMPSONS  RULE
C         NOV. 3, 1966
C          INTEGRATION ROUTINE, FROM LIBRARY SOURCE, SUBSET ASMPSN.
C          SEE COMPCEN LIBRARIAN FOR DOCUMENTATION.
      DIMENSION X(7,15),FX(7,15),AEST(3,15),DX(15),TOL(15),J(15)
      DATA LMAX/15/
      THREE=1.    $  FIRST=0
C         ABOVE CAN BE REPLACED BY THREE=3.  AND FIRST=1.
      TOL=ABS(EPS)
      LSMPS=100
      LSAVE=1
      AI=0
      IF(EPS .LT. 0 ) AI=AREA
```

```
      X(5)=XA    $    X(7)=XB
      FX(5)=F(XA)    $    FX(7)=F(XB)
      EST= FX(5)+FX(7)
      DX=(XB-XA)/18
       DO 5 K=2,18
       X=XA+(K-1)*DX
 5     EST=EST+F(X)*(4-2*MOD(K,2))
      EST=DX/3*EST + AI
      X(6)=(X(5)+X(7))/2
      FX(6)=4*F(X(6))
      DX=(X(7)-X(5))/2
      AEST(3)=DX*(FX(5)+FX(6)+FX(7))/3
 50   ERRSUM=0
      TOTSUM=EST
      L=1
      J=3
C       BEGIN  ADAPTIVE  PROCEDURE
C       INCREASE  LEVEL
 100  L1=L
      L=L+1
      LSAVE=MAXO(LSAVE,L)
      TOL(L)=TOL(L1)/THREE
      J1=J(L1)
      DX(L)=DX(L1)/3
C       PUSH  DOWN  OLD  COORDINATES
 150  KJ=2*J1-2
       DO 110 KK=1,3
       KA=KJ+KK
       K=3*KK-2
       KL1=7*L1
       KL=KL1+K
C     (K,L) = KL
       KLA=KL1-7+KA
```

```
C      (KA,L1)=KLA
        X(KL)=X(KLA)
 110    FX(KL)=FX(KLA)
C        CALCULATE  NEW  COORDINATES
       DXL=DX(L)
       H=DXL/3
       J(L)=1
        DO 120 KA=2,3
         DO 120 K=KA,6,3
         KL=7*L1+K
C      (K,L) = KL
         X(KL)=X(KL-1)+DXL
 120     FX(KL)=F(X(KL))*(4-3*MOD(K,2))
       SUMK=0
        DO 130 K=1,3
        KA=2*K-1
        KB=KA+2
        KL=3*L1+K
C      (K,L) = KL
        AEST(KL)=0
         DO 135 KJ=KA,KB
 135     AEST(KL)=AEST(KL)+FX(KJ,L)
        AEST(KL)=H*AEST(KL)
 130    SUMK=SUMK+AEST(KL)
       DSUMK=SUMK-AEST(J1,L1)
       SUMK=SUMK+DSUMK/80
       ABD=ABS(DSUMK)
       IF(L.LE. 2) GO TO 100
       TOTSUM=TOTSUM+DSUMK
       IF(ABS(SUMK*EPS) .GE. ABD .OR. TOL(L)*TOTSUM .GE. ABD) GO TO 200
       IF(L .LT. LMAX) GO TO 100
C         HIT  BOTTOM  OF  TREE
 200   ERRSUM=ERRSUM+ABD
```

```
  205  AEST(J1,L1)=SUMK
       IF(J1 .GE. 3 ) GO TO 210
       J1=J1+1
       J(L1)=J1
       GO TO 150
  210  IF(L .LE. 2) GO TO 220
       L=L1
       L1=L-1
       J1=J(L1)
       L13=3*L1+1
C      (1,L)=L13
       SUMK=AEST(L13)+AEST(L13+1)+AEST(L13+2)
       GO TO 205
   220 AREA=AEST(3)+AI
       ASMPSN=MINO(LSMPS,LSAVE)
       IF (ABS(EPS*AREA) .GE. ERRSUM/80.) RETURN
       IF(FIRST .NE. 0. ) GO TO 300
       LSMPS=0
       FIRST=1.
       THREE=3.
       GO TO 50
  300  ASMPSN=-LMAX
       RETURN
```

*TECHNICAL INFORMATION DIVISION*
*LAWRENCE BERKELEY LABORATORY*
*UNIVERSITY OF CALIFORNIA*
*BERKELEY, CALIFORNIA 94720*